# EXPERIMENTAL DETERMINATION OF BLADE FORCES IN A CROSS-FLOW TURBINE

by

Lee R. Van Dixhorn

thesis submitted to the Faculty of the

Virginia Polytechnic Institute and State University

in partial fulfillment of the requirements for the degree of

MASTER OF SCIENCE

in

Mechanical Engineering

APPROVED:

| | |
|---|---|
| J. Moore, Co-Chairman | H. L. Moses, Co-Chairman |
| A. G. Szeless | S. B. Thomason |

March, 1984

Blacksburg, Virginia

# EXPERIMENTAL DETERMINATION OF BLADE FORCES IN A CROSS-FLOW TURBINE

by

Lee R. Van Dixhorn

(ABSTRACT)

A cross-flow turbine was tested to determine the magnitude of the fluid forces on the blades. The tangential and radial forces and the torque were measured on a test blade.

Because the runner was made of plexiglas, the flow and the effects of the incidence angle at various speeds were observed.

The pattern of blade loading over a revolution was measured over a range of heads from 1.0 to 2.6 m. The maximum forces were found to occur just before the blade leaves the nozzle exit.

The experimental forces agree reasonably well with the results of a control volume analysis. Two figures are provided, by which the designer may determine the tangential and radial forces for any geometrically similar machine.

ACKNOWLEDGEMENTS

In the process of completing this thesis, I have realized the large role others had in it. My thanks go to the following people.

My wife and best friend, Ann, for her patience and support.

Dr. Hal Moses, who originally conceived the project and derived the equations used in the analysis.

Dr. John Moore, for his enthusiastic interest and the long Friday afternoons.

Dr. A. Szeless and Dr. S. Thomason for serving on my committee.

Johnnie, Jack, Red and all the others in the shop who did an excellent job of building the "waterwheel".

Jim Ruggiero of the Learning Resources Center who "tried again" enough times to get good photographs.

The Mechanical Engineering Department for paying for the fabrication and instrumentation expenses of an unfunded project.

The College of Engineering for the Pratt Supplemental Fellowship.

TABLE OF CONTENTS

LIST OF FIGURES

LIST OF TABLES

## NOMENCLATURE

| | |
|---|---|
| A | Nozzle Throat Area, sL |
| BDC | Runner Position, Bottom Dead Center |
| $C_1$ | Nozzle Coefficient |
| D | Runner Diameter |
| f | Differential Force of the Blade on the Fluid |
| F | Force of the Fluid on the Blade |
| FC | Flow Coefficient, $Q/\omega LD^2$ |
| $F_1$ | Nondimensional Force, $F/\rho\omega^2 LD^3$ |
| g | Acceleration due to Gravity |
| H | Head |
| k | Factor defined as $(X_o-X_i)/(r_o-r_i)$ |
| L | Runner and Nozzle Width |
| m | Mass Flow Rate per Blade Passage |
| N | Rotational Speed, RPM |
| $N_1$ | Nondimensional Speed, $U/\sqrt{2gH}$ |
| p | Pressure |
| P | Power |
| $P_1$ | Nondimensional Power, $P/\rho(2gH)^{1.5}\ LD$ |
| Q | Flow Rate |
| $Q_1$ | Nondimensional Flow Rate, $Q/\sqrt{2gH}\ LD$ |
| r | Runner Radius |
| s | Nozzle Throat Height |
| T | Blade Torque |

Nomenclature (cont.)

| | |
|---|---|
| U | Tangential Runner Velocity |
| V | Absolute Velocity |
| W | Relative Velocity |
| X | Relative Flow Angle, $W_t/V_r$ |

Subscripts

| | |
|---|---|
| c | Centrifugal Effect |
| i | Inside radius |
| o | Outside Radius |
| r | Radial Direction |
| s | Static |
| t | Tangential Direction |
| 1 | Nondimensional |

Greek Letters

| | |
|---|---|
| $\alpha$ | Total Convergence Angle and Absolute Velocity Angle |
| $\beta$ | Relative Velocity Angle |
| $\delta$ | Nozzle Enclosed Angle |
| $\phi$ | Blade Pitch Angle |
| $\rho$ | Water Density |
| $\omega$ | Angular Velocity |
| $\eta$ | Efficiency |

# Chapter I

# INTRODUCTION

## 1.1 INTRODUCTORY COMMENTS

The cross-flow turbine has been descriptively named, because its distinguishing feature is that water passes in, across, and out of the runner. It has gained renewed interest in the past few years due to several key features. First, it has strong potential to be inexpensively produced, and second, it maintains moderately high efficiencies over a broad range of flow rates.

This thesis describes research done on a cross-flow turbine to determine the magnitude of the fluid forces on the blades. The first chapter will deal with hydropower development in a historical context and review the research which has been done on the cross-flow turbine. Following chapters will include the design and testing of the experimental model and the development of an analytical expression for the blade forces. The final chapters will describe the results of the testing and recommend future work.

## 1.2 HISTORICAL PERSPECTIVE

Hydro-power has historically played a major role in America's development. Early dams with waterwheels provided reliable power and by the late nineteenth century were followed by small generating plants, first developed for lighting systems. The Vulcan Street Plant in Appleton, Wisconsin was recently commemorated as "the first hydroelectric central station in the world when it began operation in September 1882" [1]. These small plants were followed by larger ones and by 1930 hydropower supplied nearly 40% of America's electric energy [2]. But the most promising sites were soon taken and development of new sites became more costly and they were located far from the load centers. To meet increased power consumption, other sources of power were developed and by the 1970's hydropower's share of the total electric generating capability was less than 15% [2].

The oil embargo of 1973, however, caused much concern over America's power supply. Conservation was urged and new sources were investigated. Today, hydropower is still being examined, and since most of the large sites have been taken, a large percentage of possible development lies in the small hydropower range (less than 15 MW of total power capacity). Figure 1 shows that this in not the case for the rest of the world--countries outside of North America and Europe have far more undeveloped sites.

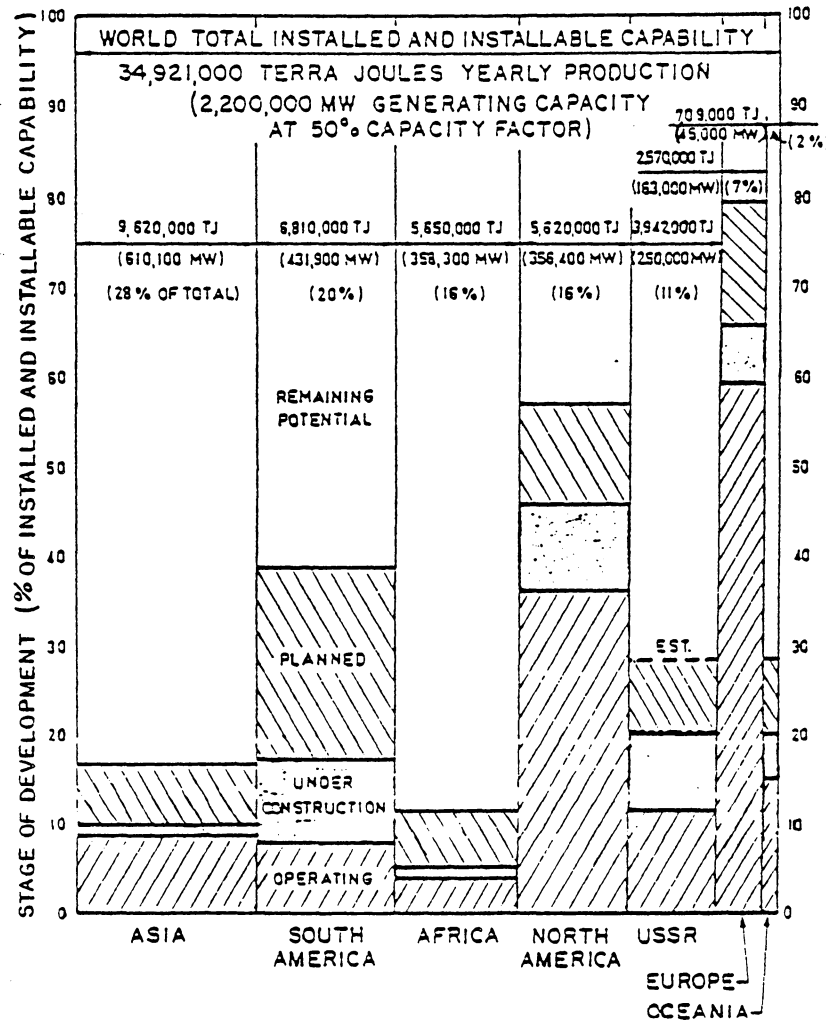


Figure 1 : World Hydropower Resources [3]

But for America, many remaining sites are small. Figures 2 and 3 show the geographic location and relative sizes of hydropower resources for all sites and for small-scale sites (less than 15 MW). These figures especially show the large potential at incremental sites--where there is already an existing dam.

But even the most optimistic hydropower developers realize serious difficulties need to be resolved in developing small sites. If no dam is in existence, the cost for civil features can be prohibitive. For the incremental sites, where there is already an existing dam for flood control, recreation or previous use for power generation, these costs may be much lower. Some of these are being developed by utilities and others by private entreprenuers [5]. The engineering design and legal costs can also be a major portion. Hydropower is often site-specific and if much engineering design is needed, this will add substantially to the cost. The legal/institutional aspects can be time consuming and a barrier to development. Finally, the equipment costs are a substantial portion of the overall cost. From Fig. 4, it can be seen that 18-39% of the total cost is equipment cost. Since this is such a large percentage, development of a low-cost turbine would increase the feasibility of small hydropower projects.

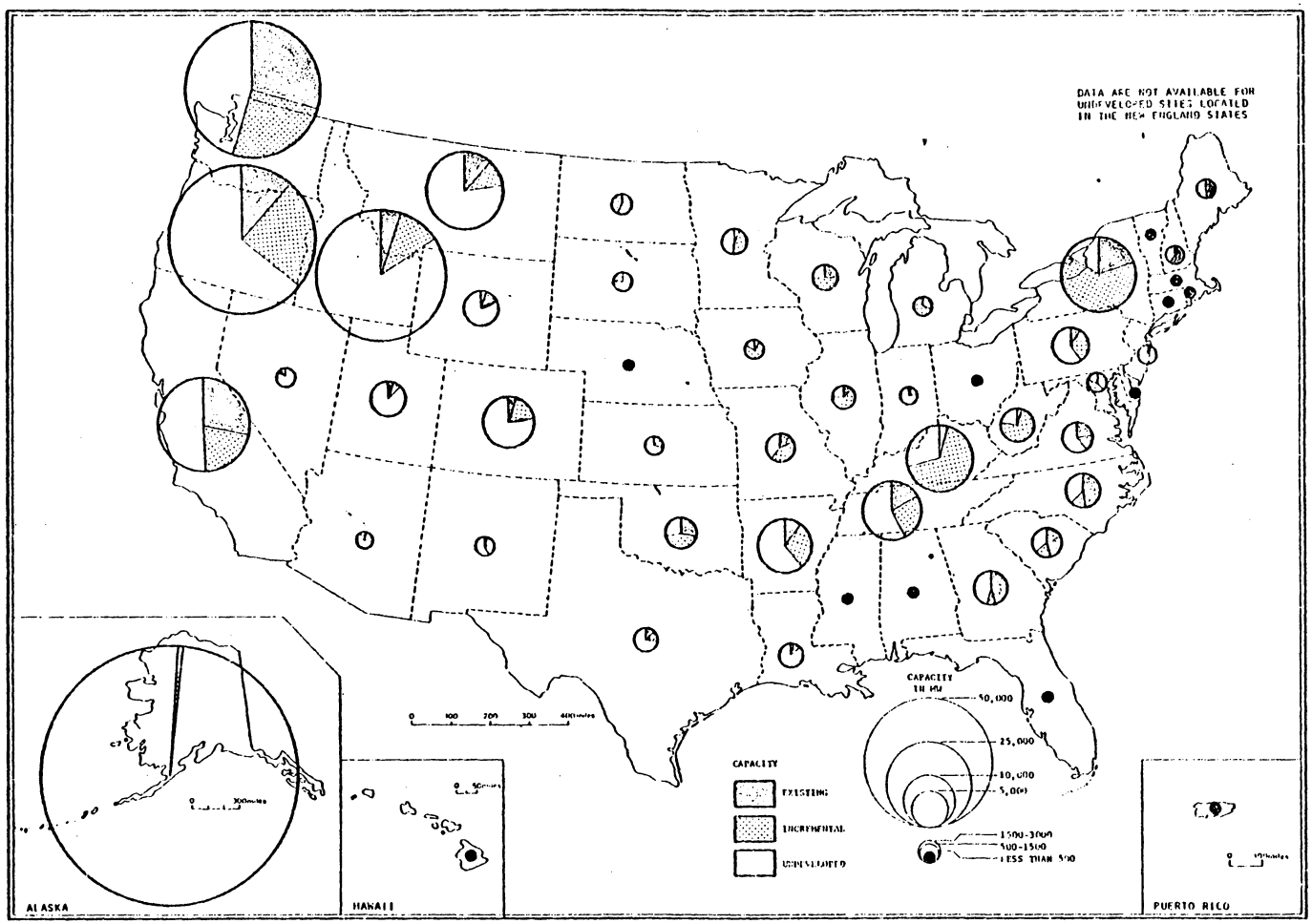


Figure 2: Hydro Resources in the United States--All Sites[4]

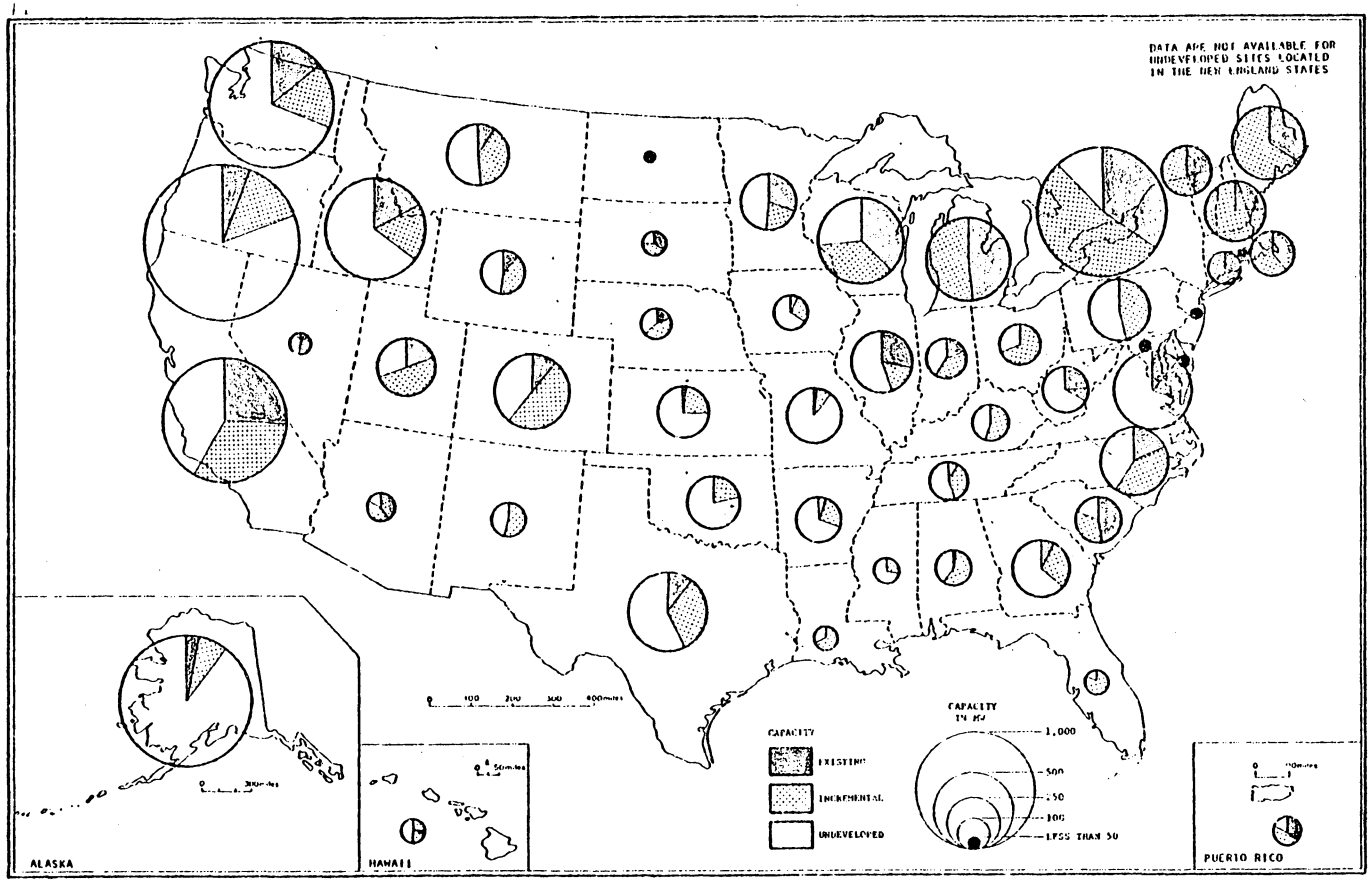


Figure 3: Hydro Resources in the United States--Small Sites[4]

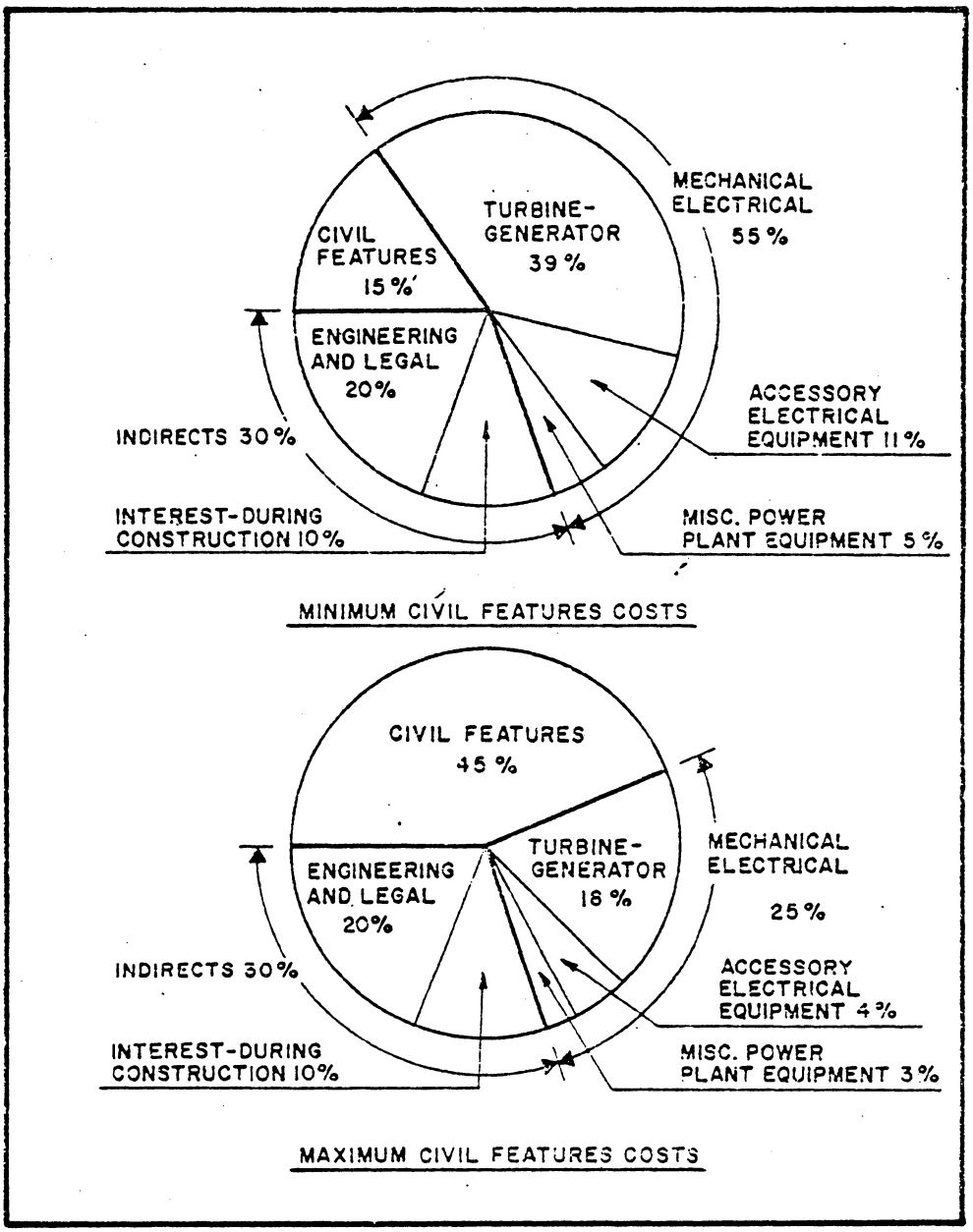


Figure 4: Cost Elements in Small Hydro Sites[6]

Turbines for small hydropower include the propellor and Francis turbines which are the most commonly used at larger sites. Several manufacturers produce smaller standardized units which help to cut costs. Other turbine designs which are being used include bulb turbines, Straflo turbines, the Schneider Engine, and the cross-flow turbine. For more complete information on this equipment see references [7,8]. Reference [9] includes economic factors in evaluating small-hydro sites. For this paper, we will focus on the cross-flow turbine.

## 1.3 LITERATURE REVIEW

The cross-flow turbine was invented at the turn of the century by an Australian engineer, A. G. Michell. It was further developed by the Hungarian professor, Donat Banki, who patented it in Germany and published a series of articles on it between 1917 and 1919 [10]. It became widely used in Europe due to its development by the Ossberger Company, which is the only major manufacturer of the cross-flow turbine. Early work in America is described by Mockmore and Merryfield [11], who translated Banki's work and published the results of testing done on a turbine built to his specifications. The analysis includes a very detailed description of the runner geometry but is based on a single free-jet

striking the blades and never completely filling the passages. This results in a good maximum efficiency for a small model (70%) but a fairly low power output/size ratio.

Haimerl's paper in 1960 [10] shows new insight in the nozzle design. He notes that using a nozzle design which follows the runner periphery gives better results but is no longer a true impulse turbine because there is a positive static pressure at the nozzle outlet. He also describes several Ossberger installations, showing the use of a draft tube to increase the net available head and the use of the current Ossberger inlet throttling vane.

A recent study by Johnson, et al. [12], describes the testing of a unit with an inlet throttling vane. Two enclosed angles (the arc of the nozzle covering the runner) of 120 and 106 degrees total were tested. A primary goal of the testing was to gain experience with new materials. The runner blades were made of polyvinylchloride (PVC) pipe, and the inlet vane was wood coated with type I PVC. Another recent study by Nakase, et al. [13] is a very thorough and detailed analysis of the nozzle. Testing was done on units with an enclosed angle of 30, 60, 90, and 120 degrees. Also, several nozzle rear wall shapes were tested and the flow angle was measured at the nozzle exit. From the testing, the optimum enclosed angle (90 degrees) and rear wall shape were determined.

Other writings on the cross-flow turbine include a section in a text by Balje [14] and a description of the construction and performance of the Ossberger turbine by Stapenhorst, the North American distributor for Ossberger [15].

References [16,17, and 18] show the possibilities of low-cost production. Hamm [16] and Breslin [17] describe how to build a cross-flow turbine with only minimal tools. This is especially aimed at less-developed countries, where a turbine which is sturdy, easy to build and maintain is needed. Durali [18] designed a small turbine for farm use. He shows an analysis and drawings for a cross-flow and other small turbines. The applicability of the cross-flow to less-developed nations is clearly shown by literature from a company in Nepal which manufacturers a line of turbines which develop from 2 to 75 kW [19].

## 1.4 OBJECTIVES

The research done to-date has been generally directed at improving efficiency and developing low-cost plans. There has been nearly no work done in the area of the mechanical aspects, to determine how large the forces are within the turbine and thus, the type and strength of the material needed. Reference [12] is the only one to mention this

aspect. The authors give a stress formula for the blades which is seriously limited because it omits the number of blades.

The major objective of this study was to determine the magnitude of the fluid forces on the blades in the turbine. Thus, the turbine dimensions were chosen to be consistent with other published designs, not varied in an attempt to maximize efficiency. It was decided to measure blade forces rather than stresses because stresses are dependent on how the blades are fastened to the runner sides. However, if the forces are known, the stresses can be determined for each fastening technique.

An added benefit from measuring the blade forces is that the flow characteristics within the turbine can be inferred. The pattern of flow within each passage as well as the relative magnitude of forces in each stage can be determined.

The cross-flow turbine generally maintains good efficiencies at widely varying flow rates by directing the flow through only a portion of the runner. This feature was not investigated because the blade forces are the greatest at the highest flow rate and only the maximum blade forces are needed for design purposes.

# Chapter II

# EXPERIMENTAL MODEL

## 2.1 TURBINE DESIGN

As previously stated, the turbine was designed not to maximize efficiency, but to have consistent geometry and blade shapes with other published designs. The turbine was designed to operate within the flow rates and head capabilities of the available pump. The nozzle and rotor sides and the casing were made of plexiglas so the flow could be observed. The overall configuration of the nozzle and runner and the nomenclature used is shown in Fig. 5.

## 2.2 RUNNER AND NOZZLE GEOMETRY

The runner diameter and width were calculated assuming free-jet conditions from the nozzle throat. It was known that this was not entirely true because the nozzle exit is at some positive static pressure. This results in flow rates which are lower than calculated, but the design conditions were somewhat arbitrary. The equation for the volume flow rate of a free jet can be written as follows:

$$Q=AV=sLC_1\sqrt{2gH} \qquad (2.1)$$

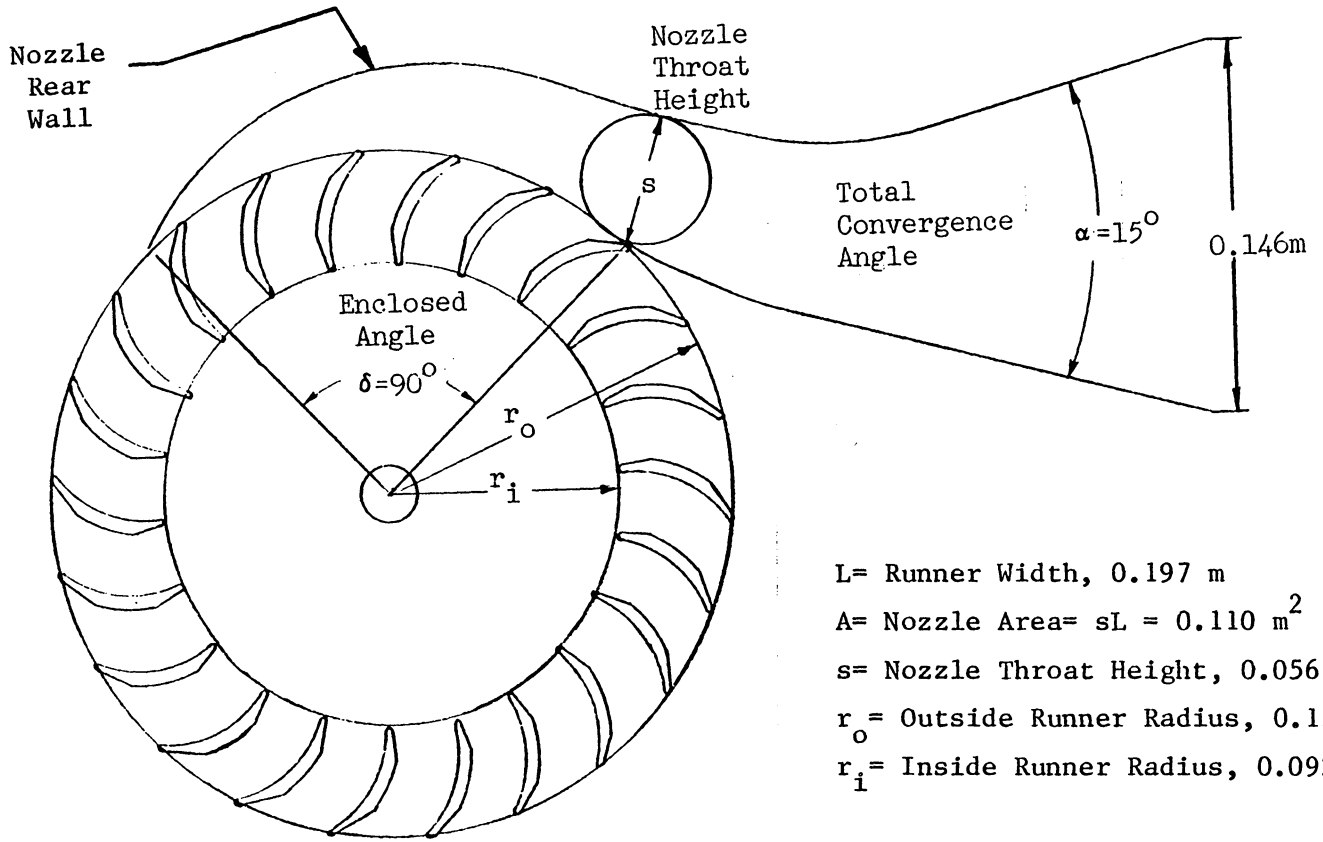


Figure 5: Runner and Nozzle Dimensions

The authors of reference 13 tested several nozzle geometries and determined that the most efficient enclosed angle, $\delta$, is 90 degrees. They determined that the rear wall shape was not extremely critical but high efficiencies were obtained with a constantly decreasing area nozzle (which is nearly a logarithmic-spiral). For a 90 degree enclosed angle, and for a constantly decreasing area nozzle with a total convergence angle, $\alpha$, of 15 degrees, the throat width, s, can be expressed as:

$$s = 0.202D \tag{2.2}$$

Combining equations 2.1 and 2.2, we can write

$$LD = Q/(0.202C_1\sqrt{2gH}) \tag{2.3}$$

Assuming a nozzle coefficient, $C_1=1$, and choosing a design flow rate and head of $Q=0.085$ $m^3/sec$ and $H=3$ m, the product of LD is equal to 0.055 $m^2$. Any product of LD which gives 0.055 $m^2$ would be acceptable, but for simplicity of construction and visibility a large diameter was preferrable. A large diameter gives lower optimum speeds, however, and a very low speed was undesirable.

The optimum speed in RPM can be expressed as a function of head and runner diameter in the form:

$$N_{optimum} = C_2\sqrt{gH/D^2}$$

The value of $C_2$ was determined from theoretical calculations in references 10 and 11 and experimentally in reference 13, and is in the range of 12.7 to 14.5. This can also be written in terms of a nondimensional speed, $N_1 = U/\sqrt{2gH}$ and it ranges from 0.47 to 0.54. Thus, for an optimum speed of 280 RPM, and our design conditions, this gives the dimensions L and D to be:

D=0.277 m

L=0.197 m

It should be noted that this method of sizing the turbine would not be accurate enough for an actual installation, because the flow rate will be lower than estimated. The better technique is to use experimental data for a machine with a similar geometry and scale it appropriately.

Since the blade shape is a circular arc, it was convenient to use pipe sections. Standard 3.5 in. nominal diameter, schedule 40 aluminum pipe was used. A flat was machined on both the leading and trailing edges to minimize losses on each pass through the turbine. The inside to outside radius was chosen to be 0.66. The actual geometry was determined with a layout drawing of the runner, by reference to calculations by Mockmore and Merryfield [11] and by comparison to the geometries shown by Nakase, et al. [13]. A detailed drawing of the blade is shown in Fig. 6.

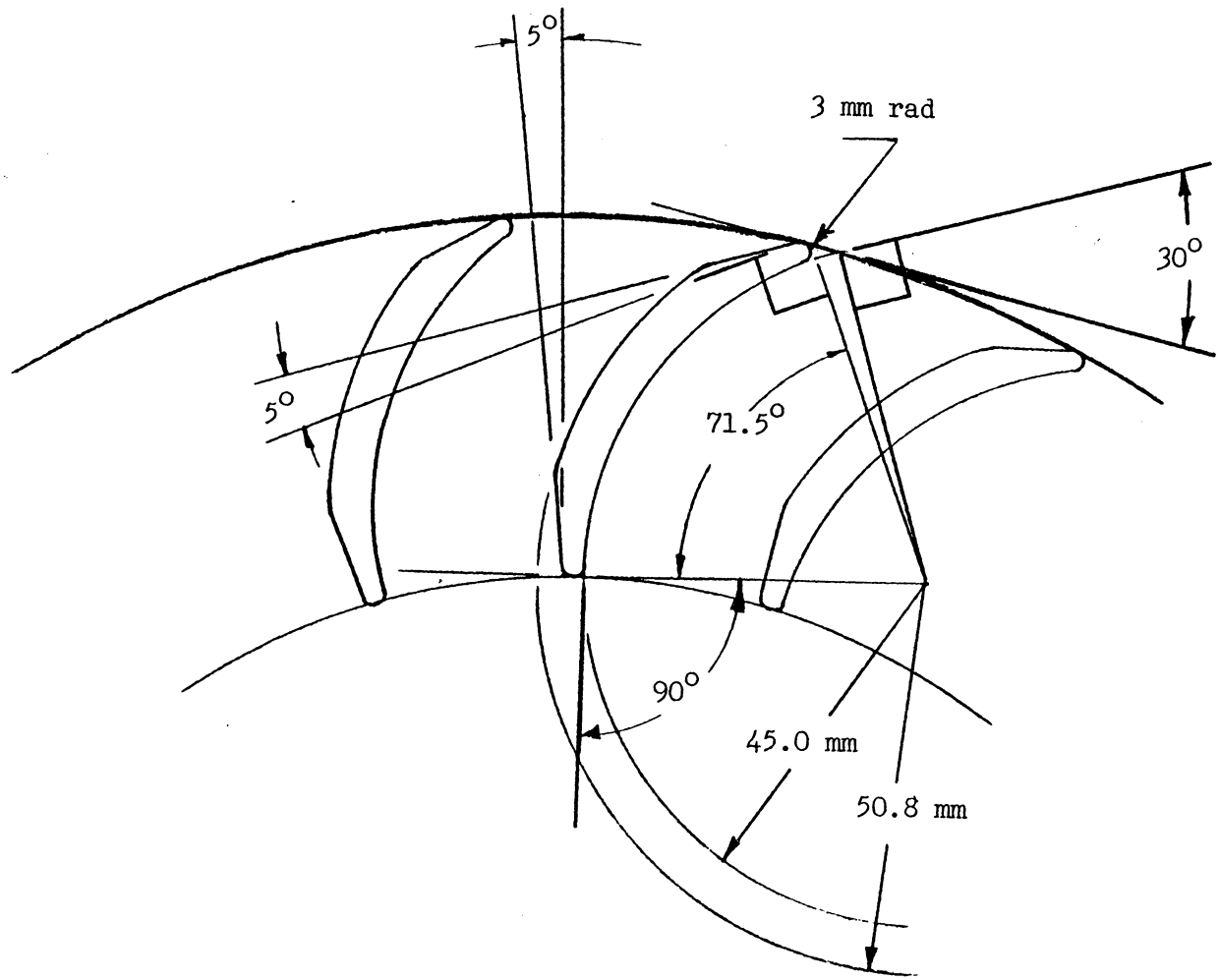


Figure 6: Blade Detail

## 2.3 CONSTRUCTION FEATURES

The runner and nozzle sides were made from plexiglas so the flow could be observed. The nozzle front and rear wall were made of sheet aluminum. The 22 blades were fastened by screws to the runner sides. The runner sides were attached to 2 hubs which joined them to the steel shaft. Two standard pillow block bearings were used to support the runner. The wheel for the Prony brake was attached to one side of the turbine shaft and a small metal box was attached around the slip-ring assembly on the other end. This arrangement, as well as the instrumentation used is shown in Fig. 7.

The frame was made from angle iron. It was placed on the tank floor and attached to the tank sides. The plexiglas casing consisted of 5 sections and was attached to the inside of the frame.

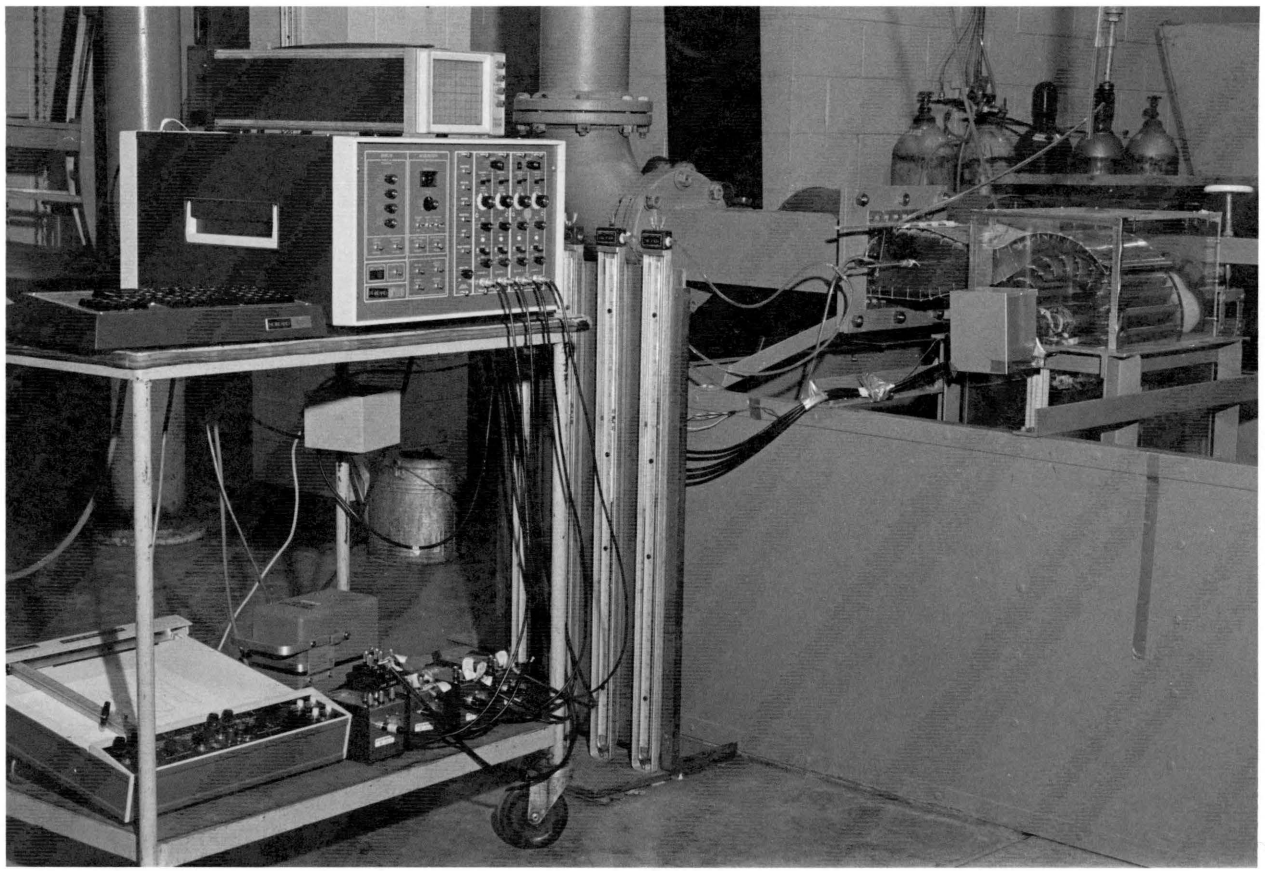

Figure 7: Instrumentation and Overall Layout

# Chapter III

# INSTRUMENTATION

## 3.1 INTRODUCTION

The primary goal of the testing was to determine the magnitude of the fluid forces on the blades. However, the flow rate, head, rotational speed and power output were also needed. This chapter describes the instrumentation used for these measurements. Also, an uncertainty analysis is presented with bounds placed on the uncertainties.

## 3.2 FLOW RATE

The flow rate was measured with a Venturi meter that had been installed for previous experimental work by Siegel [21]. The inlet diameter is 0.203 m (8 in.) and the throat diameter is 0.102 m (4 in.). The discharge coefficient for this type of Venturi is 0.983 [21], which is valid from 0.04 to 0.30 $m^3/sec$. The pressure differential was read on a 36 in. water-over-mercury manometer. For this arrangement, the flow rate can be expressed as:

$$Q\ (m^3/_{sec}) = 0.0214 \sqrt{(\text{Reading in inches of Mercury})}$$

The manometer has a scale graduated in 0.1 in. increments and could be read to the nearest 0.05 in. (0.12 kPa). With

this readability, the uncertainty varies from 0.3% at high flow rates to 0.7% at low rates. Figure 8 shows the arrangement of the Venturi meter in the supply piping. A drilled plate was installed in the piping to keep the Venturi throat pressure above atmospheric and to insure uniform flow entering the turbine.

### 3.3 HEAD

Total head is referenced to the height of the turbine shaft. Initially, the head was measured with a total-pressure probe which could be used to traverse the rectangular inlet area. It was found that the velocity head accounted for 12-14% of the total head.

When the probe was at the center of the rectangular inlet, the reading for total head was 3-4% higher than the average total head. Also, there was much debris in the water and even though the probe was fairly large, it would often become partially obstructed. For these two reasons, it was decided to calculate total head by measuring the static head and adding to it the average velocity head.

The static head was measured in two different ways. At the lower heads (1.0-1.5 m) a static tube of water was used and the head could be read directly from the column. At the higher heads, it was necessary to use a mercury manometer

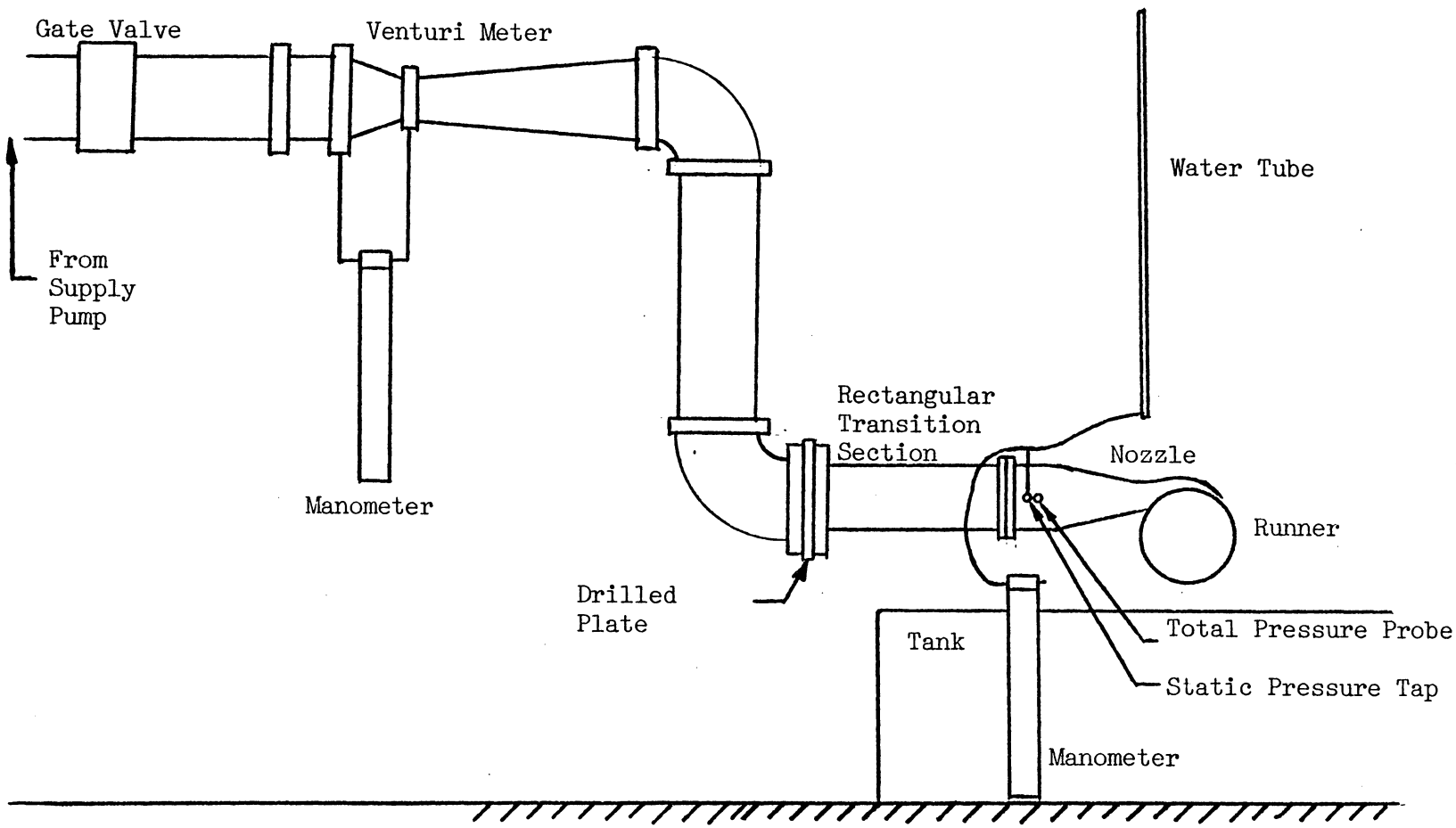


Figure 8: Supply Piping and Instrumentation

with one column of water and the other exposed to the atmosphere. The static head could be calculated by the relation:

$$H_s=0.0254(13.05(\text{Reading in inches of Mercury})-13.35)$$

where the height from the mercury zero level to the shaft is 13.35 in.

The water static tube could be read to the nearest 0.005 m. The mercury manometer could be read to the nearest 0.005 in. of mercury, and was a greater source of error. Errors for the static head were less than 0.7%. Added to the uncertainty of the velocity head, this gives an uncertainty of 0.9% for the total head.

## 3.4 BLADE FORCES

To measure the blade forces, a special test blade was used. This blade has the same configuration as the other blades but is 4.8 mm shorter. It is not fastened to the sides of the runner as the other blades are, but is specially mounted by means of a shaft attached to each side at the center of the blade arc. One side of the blade is mounted in a self-aligning bearing, which allows rotation and enough freedom so the shaft can move freely in both the tangential and radial directions. The other side is fastened to 3 strain links. Figure 9 shows the mounting of the test blade in the

3 links and the bearing. Figure 10 is a photograph of the test blade and the links.

Link A is a slip fit on the blade shaft and resists motion in the tangential direction only. It allows both motion in the radial direction and twisting of the blade. Links B and C are in the radial direction and allow tangential motion but prevent radial motion and twisting of the blade. Strain gages were attached to the three links and their outputs were used to determine the forces. The output from link A gives the tangential force. The radial force is the sum of the outputs from links B and C while the blade torque is the difference of the outputs from links B and C multiplied by the distance separating links B and C.

A complete strain-gage bridge, composed of two compressive and two tensile gages was attached to each link. This arrangement should theoretically eliminate temperature variation and bending effects [20]. The gages were sealed in a high-density wax to eliminate moisture problems. The strain gages were manufactured by Micro-Measurements and are general-purpose constantan 350 ohm resistance gages. They are combined in a transverse and longitudinal configuration for compactness in mounting. The gage configuration and wiring schematic is shown in Fig. 11.

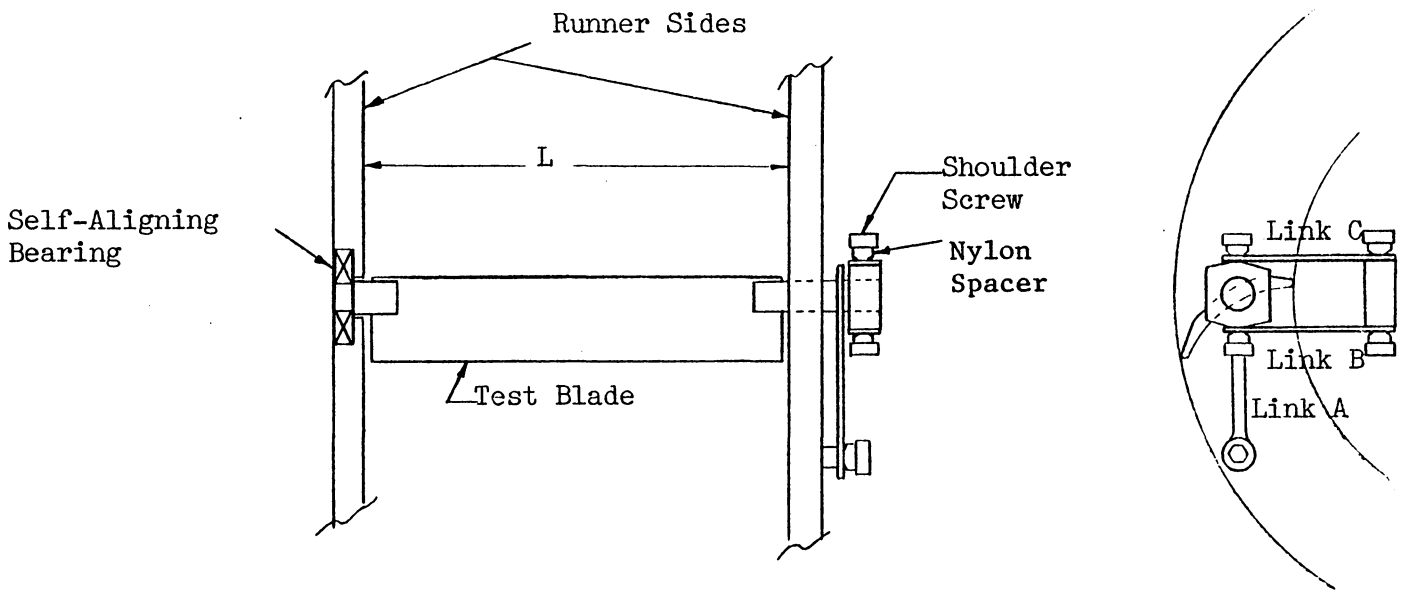


Figure 9: Test Blade Mounting

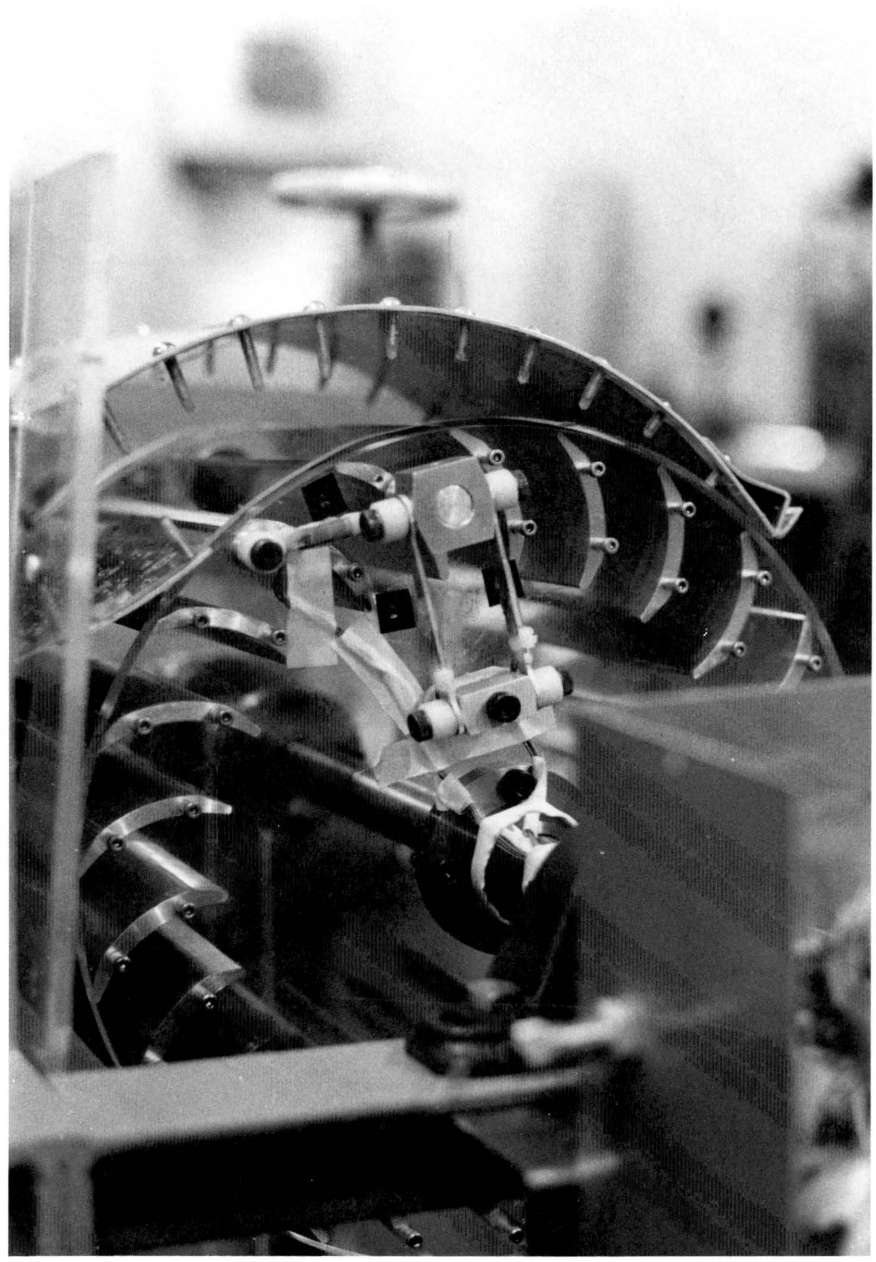

Figure 10: Photograph of Test Blade

Tension Gage (T)

Compression Gage (C)

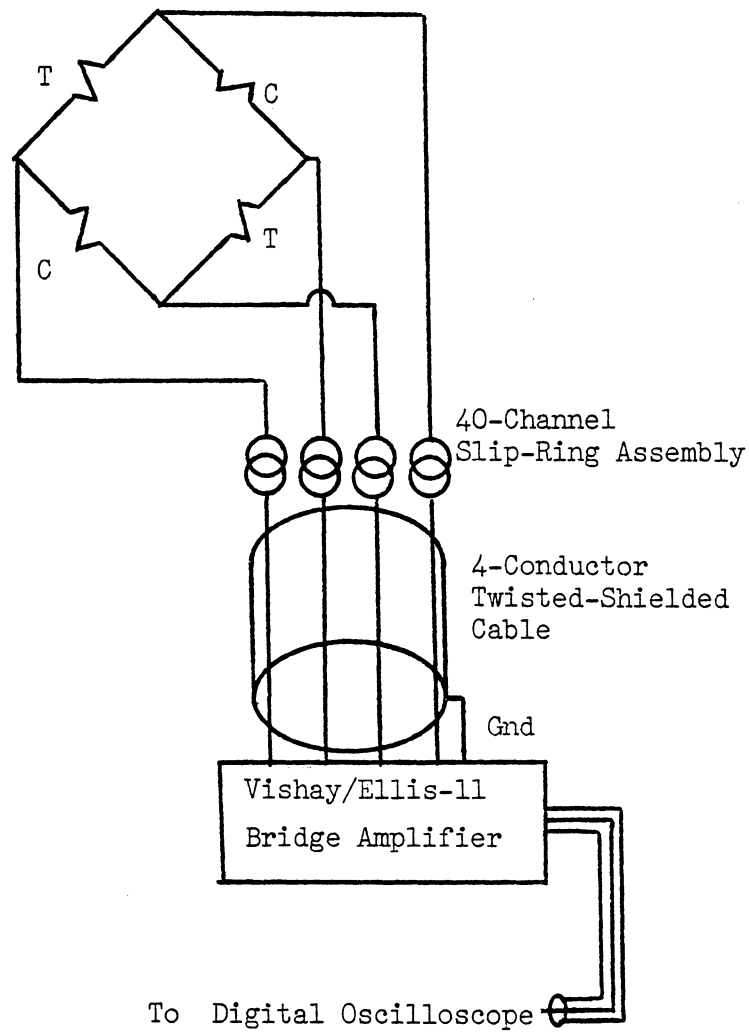


Figure 11: Strain Gage Wiring

The sizing of the links was a balance between a desire for large output signals and the need for sturdy links which would not fail under large variations in load. The actual loads to be expected, or even the direction of the radial force were not known. If the force was inward, buckling would be a problem. Weighing these factors, a cross-sectional area of 16.0 $mm^2$ was chosen.

The four wires from each bridge were routed through the support bearing by a slot in the turbine shaft to a slip-ring assembly. The slip-ring assembly is a 40-channel unit manufactured by Poly-Scientific. Only 12 channels were required, but others were wired in parallel in an attempt to eliminate as much slip-ring noise as possible. The wiring from the slip-ring assembly was connected to four Vishay/Ellis-11 bridge amplifiers, which are shown on the bottom of the cart in Fig. 7. One amplifier was needed for each link and one amplifier for the brake force. The output from the bridge amplifiers was input to the digital oscilloscope, shown on the top of the cart in Fig. 7. This approach worked well. An alternative method is shown by Light [22], who amplifies the signal on the rotor by using operational amplifiers.

The system was calibrated for two positions of the runner by hanging weights from the test blade. The first posi-

tion was when links B and C (radial links) were affected. Link A, in the tangential direction, was normal to the applied force. The second position was 90 degrees from the first position, when link A was calibrated and links B and C were normal to the applied force. See Appendix A for calibration data.

The uncertainty of the blade forces was calculated by summing the uncertainties due to nonlinearity in the output, drift from the setpoint, temperature effects, and interaction between the links. The linearity was calculated by using twice the standard deviation of the calibration curve. The drift was estimated by comparing setpoints before and after taking data. The temperature difference between water and air was originally a source of setpoint shift, but this was essentially eliminated by running the turbine for 20 minutes and then setting the bridge balance. The link interaction came about because a force in the tangential direction had a slight effect on the radial measurements. This value was determined by noting the apparent tangential force when calibrating for radial force and vice-versa. The bounds on the uncertainty are discussed in the uncertainty section.

## 3.5 BRAKE FORCE

The turbine was loaded by a Prony brake with a lever arm of 0.803 m. The brake force was measured using a cantilever beam arrangement with one compressive and one tensile gage which was first used by Siegel [21]. This was used with a Vishay/Ellis-11 bridge amplifier with a model 11-AG bridge-completion module. This was calibrated in place. The brake force is estimated to have an uncertainty of 0.19 N.

## 3.6 SPEED

The rotational speed was originally to have been measured by a "Di-Mag" magnetic pickup used with a 6-screw arrangement and an electronic counter. The "Di-Mag" gave a very sharp, clean pulse, but the electronic counters malfuntioned in the electrically noisy environment. It was decided to obtain the rotational speed by measuring the period of rotation and calculating the RPM. With the high resolution available on the digital oscilloscope, the speed could be measured within 1 RPM.

## 3.7 DIGITAL OSCILLOSCOPE

The digital oscilloscope was the central instrument item in the data acquisition. It was used to determine the rotational speed, the brake force and the blade forces.

The digital oscilloscope used is the Norland Instruments Model 3001 Waveform Analysis System. It is based on the Intel 8085 microprocessor and has the capability of a computer for data handling and analysis, but is already programmed and interfaced for data acquisition. It has a total memory of 4096 12-bit words which were configured into four storage locations for the brake force and the output from the three strain links on the rotor. Also available were up to 24 utility registers, of which several were used for calculation purposes. It has four amplifiers built in, which could be used in a range from +100 V down to +.1 V, which was the range used for the 3 strain links. The display is an oscilloscope face on which the storage contents are displayed. The display has a feature which allows the user to move two pointers by which the exact X and Y (time and force) could be read. This was especially useful in determining the period accurately. The system was connected to a Hewlett-Packard Model 7004B X-Y recorder, which was used to make a paper copy of the data stored in memory. The input was triggered by a pulse from the "Di-Mag" pickup mentioned

earlier, and was set to trigger when the blade shaft was at a position of 45 degrees before the nozzle.

## 3.8 EXPERIMENTAL PROCEDURE

Before any data were recorded, the turbine was run for approximately twenty minutes to ensure that the strain links had come to an equilibrium temperature. Then the water was shut off, the runner was set so the weight of the blade was on only the tangential link, and reference voltages for the strain links and the brake force were taken. This was important for minimizing the offset from zero and for providing a means for determining how much the bridge balance drifted over the testing period.

Then the water was restarted and the manometers for the static pressure and the Venturi were bled to eliminate air bubbles. The brake was set to the desired load, and data were recorded at that condition. The static head, Venturi manometer reading, and the data stored on the digital oscilloscope were recorded as closely together as possible.

The data acquisition on the digital oscilloscope was started by simply pressing the trigger switch. When triggered, the system would acquire 1024 bits of data for each of the four channels. Two sample rates of 1 and 0.5 ms between data points were used. Thus at a typical speed of 180

RPM, using the 1 ms sample rate, this meant 333 sample points per revolution.

Once head and flow rate data had been recorded, the information on the digital oscilloscope was reduced by using a programmed routine. The program performed several main tasks. The first was simply to average the rotor data using a feature called the n-point average. In this case, each data point was averaged with the 10 points immediately surrounding it. This eliminated slip-ring noise and smoothed the curve.

Then, the brake force was integrated and divided by the time, so an integrated average could be attained. This was especially needed at very slow speeds because the brake force was large and somewhat unsteady.

The next step was optional and not always used. The force in the tangential direction was integrated over one revolution. This was used to compare the tangential force output with the average tangential output (as determined from the brake) and determine if the blade had typical forces on it. Also, the power output was calculated.

Finally, the blade forces were determined. For each link, the voltage output was converted to force by multiplying by the conversion factor determined from the calibration curve and the relative lever arm of the calibration weights

to the center of the blade. Links A, B and C had separate conversion factors as shown in Appendix A.

The tangential force is simply the converted output from link A. The radial force is the sum of forces from links B and C. The blade torque is the difference of the forces in links B and C multiplied by the distance between the two links. Once the forces and blade torque were calculated, they were recorded on the X-Y plotter with the appropriate scales.

After several data points were recorded, the water was turned off and the runner set to the calibrate position so reference voltages could again be recorded.

## 3.9 UNCERTAINTIES

The bounds for experimental uncertainties are shown in Table 1. For the primary measurements, flow rate, head and forces, the method used in calculating uncertainties has already been described. For the calculated values, the method of Kline and McClintock [23] was used.

TABLE 1

Experimental Uncertainties

| Measured Variables | | Uncertainty |
|---|---|---|
| p | Pressure Differential in Venturi | 0.12 kPa |
| $H_s$ | Static Head | 0.7% |
| N | Rotational Speed | 1 RPM |
| $F_D$ | Brake Force | 0.19 N |
| $F_A$ | Force on the Tangential Link | 1.60 N |
| $F_B$ | Force on Radial Link B | 1.67 N |
| $F_C$ | Force on Radial Link C | 1.50 N |
| **Calculated Variables** | | |
| Q | Flow Rate | 0.7% |
| P | Power | 0.9% |
| H | Total Head | 0.9% |
| e | Efficiency | 0.9% |
| $N_1$ | Nondimensional Speed | 0.7% |
| $P_1$ | Nondimensional Power | 0.9% |
| $Q_1$ | Nondimensional Flow Rate | 0.7% |
| $F_t$ | Tangential Force on Blade | 1.60 N |
| $F_r$ | Radial Force on Blade | 2.24 N |
| T | Torque on Blade | 0.06 Nm |

# Chapter IV

# ANALYSIS

## 4.1 ASSUMPTIONS

The primary reason for calculating the blade forces is to determine the maximum loading on the blades for design purposes. References 10 and 11 show that the first stage of the turbine gives the major part of the power output. It seems likely that the largest forces will occur when the blade is within the nozzle exit. The analysis calculates the tangential and radial components of the force assuming full flow in the blade passage, axisymmetric, inviscid and two-dimensional flow. The control volume and nomenclature used is shown in Fig. 12.

## 4.2 TANGENTIAL FORCES

Starting with the tangential momentum equation in cylindrical coordinates [24], and omitting the terms described above, we can write:

$$f_t = \rho \left[ V_r \frac{dV_t}{dr} + \frac{V_r V_t}{r} \right] \qquad (4.1)$$

where $f_t$ is the differential force of the blade on the fluid in the control volume and positive $f_t$ is in the direction of rotation.

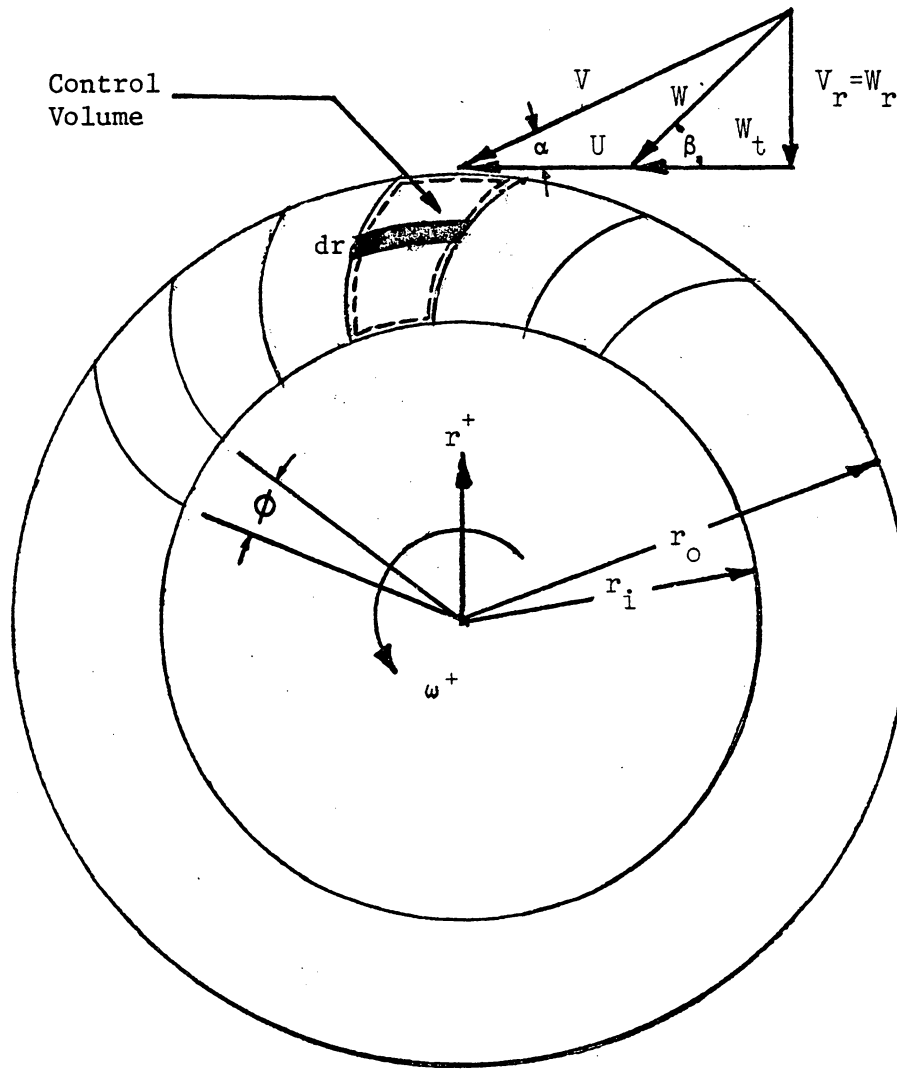


Figure 12: Control Volume

Defining $F_t$ to be the total tangential force of the fluid on the blade, we have:

$$F_t = \int_o^i \phi r L f_t dr \tag{4.2}$$

With this convention, $F_t$ will be positive in the positive direction of rotation. Now substituting for $f_t$, we can write Eq. 4.2 as:

$$F_t = \int_o^i \rho \phi r L \left( V_r \frac{dV_t}{dr} + \frac{V_r V_t}{r} \right) dr \tag{4.3}$$

But the mass flow rate per passage can be written:

$$m = \rho \phi r L V_r \tag{4.4}$$

Note that the mass flow rate, m, will be negative for inward flow.

Simplifying, we write:

$$F_t = m \int_o^i \left( \frac{dV_t}{dr} + \frac{V_t}{r} \right) dr = m \int_o^i \left( dV_t + \frac{V_t}{r} dr \right) \tag{4.5}$$

But $V_t = U + W_t = r\omega + W_t$

and $dV_t = \omega\, dr + dW_t$ (for constant rotational speed)

Thus, $$F_t = m \int_o^i \left( ( \omega\, dr + dW_t ) + ( \omega + \frac{W_t}{r} ) \right) dr$$

$$F_t = m \int_o^i \left( 2\, \omega dr + dW_t + \frac{W_t}{r} dr \right)$$

$$\text{or} \qquad F_t = m\int_o^i \left(2\,\omega\,dr + \frac{1}{r}\,d(rW_t)\right) \tag{4.6}$$

$$\text{Letting} \quad (rW_t) = \frac{V_r rW_t}{V_r} = \frac{W_t\,\rho\phi\,LrV_r}{V_r\,\rho\phi\,L} = \frac{mW_t}{\rho\phi\,LV_r}$$

$$d(rW_t) = \frac{m}{\rho\phi\,L}\,d\left(\frac{W_t}{V_r}\right)$$

$$\text{Defining X to be,} \quad X = \frac{W_t}{V_r} \text{, we can write:}$$

$$d(rW_t) = \frac{m}{\rho\phi\,L}\,dX \tag{4.7}$$

Combining Eqs. 4.6 and 4.7, we have,

$$F_t = m\int_o^i \left(2\,\omega\,dr + \frac{m}{\rho\phi\,L}\,\frac{dX}{r}\right)$$

$$F_t = m\left[2\,\omega(r_i - r_o) + \frac{m}{\rho\phi\,L}\int_o^i \frac{dX}{r}\right] \tag{4.8}$$

Letting X vary linearly from the inlet to the outlet of the blade passage (an assumed variation for the purpose of simplifying the analysis), we can write:

$$X = X_o - \frac{X_o - X_i}{r_o - r_i}(r_o - r)$$

$$X = X_o - k(r_o - r) \qquad \text{where } k = \frac{X_o - X_i}{r_o - r_i}$$

$$dX = k\,dr \tag{4.9}$$

Substituting Eq. 4.9 into the integral in Eg. 4.8, we have:

$$\int_o^i \frac{dX}{r} = \int_o^i k\frac{dr}{r} = k\,\ln\frac{r_i}{r_o}$$

Thus, we can write:

$$F_t = m\left[2\omega(r_i - r_o) + \frac{m}{\rho\varnothing L} k \ln \frac{r_i}{r_o}\right] \tag{4.10}$$

$$F_t = -m\left[2\omega(r_o - r_i) + \frac{m}{\rho\varnothing L} k \ln \frac{r_o}{r_i}\right] \tag{4.11}$$

With the sign convention used, m will be negative and $F_t$ will be positive (the force of the fluid on the blade is in the same direction as the rotation).

## 4.3 RADIAL FORCES

Starting with the radial momentum equation in cylindrical coordinates [24] and making the assumptions initially described, we can write:

$$f_r = \rho\left[V_r \frac{dV_r}{dr} - \frac{1}{r} V_t^2\right] + \frac{dp}{dr} \tag{4.12}$$

where $f_r$ is the differential force of the blade on the fluid in the control volume. Defining $F_r$ to be the total force of the fluid on the blade, we have:

$$F_r = \int_o^i \varnothing r L f_r dr \tag{4.13}$$

With this convention, $F_r$ will be positive in the outward direction. Now, solving for $F_r$, we can write:

$$F_r = \int_o^i r\varnothing L\left[\rho\left(V_r \frac{dV_r}{dr} - \frac{1}{r} V_t^2\right) + \frac{dp}{dr}\right] dr$$

$$F_r = \int_o^i \left(\rho\varnothing L V_r dV_r - \varnothing L V_t^2 dr + r\varnothing L dp\right) \tag{4.14}$$

But the mass flow rate in the blade passage is

$$m = \rho \phi r L V_r \tag{4.15}$$

so $F_r$ can be written:

$$F_r = m \int_o^i dV_r - \int_o^i \rho \phi L V_t^2 \, dr + \int_o^i \phi r L \, dp \tag{4.16}$$

where
$$V_t = U + W_t$$
$$V_t^2 = U^2 + 2UW_t + W_t^2$$
$$V_t^2 = r^2 \omega^2 + 2r\omega W_t + W_t^2$$

Now, working with the third term in Eq. 4.16, we have:

$$\rho \phi L \int_o^i V_t^2 \, dr = \rho \phi L \int_o^i \left( (r^2 \omega^2 + 2r\omega W_t + W_t^2) \, dr \right) \tag{4.17}$$

Also, using the concept of rotary stagnation pressure (which follows from Bernoulli's equation for a rotating system), we can write:

$$p + \tfrac{1}{2}\rho(W^2 - U^2) = \text{Constant}$$
$$p + \tfrac{1}{2}\rho(V_r^2 + W_t^2 - U^2) = \text{Constant}$$
$$dp + \rho(V_r dV_r + W_t dW_t - U dU) = 0$$
$$dp = -\rho(V_r dV_r + W_t dW_t - U dU)$$

and
$$dp = -\rho(V_r dV_r + W_t dW_t - r\omega^2 dr) \tag{4.18}$$

Now, we can write the final term of Eq. 4.16 as

$$\phi L \int_o^i rdp = \phi L \int_o^i \rho( -rV_r dV_r - rW_t dW_t + r^2 \omega^2 dr)$$

$$= -m \int_o^i dV_r - \rho \phi L \int_o^i rW_t dW_t + \rho \phi L \omega^2 \int_o^i r^2 dr \qquad (4.19)$$

Combining the terms in Eq. 4.16 with the forms in Eqs. 4.17 and 4.19, we have

$$F_r = - \rho \phi L \int_o^i ( r^2 \omega^2 + 2r\omega W_t + W_t^2 ) dr$$

$$- \rho \phi L \int_o^i rW_t dW_t + \rho \phi L \omega^2 \int_o^i r^2 dr$$

$$F_r = - \rho \phi L \int_o^i (2r\omega W_t + W_t^2 ) dr - \rho \phi L \int_o^i rW_t dW_t$$

$$F_r = - \rho \phi L \int_o^i (2r\omega W_t dr + rW_t dW_t + W_t^2 dr) \qquad (4.20)$$

But since

$$rW_t dW_t + W_t^2 dr = W_t \, d(rW_t) \qquad (4.21)$$

$$F_r = - \rho \phi L \int_o^i \left( 2r\omega W_t dr + W_t \, d(rW_t) \right) \qquad (4.22)$$

$$F_r = -\int_o^i \frac{\rho \phi L r V_r}{r V_r} ( 2r\omega W_t dr + W_t \, d(rW_t))$$

$$F_r = -m \int_o^i \left( 2\omega \frac{W_t}{V_r} dr + \frac{1}{r} \frac{W_t}{V_r} d(rW_t) \right) \qquad (4.23)$$

Again, using the definition, $X = \frac{W_t}{V_r}$, we can write

$$F_r = -m \int_o^i 2\omega X \, dr + \frac{1}{r} X \, d(rW_t) \qquad (4.24)$$

But $$rW_t = \frac{rV_r W_t}{V_r} = \frac{m}{\rho \phi L} X$$

$$d(rW_t) = \frac{m}{\rho \phi L} dX \tag{4.25}$$

Thus

$$F_r = -m \int_o^i \left( 2\omega X \, dr + \frac{m}{\rho \phi L} \frac{X}{r} \, dX \right) \tag{4.26}$$

This can be integrated by our assumption that X varies linearly from the outside to the inside radius.

$$X = X_o - k (r_o - r)$$

$$dX = k \, dr$$

$$F_r = -m \left[ 2\omega \int_o^i X \, dr + \frac{m}{\rho \phi L} \int_o^i \frac{X}{r} \, dX \right] \tag{4.27}$$

Working with the first integral, we can write:

$$\int_o^i X \, dr = \int_o^i X \frac{dX}{k} = - \frac{(X_o - X_i)(r_o - r_i)}{2} \tag{4.28}$$

The second integral can be written:

$$\int_o^i \frac{X}{r} \, dr = \int_o^i \frac{X_o - k(r_o - r)}{r} \, k \, dr$$

$$= k(X_o - kr_o) \ln \frac{r_i}{r_o} + k^2 (r_i - r_o) \tag{4.29}$$

Combining Eqs. 4.28 and 4.29 with 4.26, we solve for $F_r$.

$$F_r = m \left[ (X_i + X_o) \omega (r_o - r_i) - \frac{m}{\rho \phi L} \left( k(X_o - kr_o) \ln \frac{r_i}{r_o} + k^2 (r_o - r_i) \right) \right] \tag{4.30}$$

or

$$F_r = m\left[(X_i+X_o)\omega(r_o-r_i) + \frac{m}{\rho\phi L}\left[k\left((X_o-kr_o)\ln\frac{r_o}{r_i} + (X_o-X_i)\right)\right]\right] \quad (4.31)$$

With the present assumptions, this analysis predicts an outward force, $F_r$.

## 4.4 BLADE FORCE CALCULATIONS

Two pitch angles, $\phi$, were used in the calculations; one assuming zero blade thickness, and the other accounting for the full blade thickness by neglecting the changes due to blade taper at the leading and trailing edges.

Two other assumptions about the flow are used. First, the mass flow rate per passage is needed and this was assumed to be the total flow rate divided by the number of passages in the nozzle enclosed angle (in this case 5.5). Secondly, the relative entry angle, $\beta$, was assumed to be constant over the nozzle exit area and was calculated by using the velocity triangle relationships (see Fig. 12) as follows:

$$V_r = -V \sin\alpha$$

$$W_t = V\cos\alpha - U$$

$$= \tan^{-1}\left(\frac{V\cos\alpha - U}{-V\sin\alpha}\right) \qquad \text{where} \quad V = \frac{Q}{sL}$$

With these fairly simple assumptions, the blade forces could be calculated as a function of flow rate.

## 4.5 NONDIMENSIONALIZATION OF BLADE FORCES

Equations 4.11 and 4.31, which give the tangential and radial forces on the blades, can be nondimensionalized using flow rate, speed, turbine geometry and water density. Taking the geometry of the turbine into account, a nondimensional force coefficient, $F_1$, can be written as:

$$F_1 = \frac{F}{\rho\omega^2 LD^3}$$

and the flow rate can be written in terms of a flow coefficient, FC, which is defined as:

$$FC = \frac{Q}{\omega LD^2}$$

With this nondimensionalization, Eqs. 4.11 and 4.31 for the tangential and radial forces may be expressed in functional form as simply

$$\frac{F_t}{\rho\omega^2 LD^3} = f\left(\frac{Q}{\omega LD^2}\right)$$

and

$$\frac{F_r}{\rho\omega^2 LD^3} = f\left(\frac{Q}{\omega LD^2}\right)$$

The results of the blade force analysis are presented in this nondimensional form in the following chapter, where they are compared with the experimental results.

# Chapter V

# EXPERIMENTAL RESULTS

## 5.1 TURBINE CHARACTERISTICS

The performance of the turbine is shown by three curves which show the efficiency, nondimensional power and nondimensional flow rate as a function of nondimensional speed. For a particular turbine geometry:

$$\eta \,,\ \frac{P}{H^{1.5}} \,,\ \frac{Q}{\sqrt{H}} = f\left(\frac{N}{\sqrt{H}}\right)$$

For a geometrically similar machine, these may be made fully dimensionless by writing as follows:

$$\eta \,,\ \frac{P}{\rho(2gH)^{1.5}LD} \,,\ \frac{Q}{\sqrt{2gH}\,LD} = f\left(\frac{U}{\sqrt{2gH}}\right)$$

The efficiency curve, Fig. 13, shows that the optimum speed, $N_1$, is in the range of 0.47. The peak efficiency at this point is between 65-70%, depending on the head. It can be clearly seen that the highest efficiencies are at the lowest head, and that they consistently decrease as the head increases. This is thought to be largely due to referencing

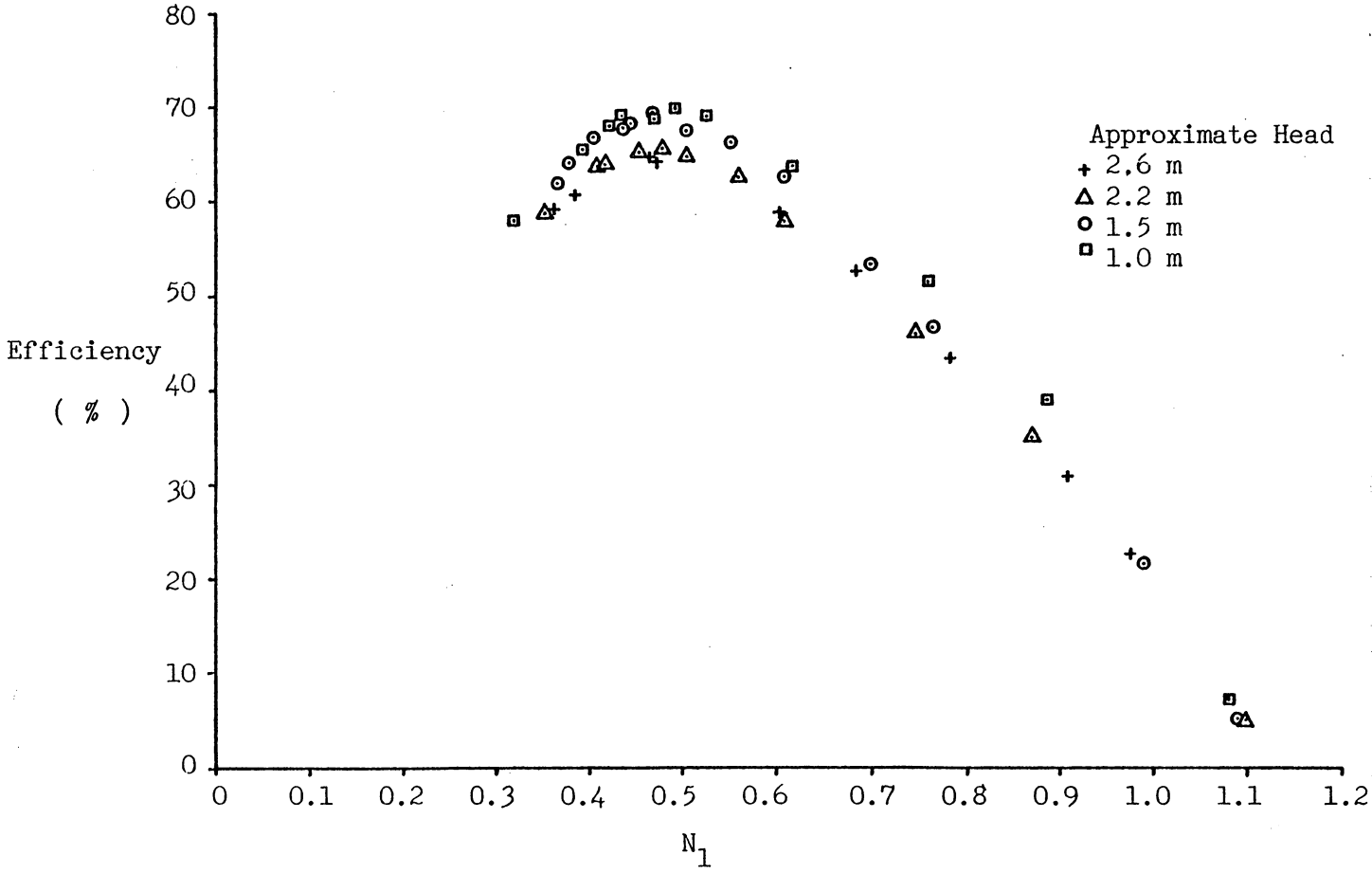


Figure 13: Turbine Efficiency

head to the turbine shaft, rather than the bottom of the runner. It might also have occurred because the casing was very close to the runner and at higher heads and flow rates there was more interference. The lowering of efficiency with an increase in head is also shown by Johnson [12].

At all heads, the efficiency was lower than that published by others [12,13]. This may be partly due to a substantial amount of water (possibly 5% of the total) escaping from the nozzle-runner gap. A 5% increase in efficiency would put the peak efficiency in the 70-75% range, which could be expected since large cross-flow turbines are in the 83% efficiency range [15].

From the range of nondimensional speeds, it can be seen that the runaway speed is on the order of 235 percent that of the optimium speed. This is somewhat higher than the 180 percent mentioned by Stapenhorst [15].

The nondimensional flow rate, Fig. 14 shows that at normal operating speeds, the flow rate is nearly independent of changes in speed, with only a small, linear decrease in flow for increasing speed.

However, at high $N_1$, the flow rate decreases non-linearly which may be due to reaction effects within the runner. The nondimensional flow is the lowest for low heads and highest for high heads, but the difference is very small (within 2%).

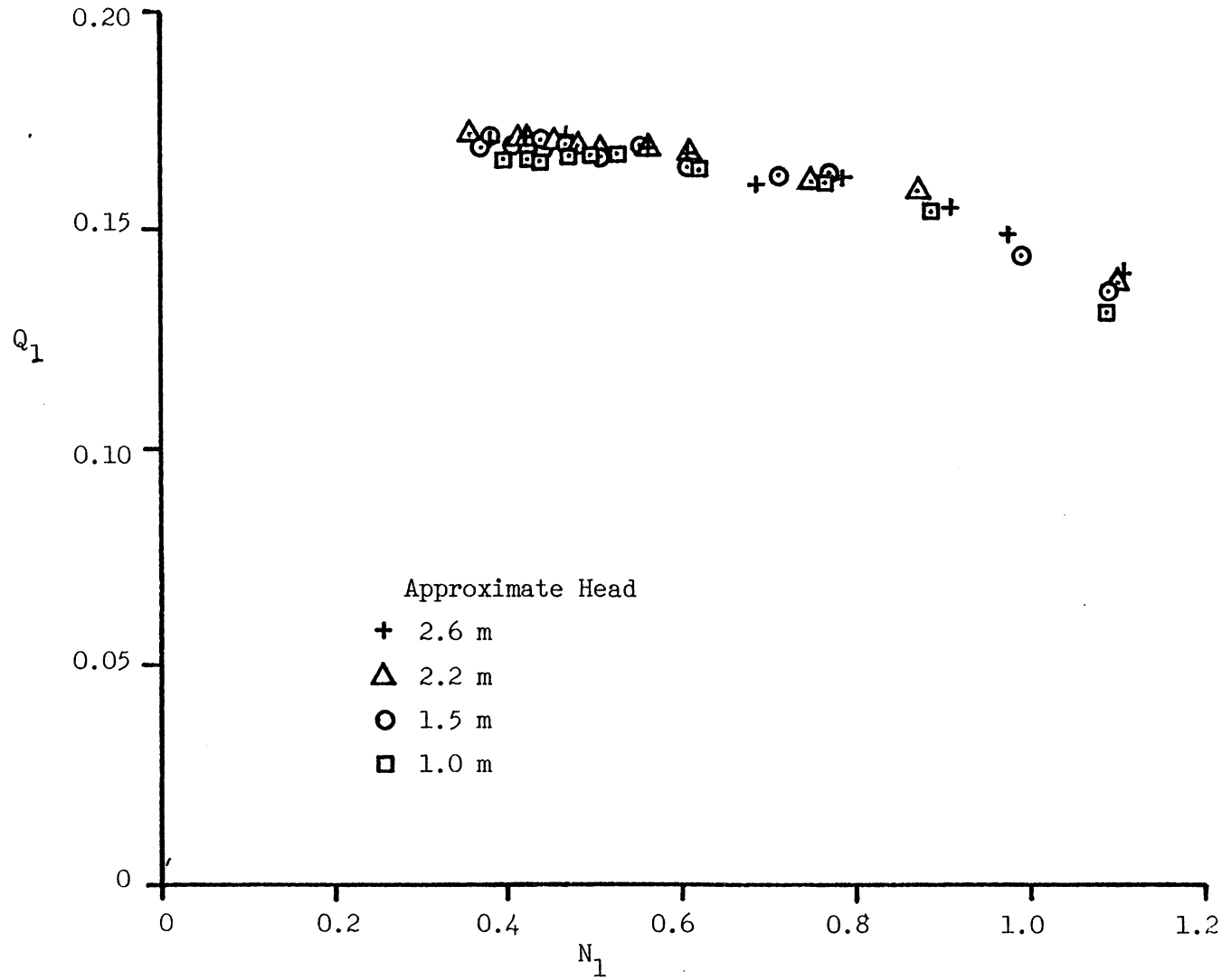


Figure 14: Turbine Flow Rate

The experimental flow rate was found to be substantially different from that predicted by the free-jet calculations. To calculate the actual flow using the free-jet (as in Eq. 2.1), the nozzle coefficient, $C_1$, would need to be 0.83. The theoretical calculation predicted a flow rate 17% higher than the actual.

The nondimensional power curve (Fig. 15), again shows a slight spread (about 5%) between low and high heads. The pattern is consistent with that shown by the efficiency curves. The peak power comes at a nondimensional speed of 0.47, which is at the same speed as the peak efficiency. This contrasts with the results shown in reference 13 which show peak power at a slightly lower speed than peak efficiency.

## 5.2 FLOW CHARACTERISTICS

### 5.2.1 Nondimensional Speed and Flow Coefficient

The flow characteristics through the turbine were observed by using a stroboscope to visually stop the motion. Also, photographs were taken of the flow. Before dealing with these, however, it is helpful to relate the nondimensional speed, $N_1$, to the flow coefficient, FC, which is used in the force calculations.

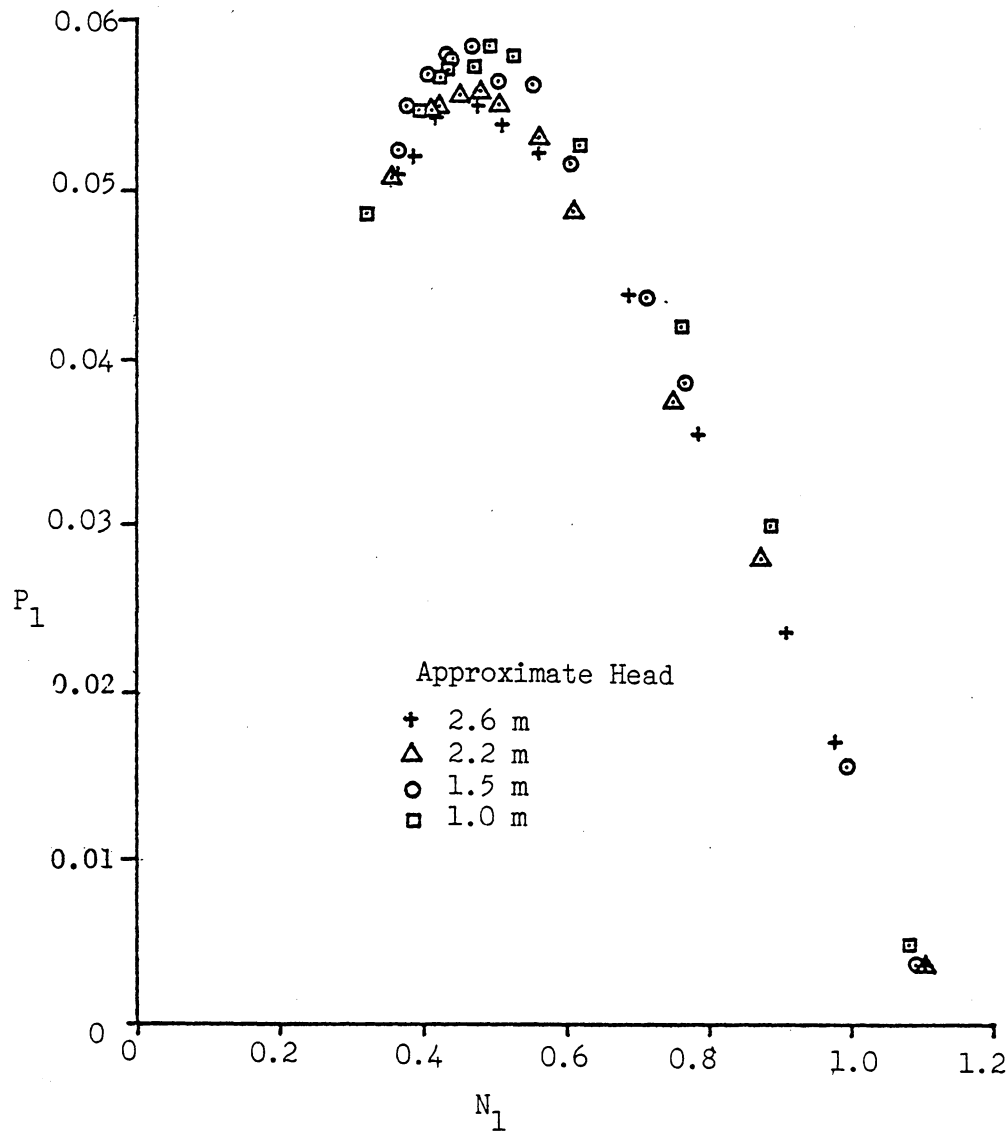


Figure 15: Turbine Power

$Q/N$ is the flow coefficient that relates the flow to the rotational speed. It was made entirely dimensionless by taking the runner diameter and length into consideration, and was expressed as $FC=Q/\omega LD^2$. However, when working with a turbine, the head, not the flow, is the primary parameter. But, if the head is specified, the flow rate is difficult to determine analytically. The nozzle coefficient is unknown and cannot be adequately approximated as 1.0. The flow calculation would be elliptic, taking the reaction effects of the runner into account. However, the two parameters, FC and $N_1$ may be related experimentally as shown in Fig. 16. This figure shows the relationship between $N_1$, which has been used in analyzing the turbine characteristics, and FC, which is used in calculating the blade forces.

### 5.2.2 Flow Visualization

In observing the flow, the incidence angle concept is very useful. The incidence angle can be defined as the difference between the blade angle and the relative velocity (velocity of the flow relative to the blade) angle at the runner inlet, as shown in Fig. 17. The blade angle is fixed at 30 degrees, but the relative velocity angle varies with the flow rate and speed. If we assume that the absolute flow enters at the nozzle angle (15 degrees), then the incidence

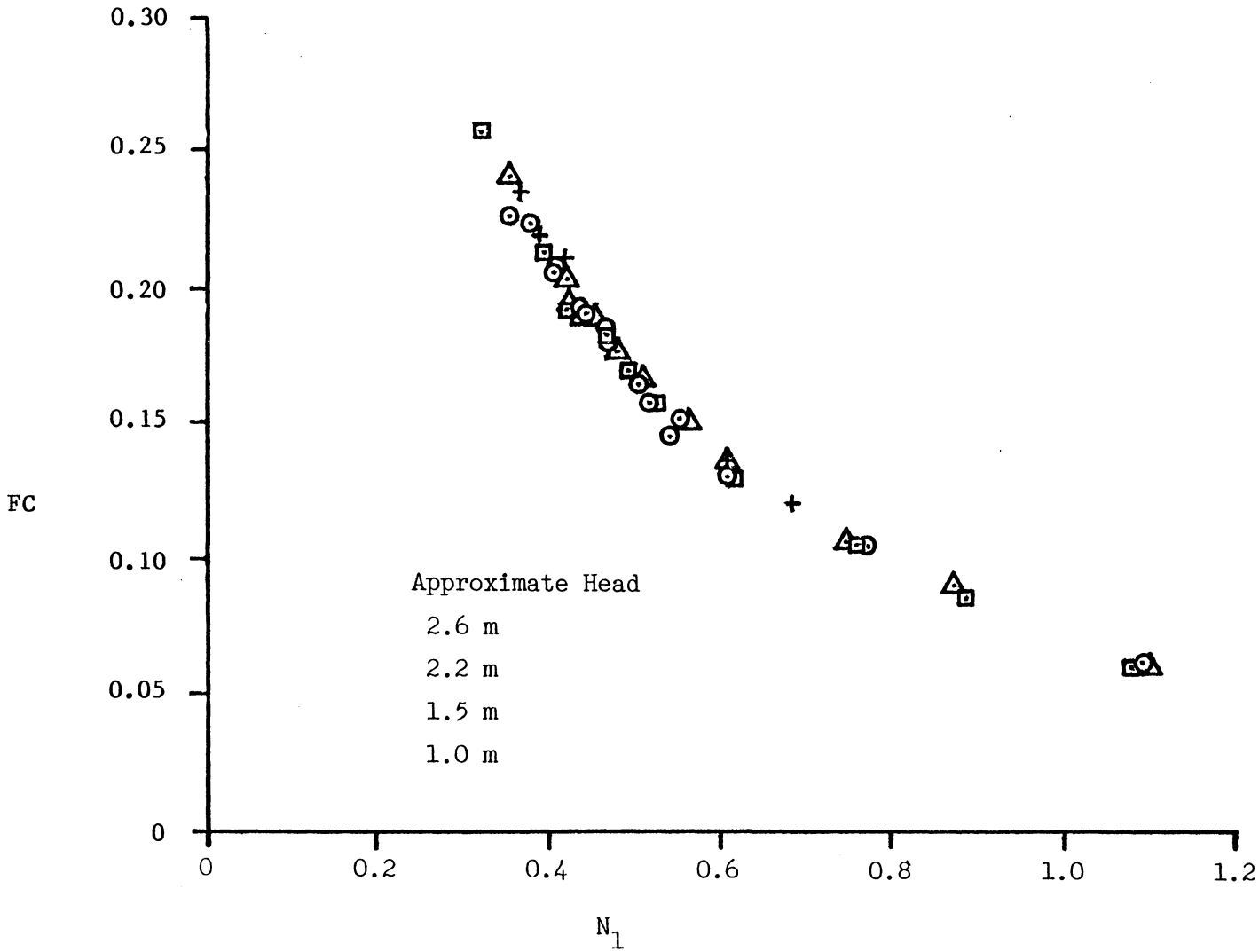


Figure 16: Nondimensional Speed and Flow Coefficient

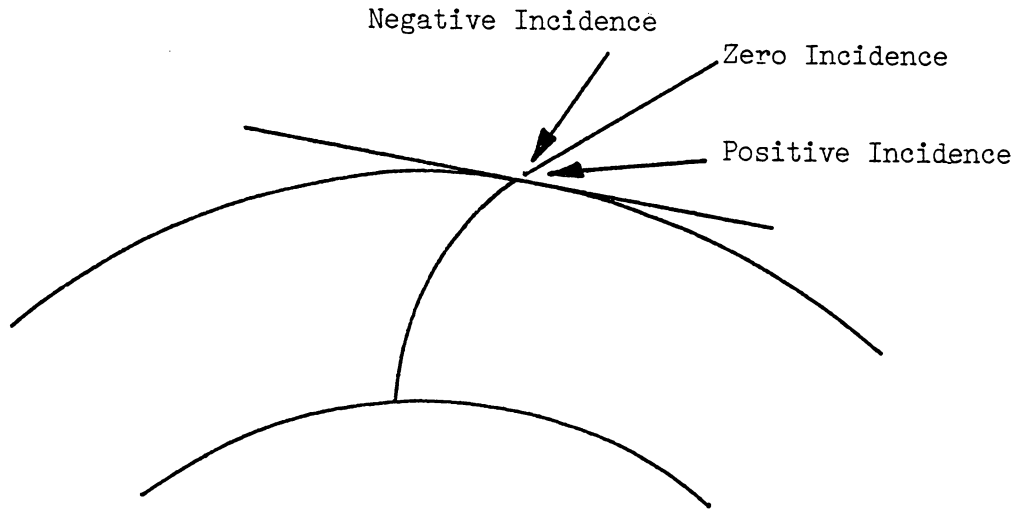


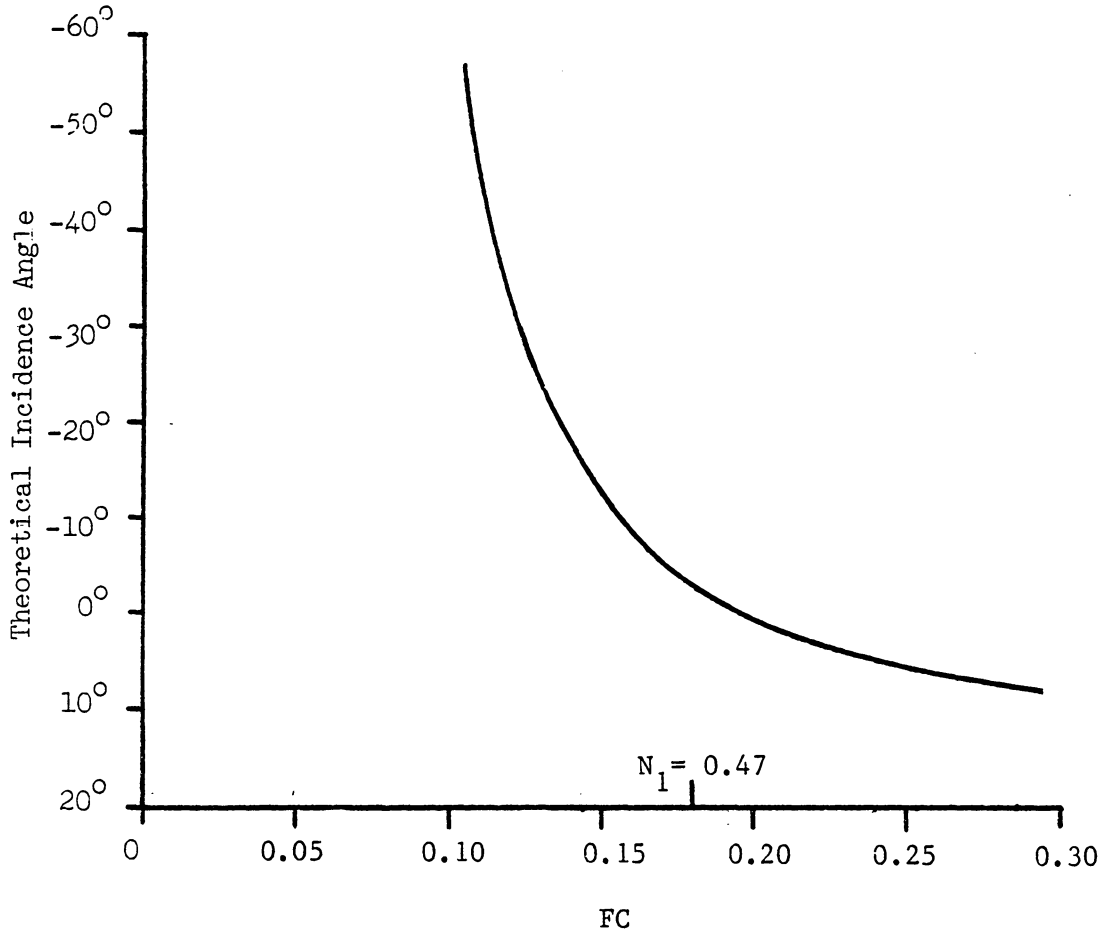


Figure 17: Theoretical Incidence Angle

angle can be calculated, which is also shown in Fig. 17. It should be noted that this is an analytic expression. Nakase, et al. [13] show that the absolute velocity is nonuniform across the nozzle and does not exactly follow the nozzle angle, but this calculation is useful in understanding the flow even if the actual incidence angle is unknown. From Fig. 17, we can see that the optimum speed is very close to zero incidence. This should be expected since at zero incidence the entrance losses will be minimized.

The flow was observed by using a stroboscope set to flash 22 times (the number of blades) per revolution. The stroboscope was set behind the turbine so the water flow was backlighted and clearly visible. Only the region after the nozzle outlet was difficult to observe, since water would splash between the runner and the plexiglas casing.

Figures 18-21 are sketches of the flow over a range of nondimensional speeds, $N_1$, from 0.37 to 0.64. Figure 18 shows the turbine at a very slow speed. At such low speeds, the flow is highly turned by the first pass through the runner and nearly interferes with the turbine shaft. Also, at this point, the incidence angle is positive and it is observed that the flow separates off the suction side of the blades. Only when the blade passage approaches the nozzle exit does the flow completely fill the passage.

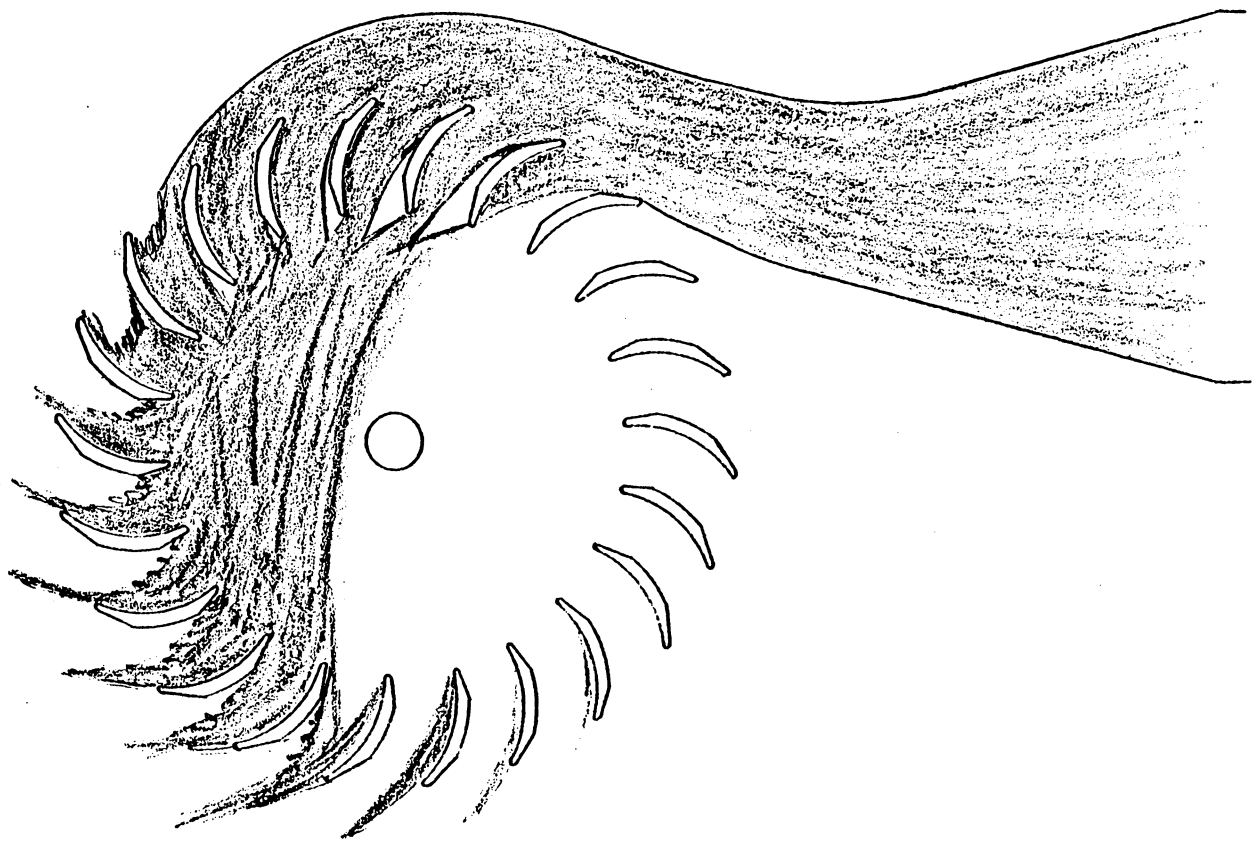

Figure 18: Flow Visualization at $N_1$=0.37

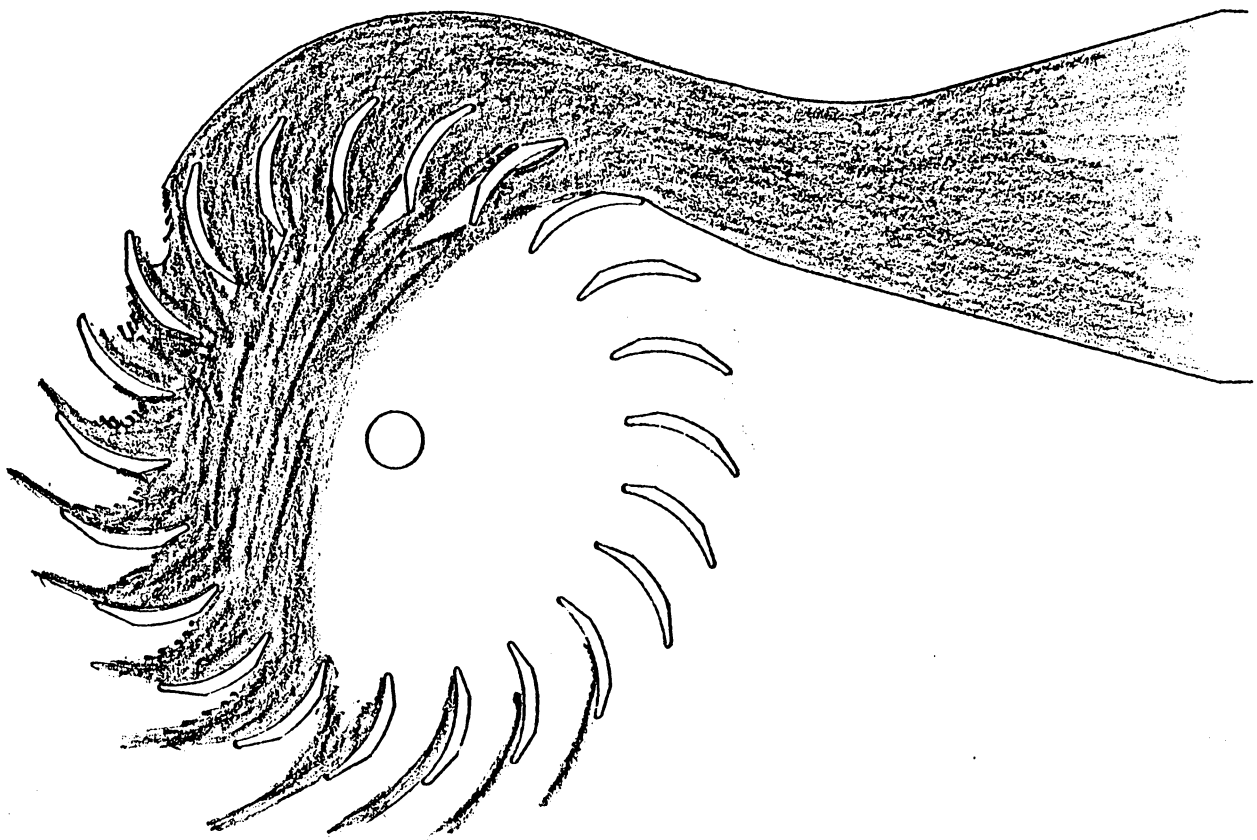

FIgure 19: Flow Visualization at $N_1$=o.43

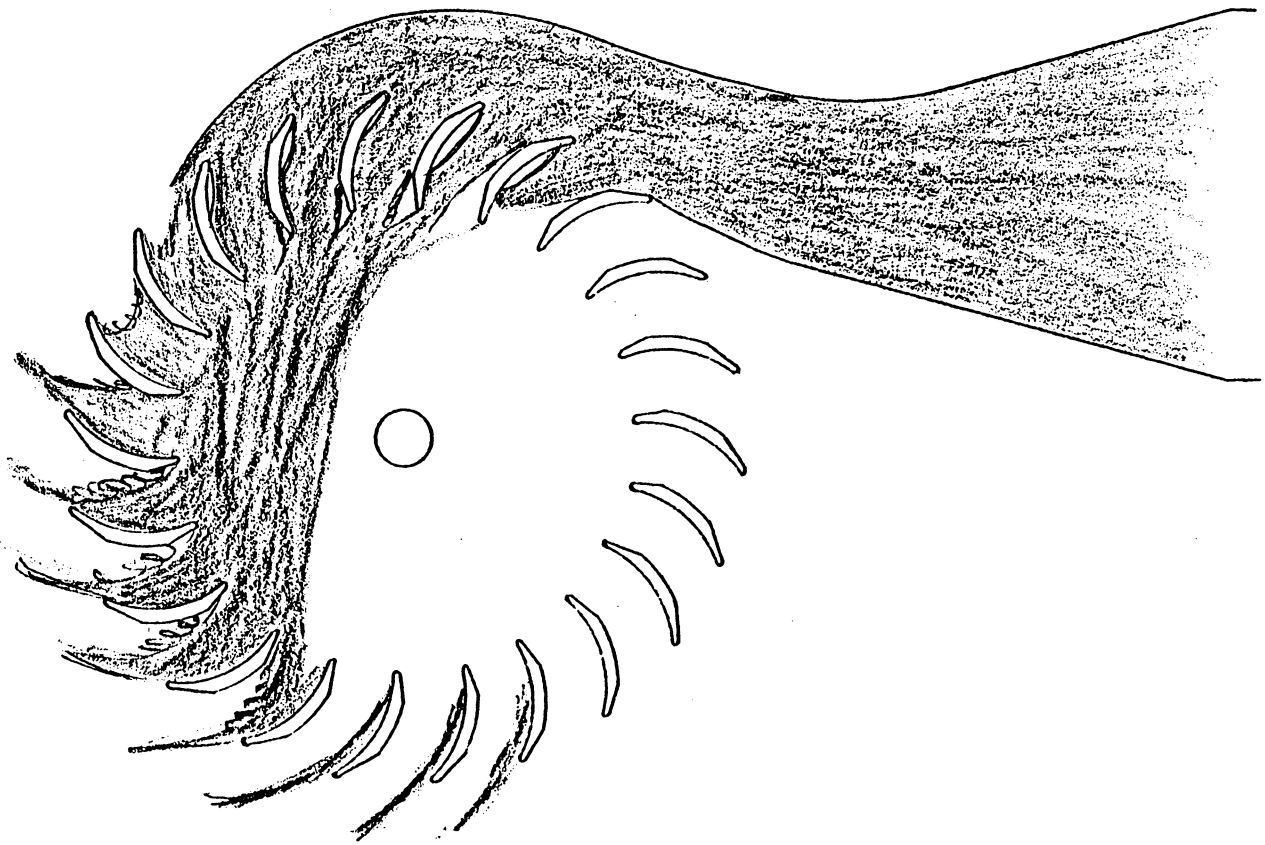

Figure 20: Flow Visualization at $N_1$=0.51

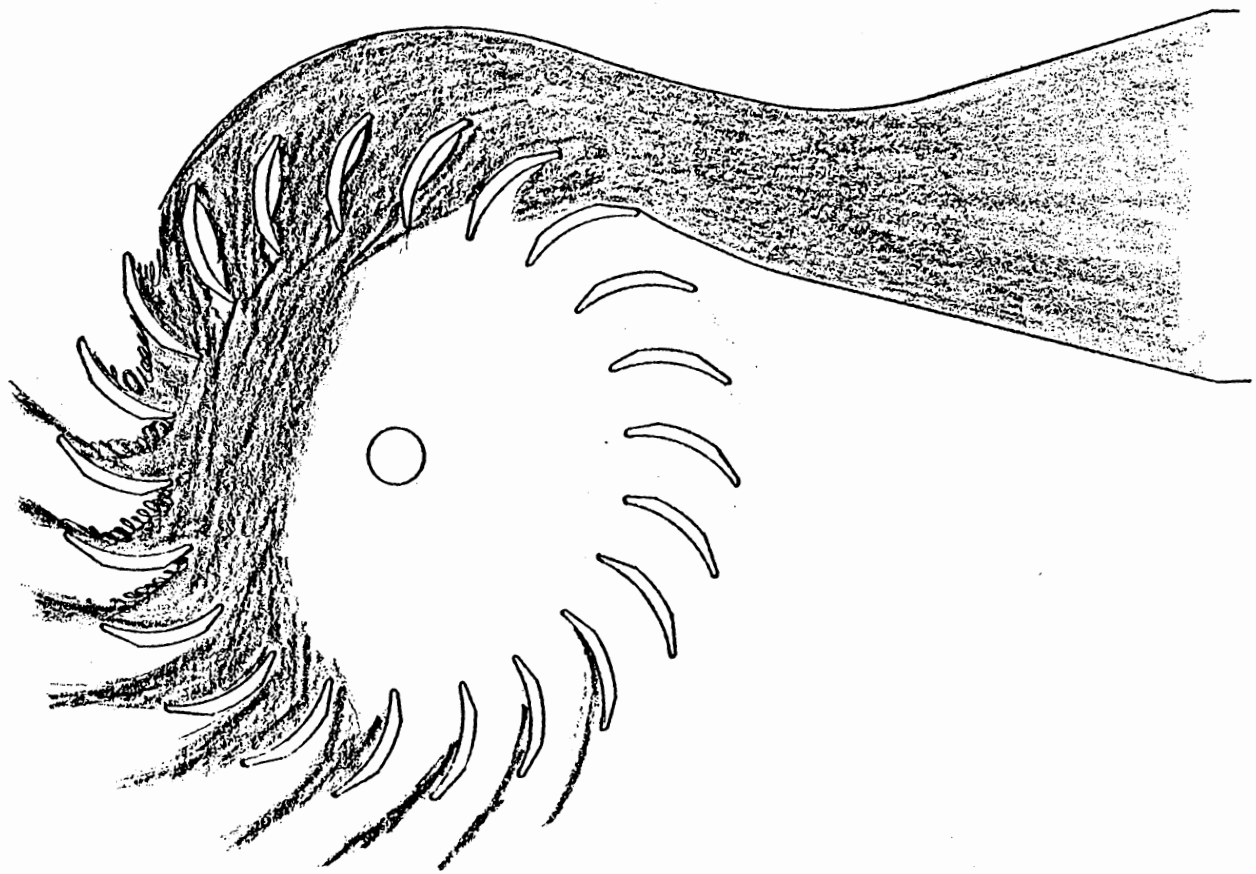

FIgure 21: Flow Visualization at $N_1$=0.64

Figures 19 and 20 show the turbine at nearly optimum speed. The flow is still turned in the first pass, but not as much as at the very slow speed. Figure 19 shows that the incidence angle is nearly zero, because in the nozzle exit the runner passages are nearly full. There is only slight separation on the pressure side of the blade near the leading edge when first entering the nozzle and slight separation off the machined flat near the trailing edge on the suction side of the blades. At this point, the full-passage assumption of the analysis in Chapter 4 appears well-justified. Figure 20 shows the increasing tendency of a negative incidence angle to cause separation on the pressure side of the blades near the leading edges. The passages are nearly full, but there are small pockets of air on the pressure side because of the negative incidence angle.

Figure 21 shows the flow pattern at a high speed ($N_1$=0.64). The flow is not turned as much through the first pass as at slower speeds. Also, the large negative incidence angle can be clearly seen as large separated regions on the pressure side. Flow is impeded and the blade passage never gets completely filled. The blockage of the flow by the air pocket appears to be about 20%.

In summary, as the speed goes from low to high, the turning on the first pass through the rotor decreases, and

the incidence angle changes from positive to negative causing separation off the suction side of the blades, to little separation, to separation off the pressure side of the blades.

On the second pass (flow from inside to outside) the flow was highly turbulent because of interference between the flow from different passages. At all speeds, the flow separated off the suction side of the blades and never filled the passage. Using the stroboscope, the relative flow from the runner appeared to leave at the blade angle.

These effects can also be seen in Figs. 22-24, which are photographs of the flow over a range of $N_1$ from 0.31 to 0.64. The amount of turning in the first pass, as well as the separation at various points within the blade passage can be seen. The leakage from the nozzle-runner gap is also clearly visible. The photographs were taken using a flash attachment to backlight the runner.

## 5.3 BLADE FORCES

### 5.3.1 Mechanical Forces

In the experimentation, it was essential to separate the fluid forces from the mechanical forces on the blades. The test blade had added mass because of the strain links and mounting shafts. Also, other blade designs are not a pipe

Figure 22: Photograph of Flow at $N_1$=0.31

Figure 23: Photograph of Flow at $N_1$=0.48

Figure 24: Photograph of Flow at $N_1$=0.64

section, but sheet steel which is much lighter. For design purposes, it is preferrable to know the fluid forces and add on the centrifugal forces for a given blade mass.

There is a torque associated with rotational speed because the inner half of the blade is more nearly in line with the radius through the blade axis than the outer half, as shown in Fig. 25. The centrifugal forces due to the blade mass were found by spinning the runner with no water flow and recording the radial force and blade torque. Figure 26 shows the radial force as the runner speed decreases. This is not a constant value because the speed is decreasing (showing the overall trend) and because the blade weight adds and then subtracts from the total force (giving the sinusoidal variations). The equivalent blade weight is defined as the equivalent weight of the blade and strain links concentrated at the center of the blade and was found to be 2.72 N. The mean mechanical force (which corresponds to the centrifugal force) was determined at several speeds. The speeds were found by measuring the period indicated by the blade weight. Centrifugal force and torque are shown as a function of rotational speed in Figs. 27 and 28. It can be seen that the forces vary as the square of speed, as expected.

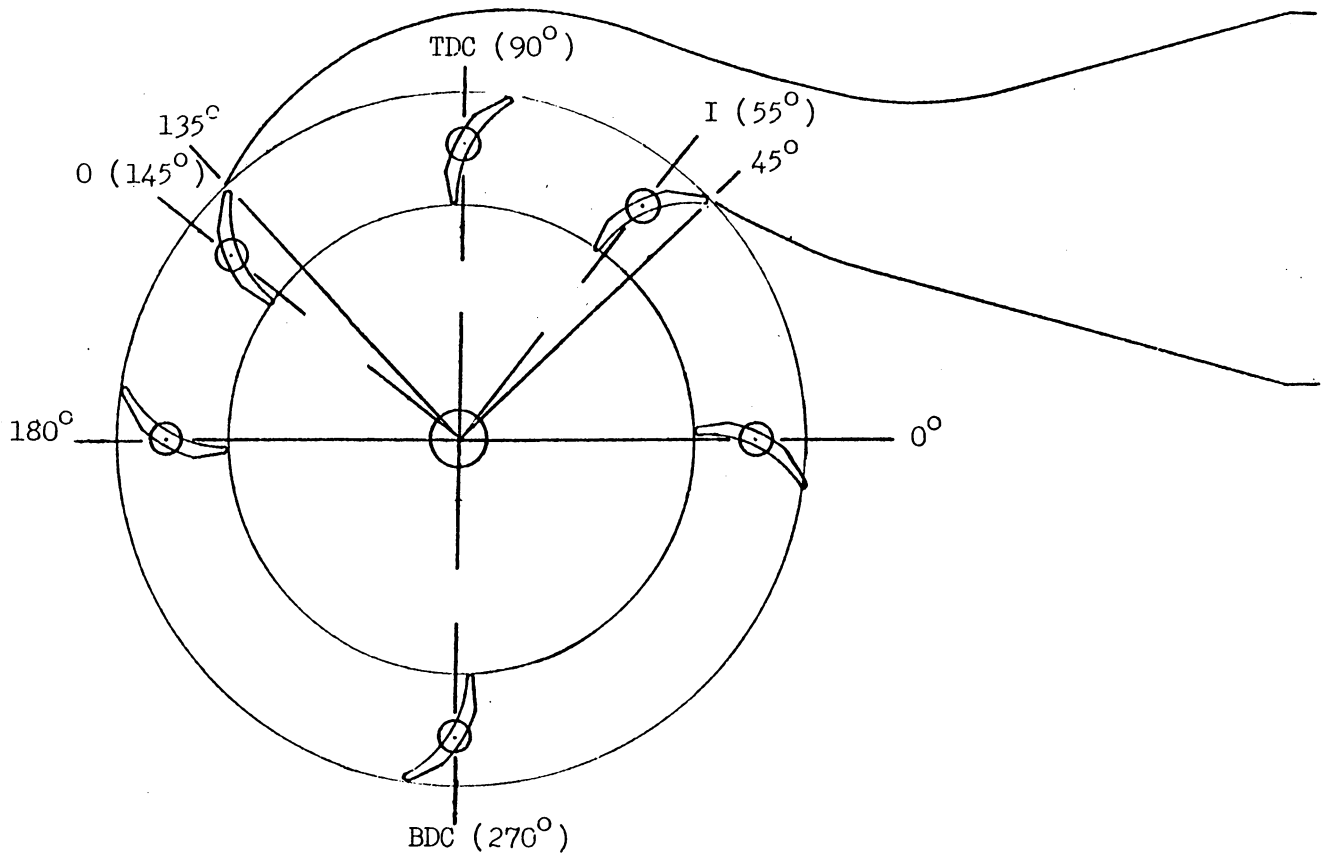


Figure 25: Notation for Blade Position

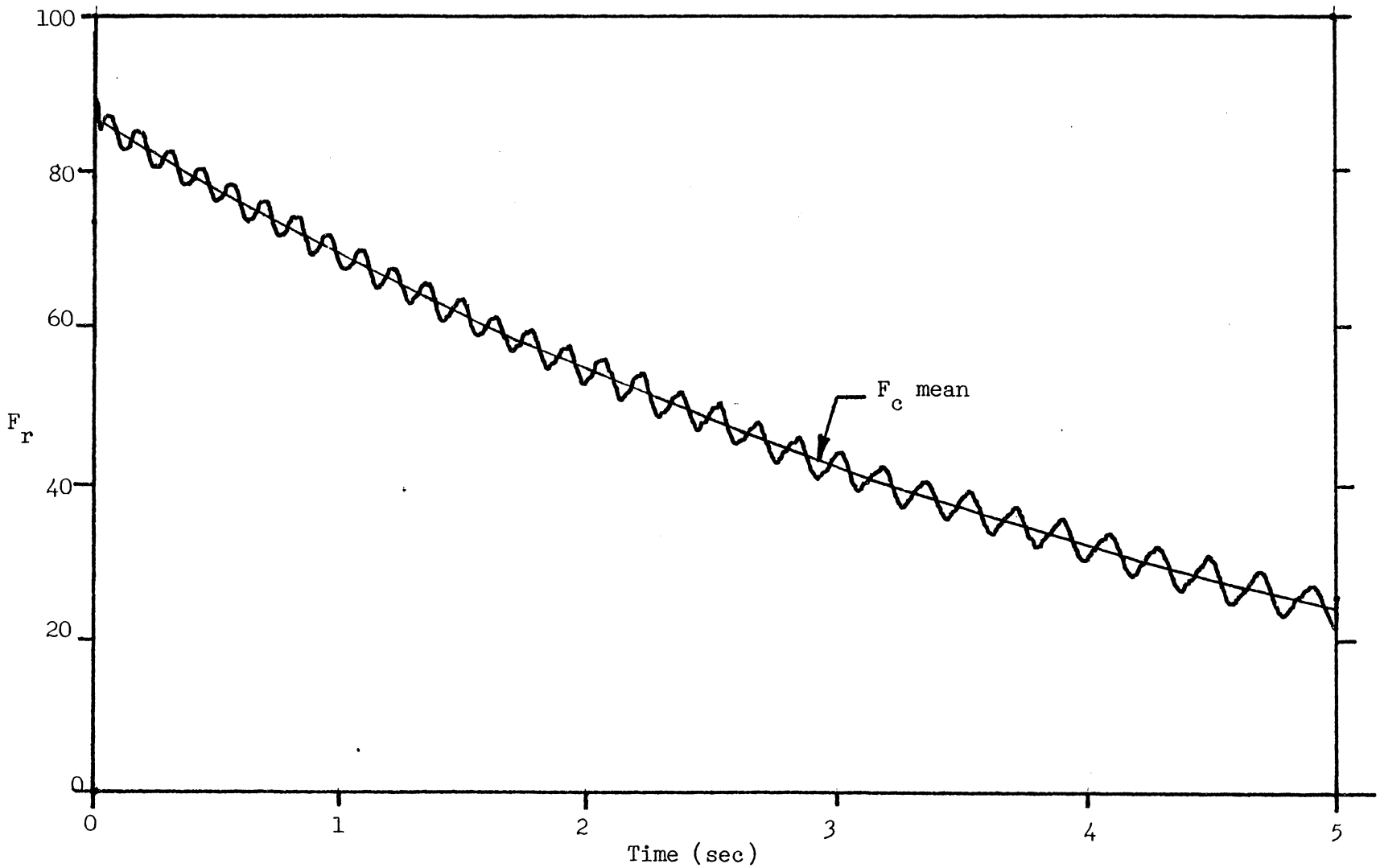


Figure 26: Radial Force at Varying Speed

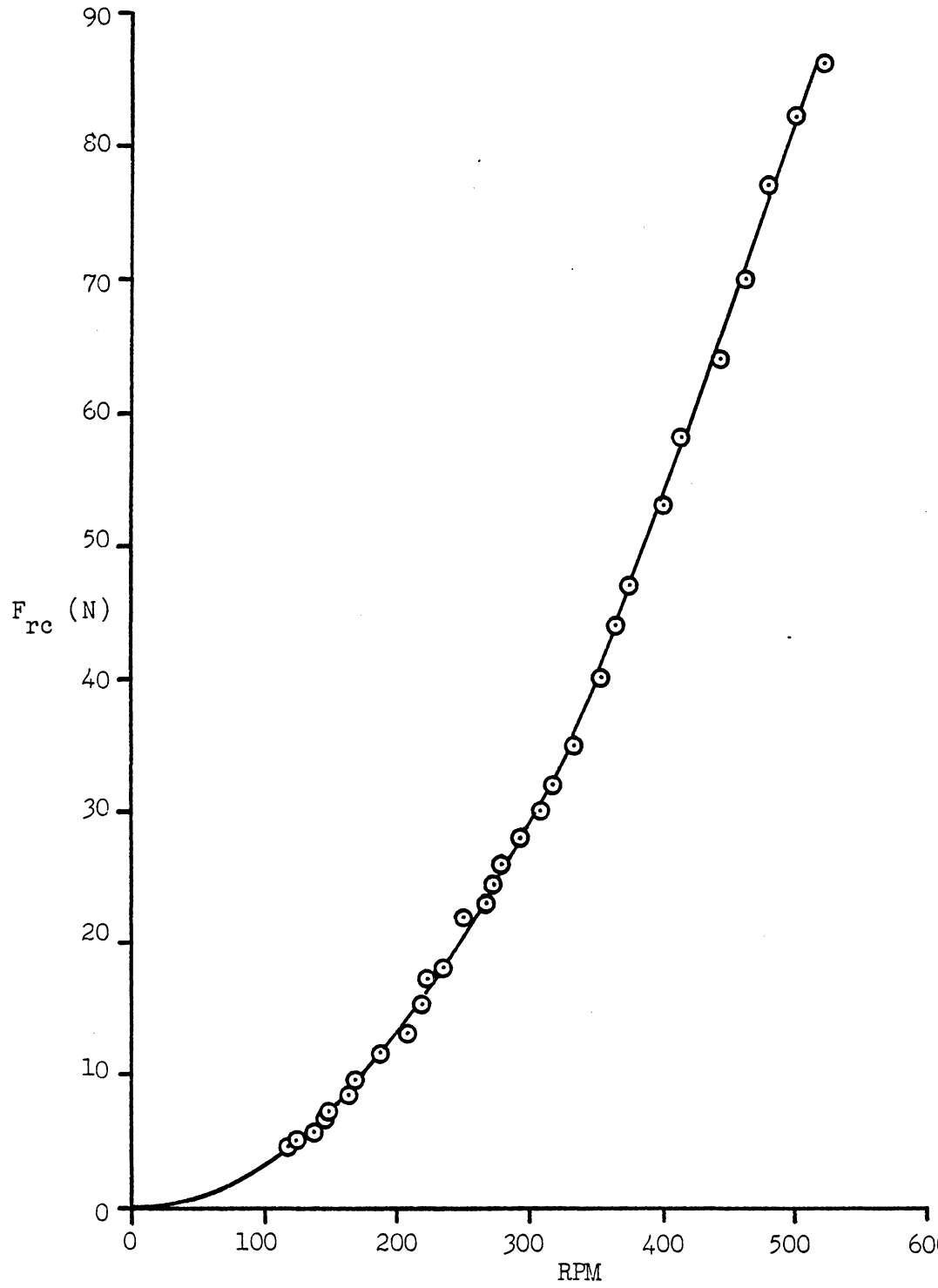


Figure 27: Blade Force due to Rotational Speed

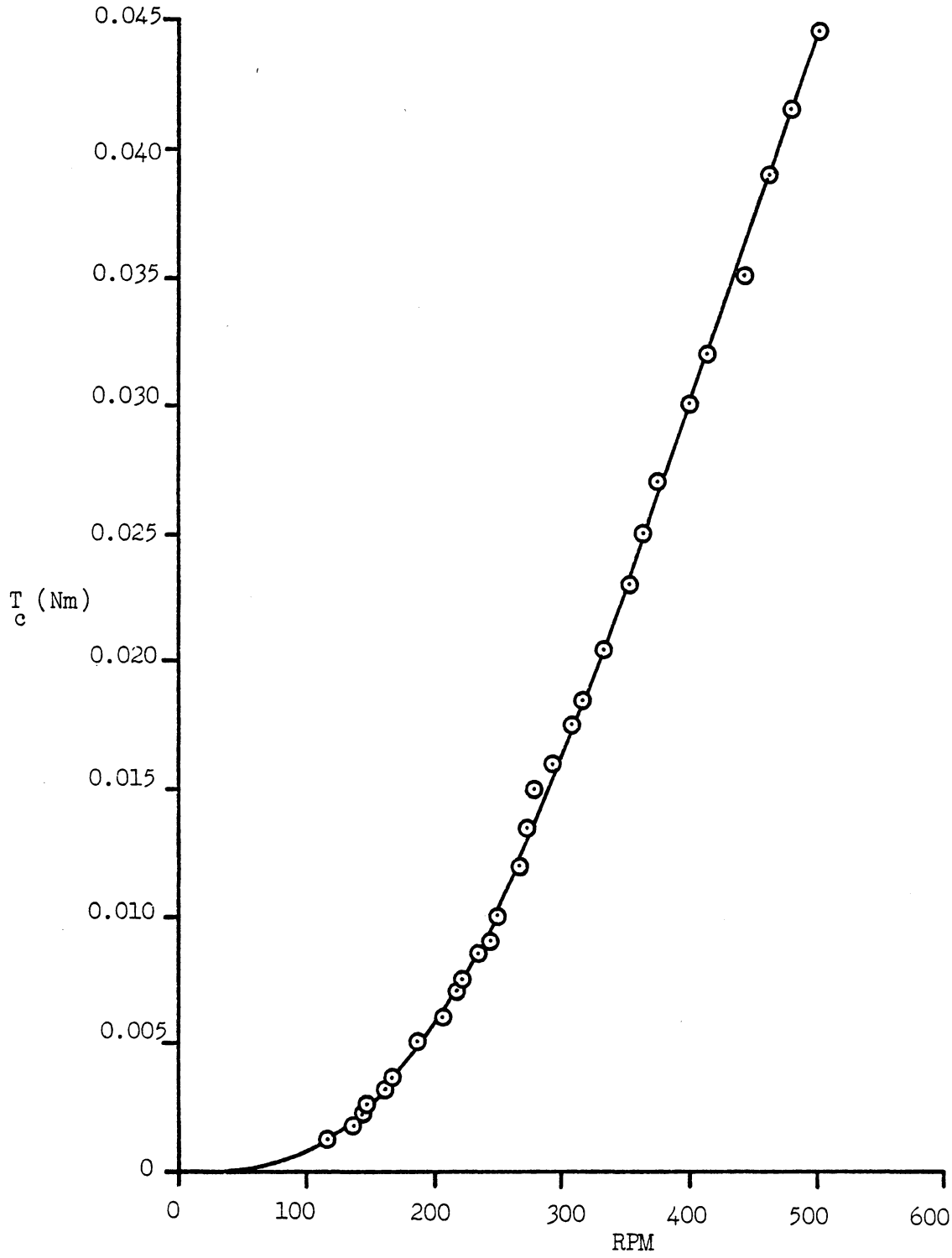


Figure 28: Blade Torque due to Rotational Speed

### 5.3.2 Pattern of Blade Loading

#### 5.3.2.1 Forces at Optimum Speed

The turbine was run following the procedure described in Chapter 3, and the forces were recorded on the digital oscilloscope. The forces can be analyzed showing the pattern of blade loading over a cycle, giving insight into the flow through the turbine and the magnitude of forces.

The notation used for the blade position is shown in Fig. 25. Figures 29-31 show the tangential and radial forces, and the blade torque.

Figure 29 shows that the tangential force starts at slightly below zero because the blade weight is in the negative direction at that point and possibly because of air drag or water shedding. When the blade enters the nozzle, the force increases rapidly until it reaches a plateau near 30 N. This is the area where the blade passage is full.

Ten degrees (about half a passage width) before the blade leaves the nozzle exit, there is a sudden increase in force. This can be explained by the static pressure in the nozzle area being greater than the atmospheric pressure outside the nozzle, perhaps caused by a small reaction of the blading. By the flow visualization done earlier (Figs. 18-23), we can see that just before the blade leaves the nozzle, the passage is not full. Thus, when the blade is

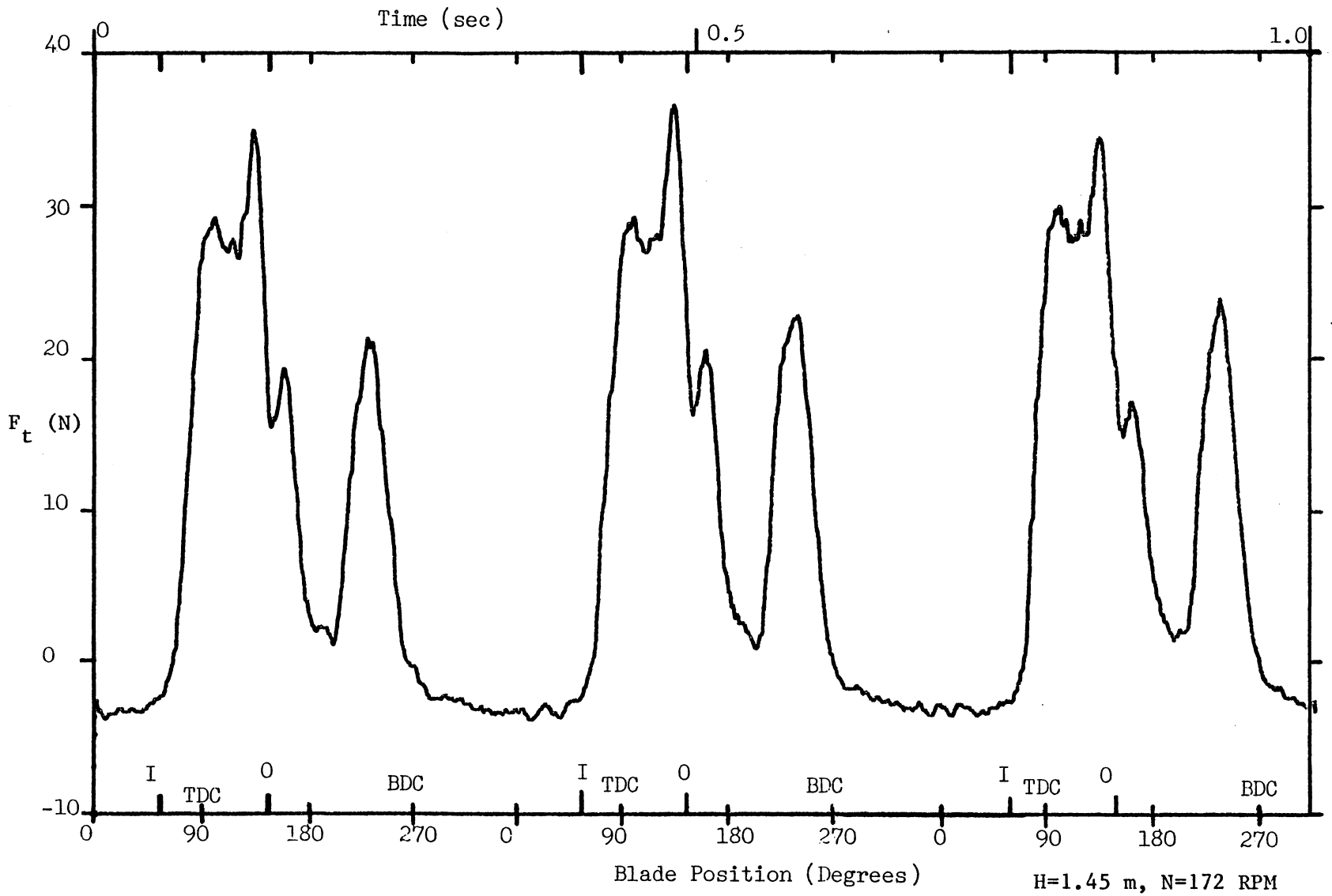


Figure 29: Tangential Blade Force

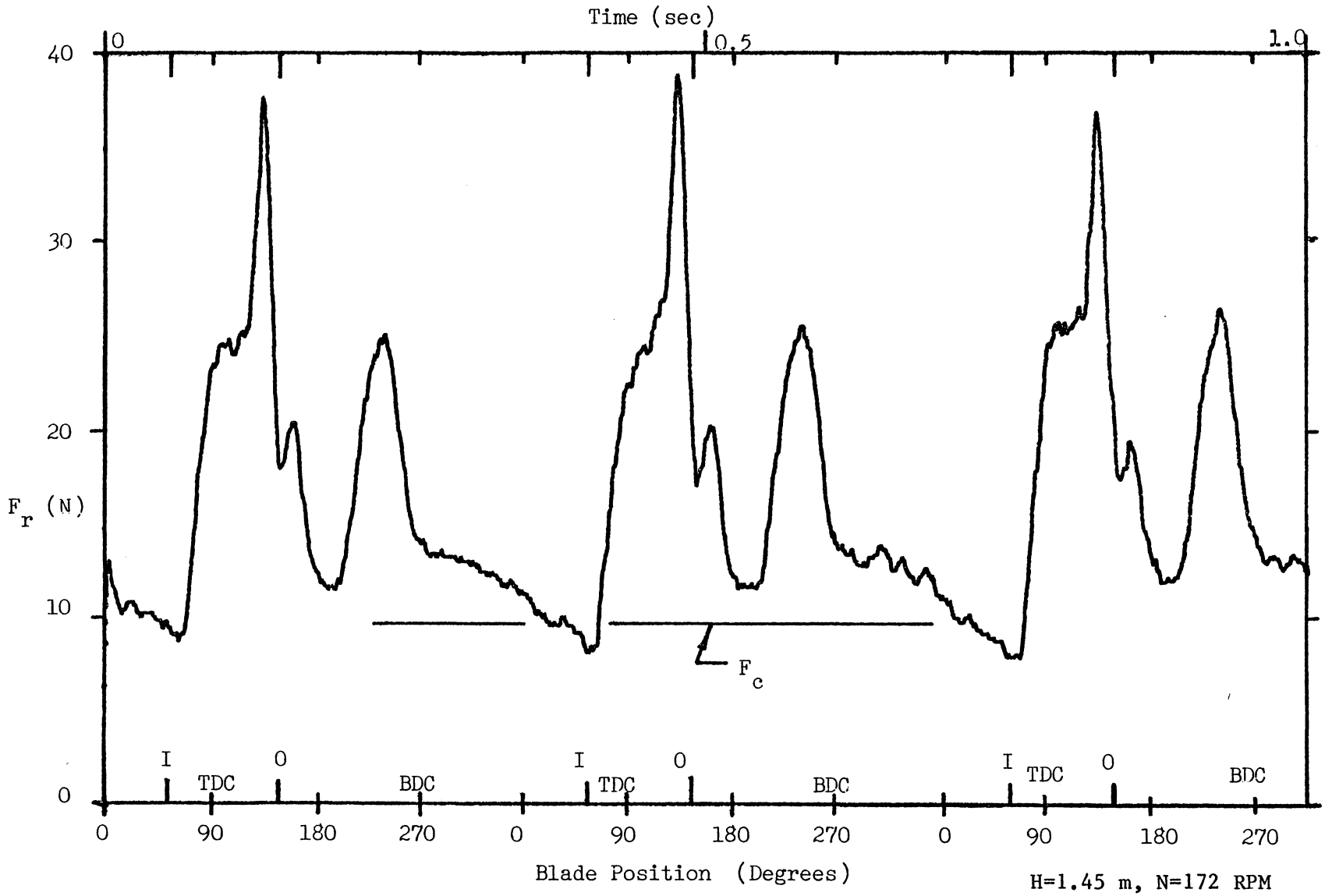


Figure 30: Radial Blade Force

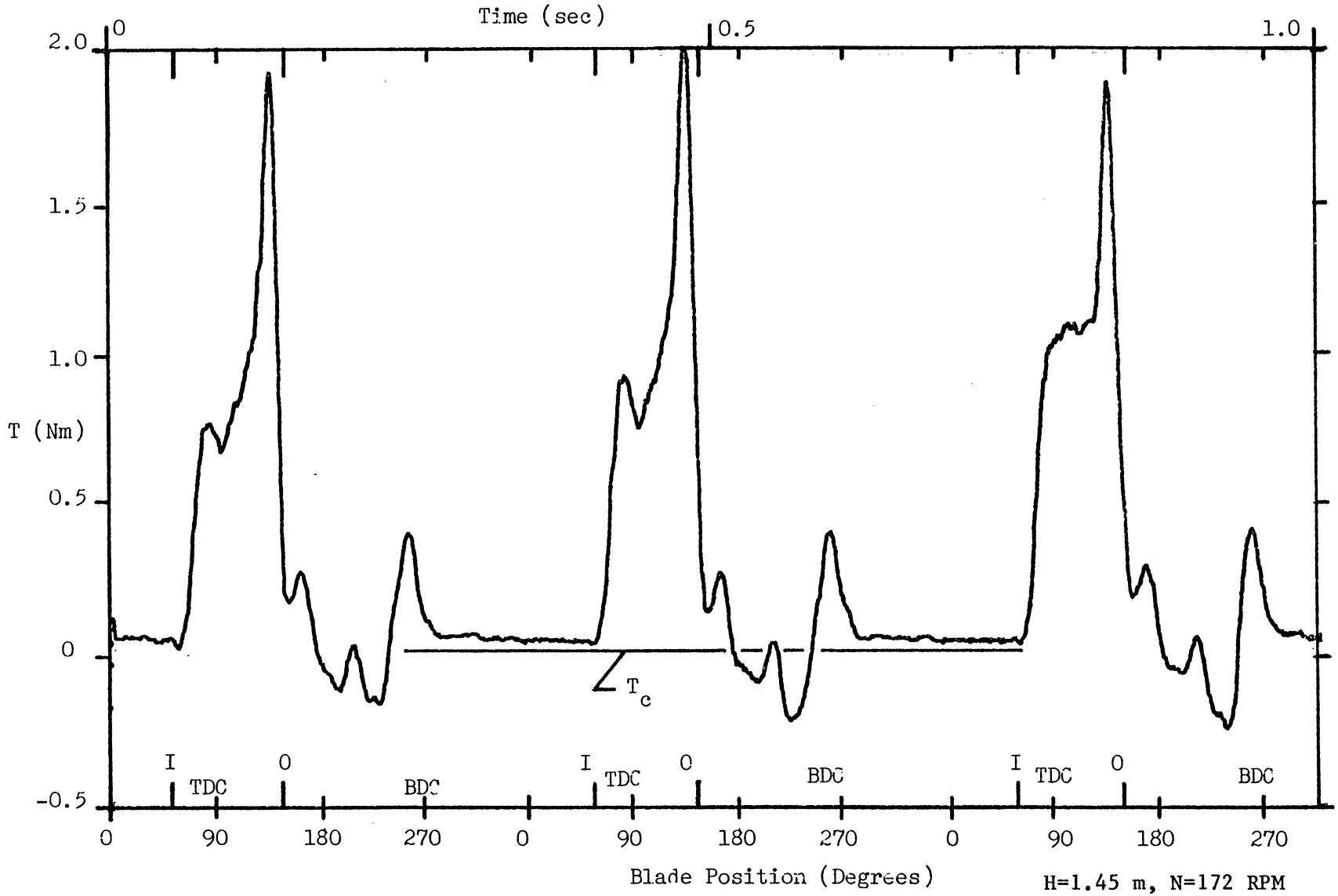


Figure 31: Blade Torque

nearing the nozzle exit, the passage on the back of the blade empties and is at atmospheric pressure, while the passage on the front of the blade is full and at greater than atmospheric pressure. This creates a surge in the force on the blade.

As the runner continues turning, the tangential force drops off. Then, the characteristic feature of the cross-flow turbine can be seen. The flow again passes through the runner, giving additional force to the runner. At optimum speed, the second pass provides about 25% of the total power.

Figure 30 shows a similar behavior of the radial force. When the blade enters the nozzle, the radial force increases rapidly. It also reaches a plateau when the blade passage is full. Then nearing the nozzle exit, there is the characteristic spike due to the pressure differential.

The effect of the blade weight on the total force can also be seen quite clearly from Fig. 30. The mean centrifugal force is 9.8 N and the blade weight of 2.72 N gives a variation about that value. When the runner is in the BDC position, the blade weight adds to the centrifugal force, when it is halfway between TDC and BDC it is nearly zero, and as it approaches TDC the blade weight subtracts from the centrifugal force.

Figure 31 shows that when the blade enters the nozzle it is given a positive torque of 0.7-1.1 Nm, implying a positive incidence angle. The characteristic spike near the nozzle exit doubles the torque to nearly 2.0 Nm. The torques involved with the second pass of the water through the runner are relatively small. Also, the torque due to the rotational speed (0.04 Nm) is shown to be small and close to that shown at points where there is no water in the runner.

#### 5.3.2.2 Forces at Varying Heads

It is expected that the magnitude of blade forces increase as head increases. Figures 32-35 show the tangential and radial forces and the blade torque as the head varies from 1.0 to 2.6 m. These figures show the variation in the forces, and also that the patterns are much the same. Comparing the relative amplitudes of the first and second pass, we can see that the tangential forces are very similar. The radial forces are also very similar except at the lowest head, 1.0 m, where the second pass plays a much larger role. Evidently at a very low head, the drop across the rotor adds substantially. This effect does not appear in the rest of the head range studied. From the torque plots, it can be seen that the pattern is much the same, except the spike near the nozzle exit is a larger percentage of the total torque at

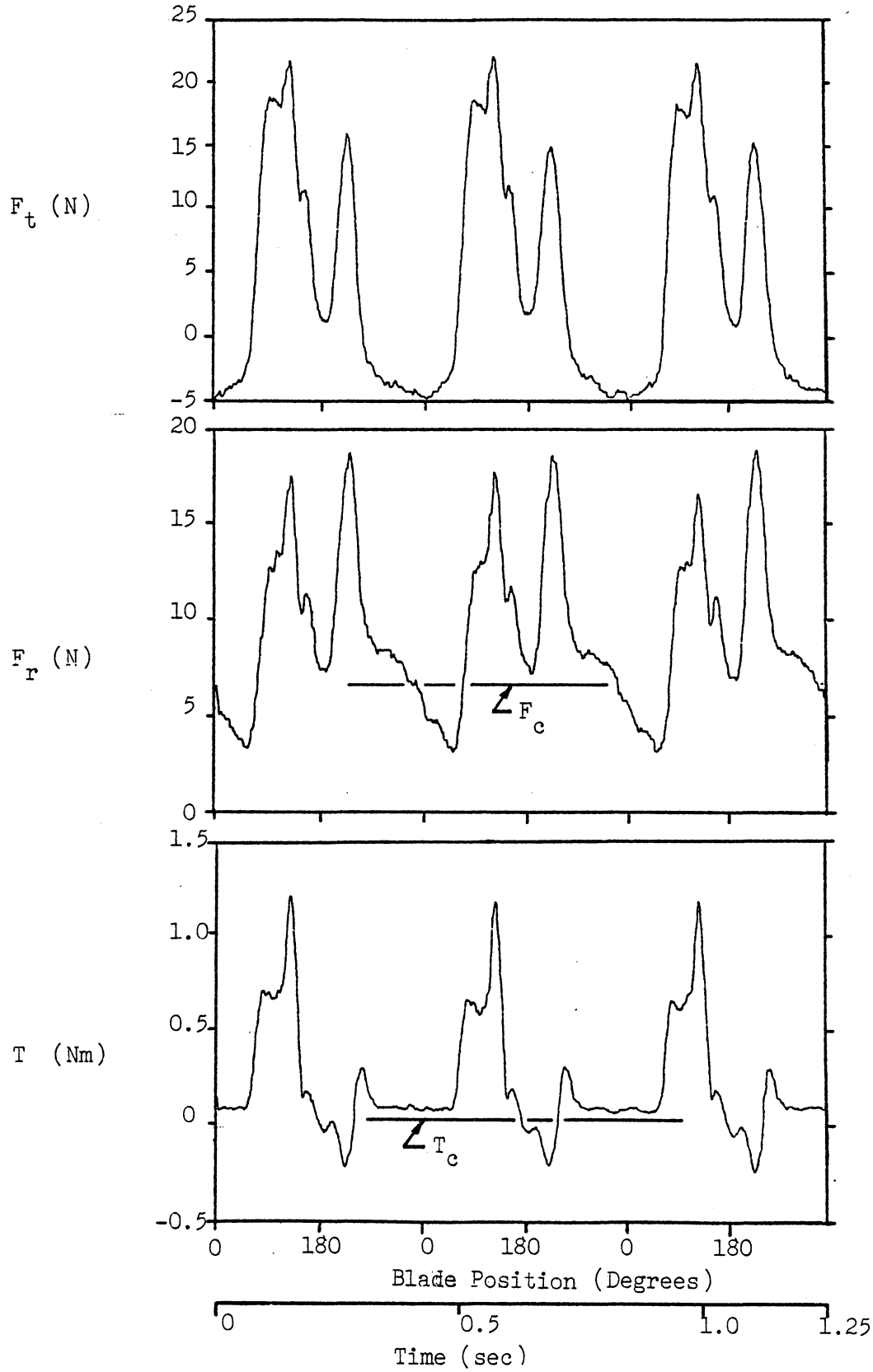


Figure 32: Blade Forces at H=1.01 m, $N_1$= 0.47

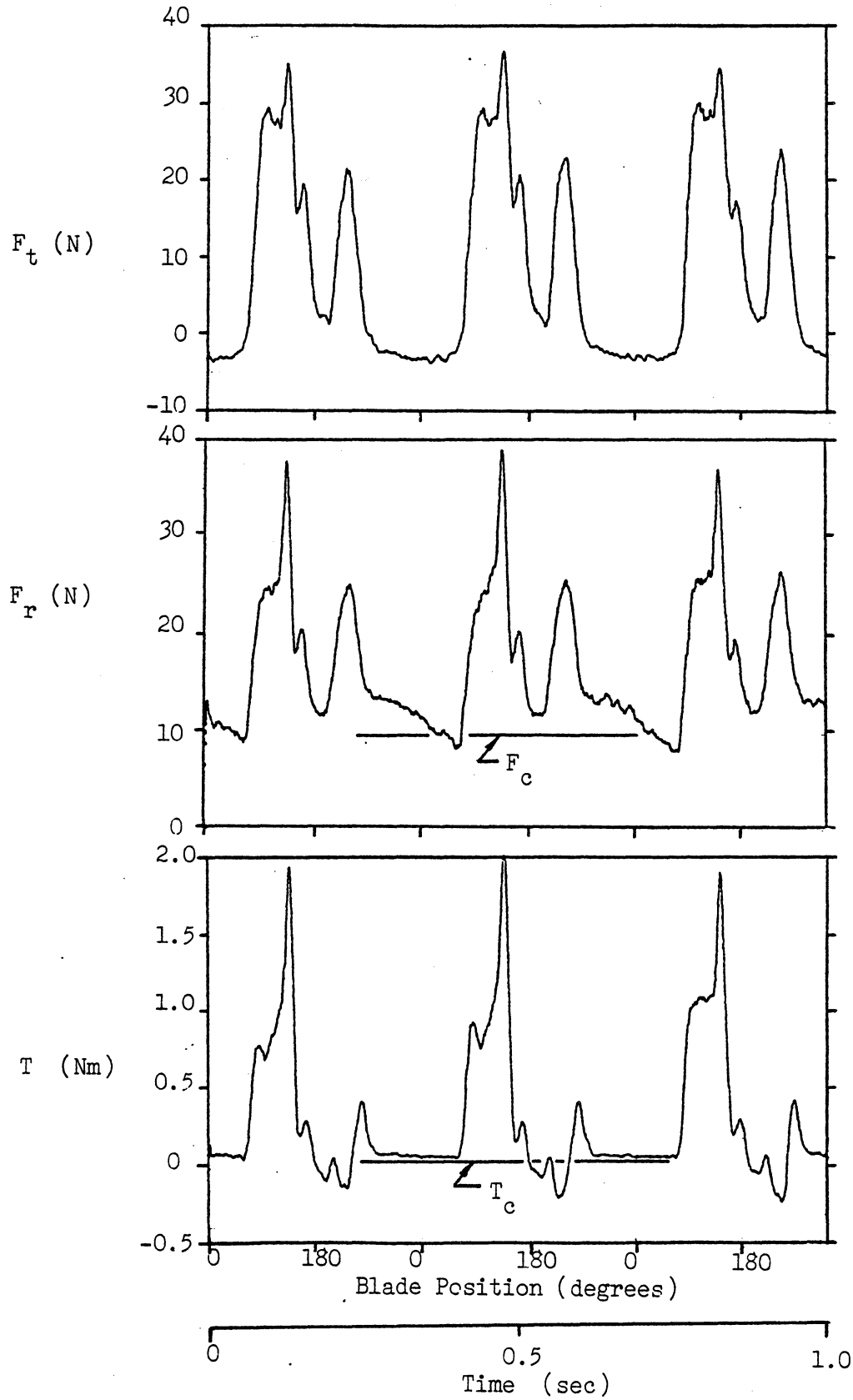


Figure 33: Blade Forces at H= 1.45 m, $N_1$= 0.47

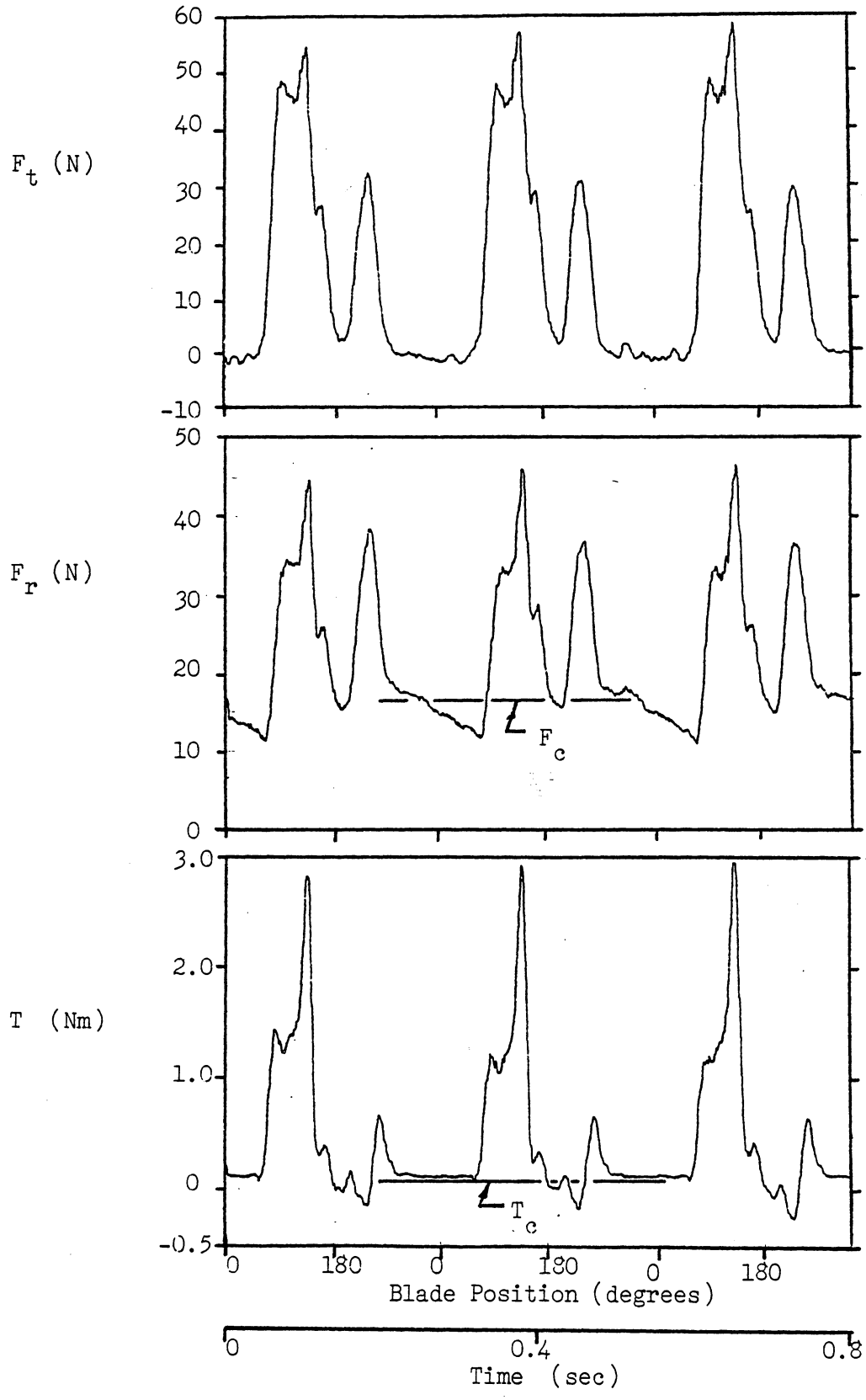


Figure 34: Blade Forces at H= 2.25 m, $N_1$ = 0.48

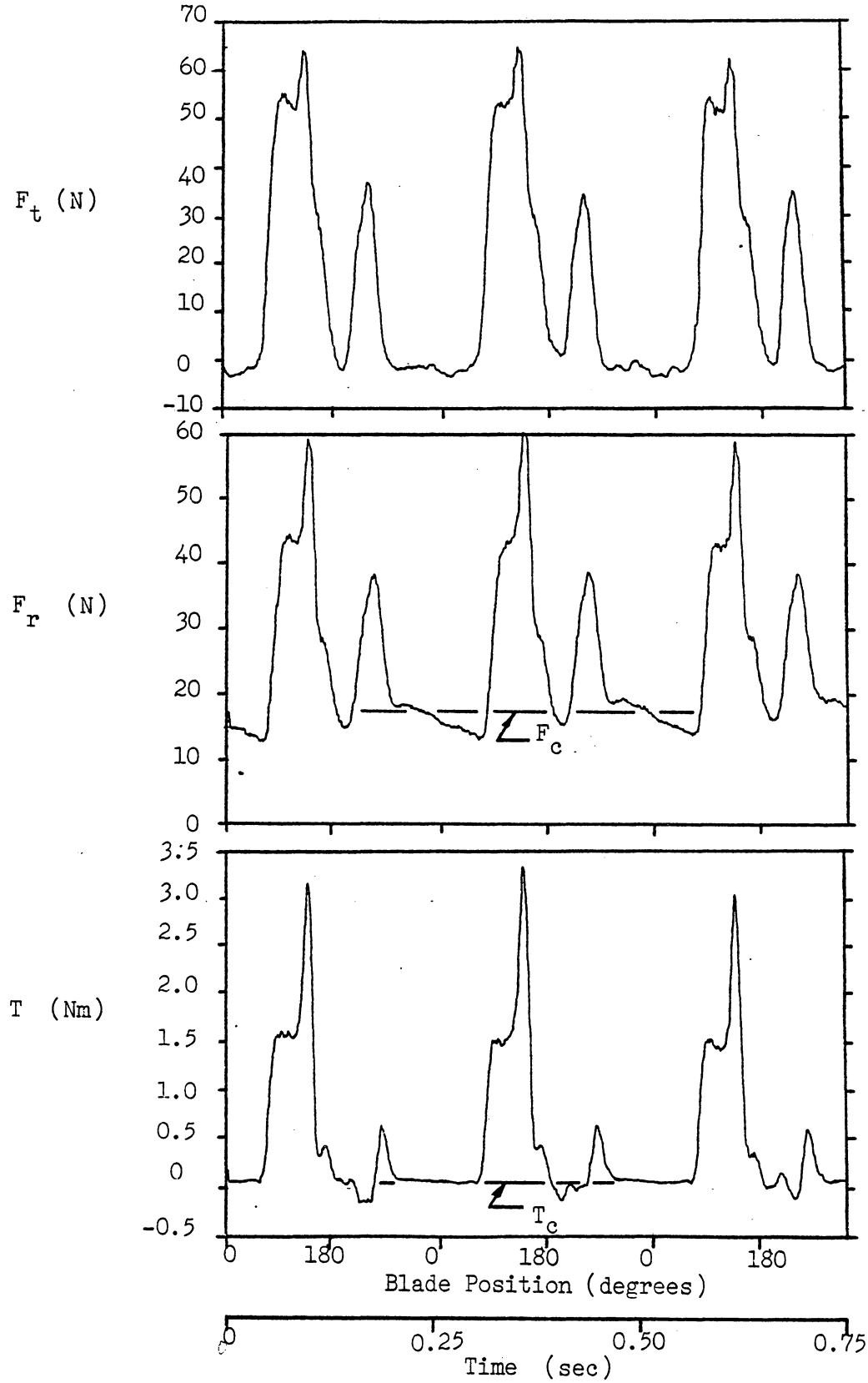


Figure 35: Blade Forces at H= 2.60 m, $N_1$= 0.47

higher heads. A possible explanation is that the static pressure in the nozzle exit increases with increasing head, and this causes an increase in the pressure differential, causing a larger spike.

In summary, there are minor variations in the patterns of the blade forces and torque as the head changes, but overall they are very similar at different heads.

#### 5.3.2.3 Forces at Varying Speeds

In the previous plots, the blade forces at different heads but at the optimum nondimensional speed, $N_1$, were compared. By keeping the head constant and varying $N_1$ we can see the effect of speed. Figures 34 and 36-40 show the blade forces at about 2.2 m head and $N_1$ from 0.35 to 1.10.

By looking at the tangential force in these figures, we can see that it is fairly consistent over the range of peak efficiencies ($N_1$=0.42-0.56). The pattern is very similar to that described at optimum speed--with the characteristic spike and two distinct passes through the runner. At the highest speed, essentially runaway speed ($N_1$=1.10), there appears to be only one pass. At that speed, we can see that the initial tangential force, as the runner enters the nozzle, is negative.

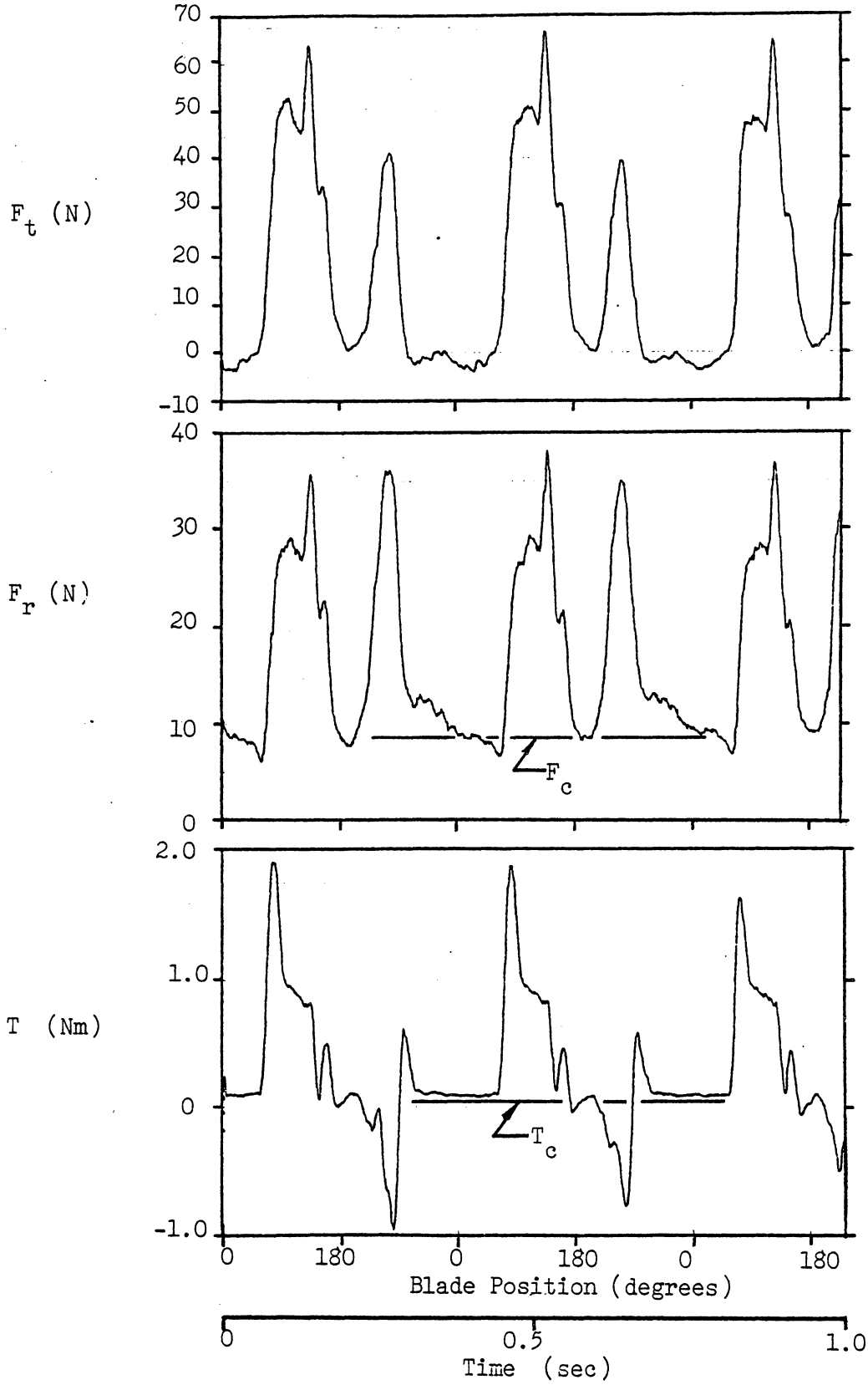


Figure 36: Blade Forces at H= 2.20 m, $N_1$= 0.35

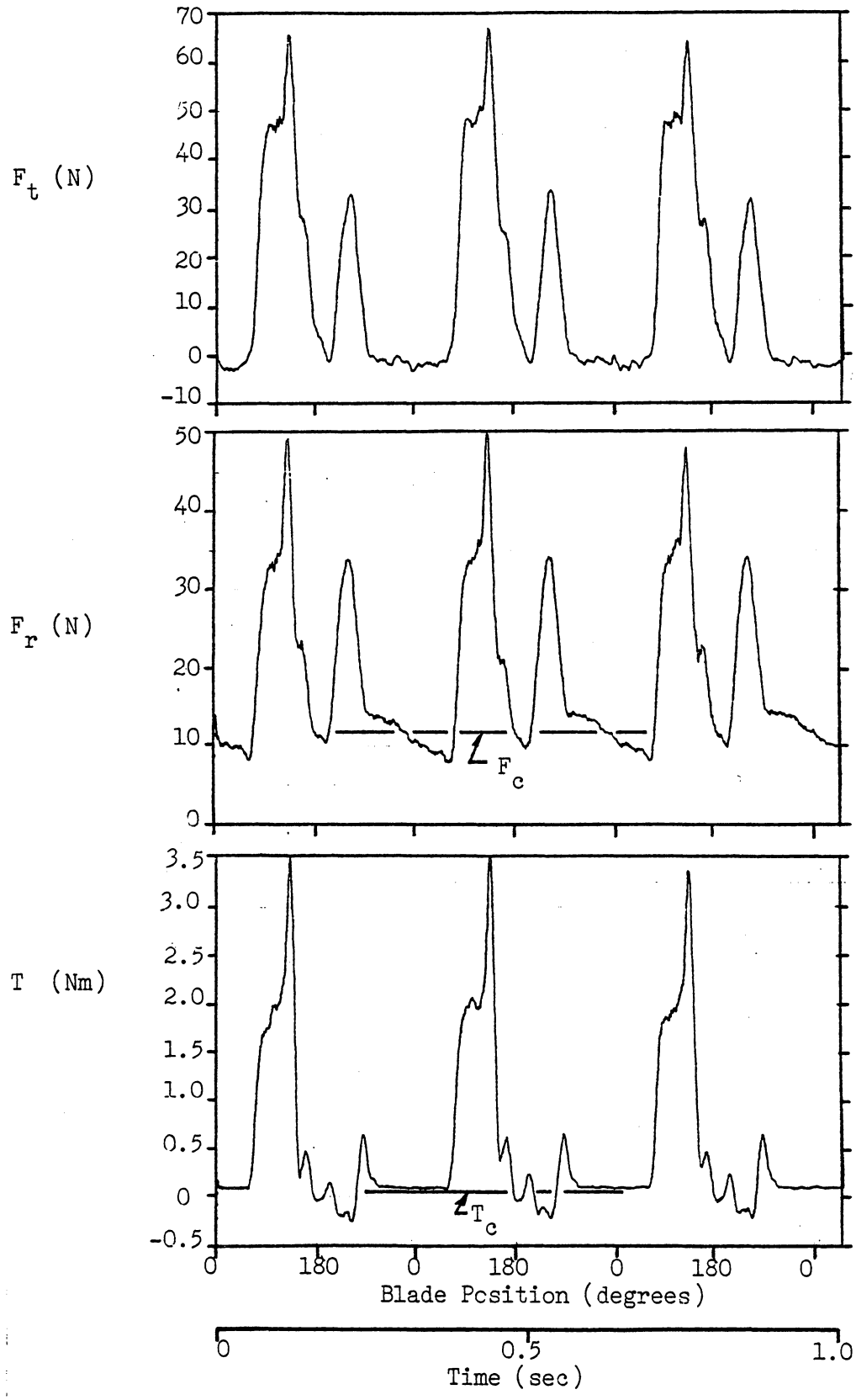


Figure 37: Blade Forces at H= 2.16 m, $N_1$= 0.42

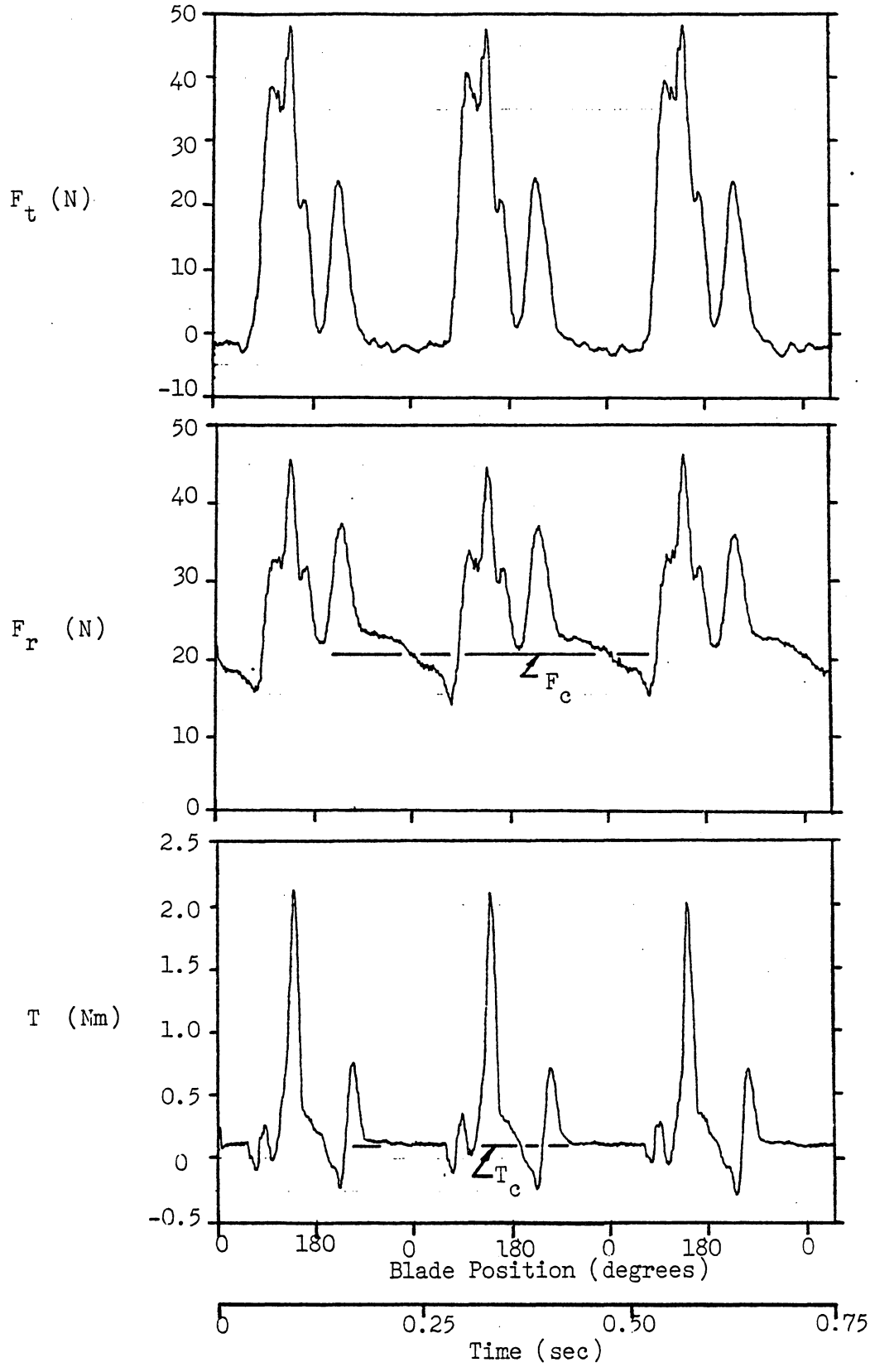


Figure 38: Blade Forces at H=2.13 m, $N_1$= 0.56

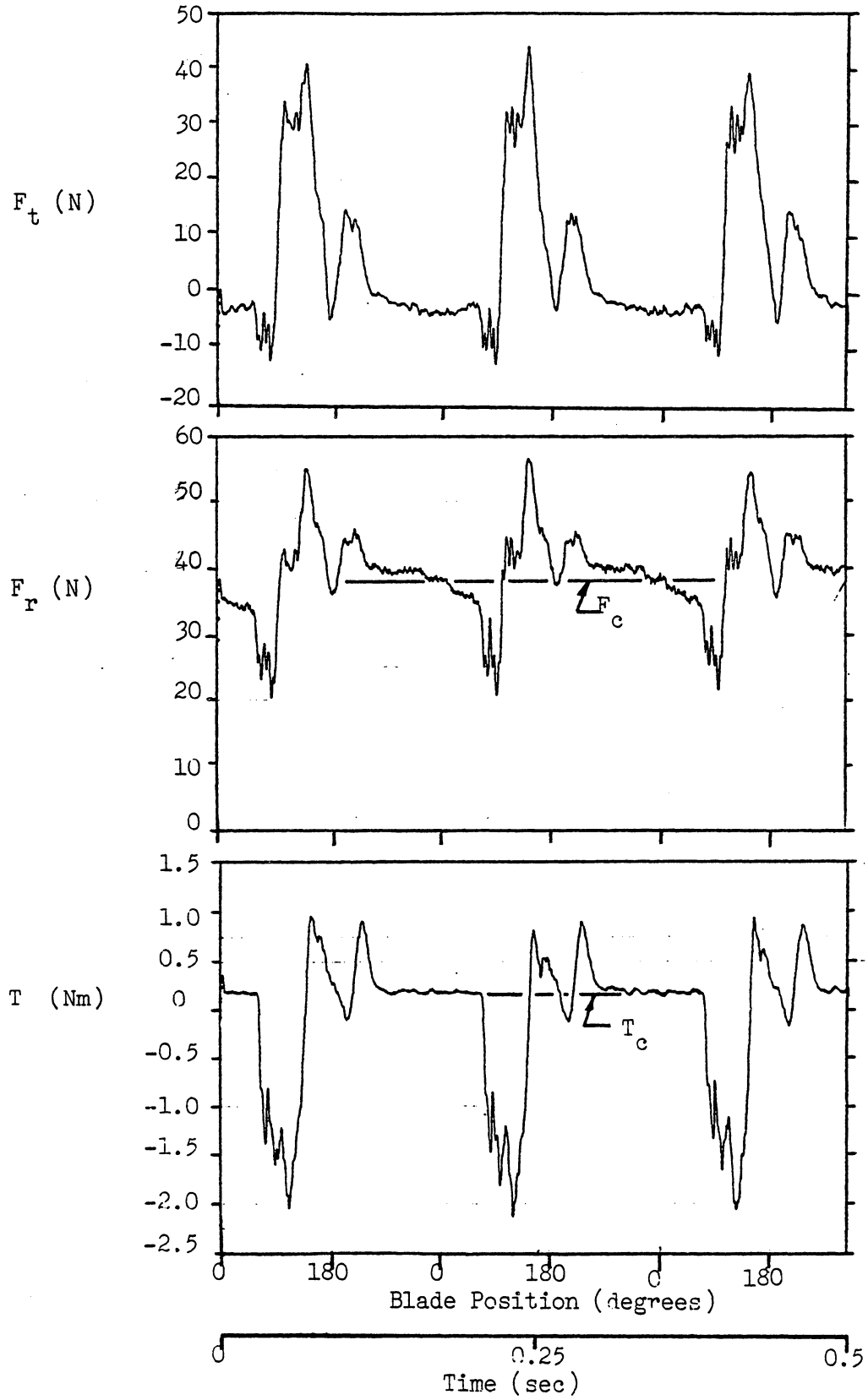


Figure 39: Blade Forces at H= 2.20 m, $N_1$= 0.75

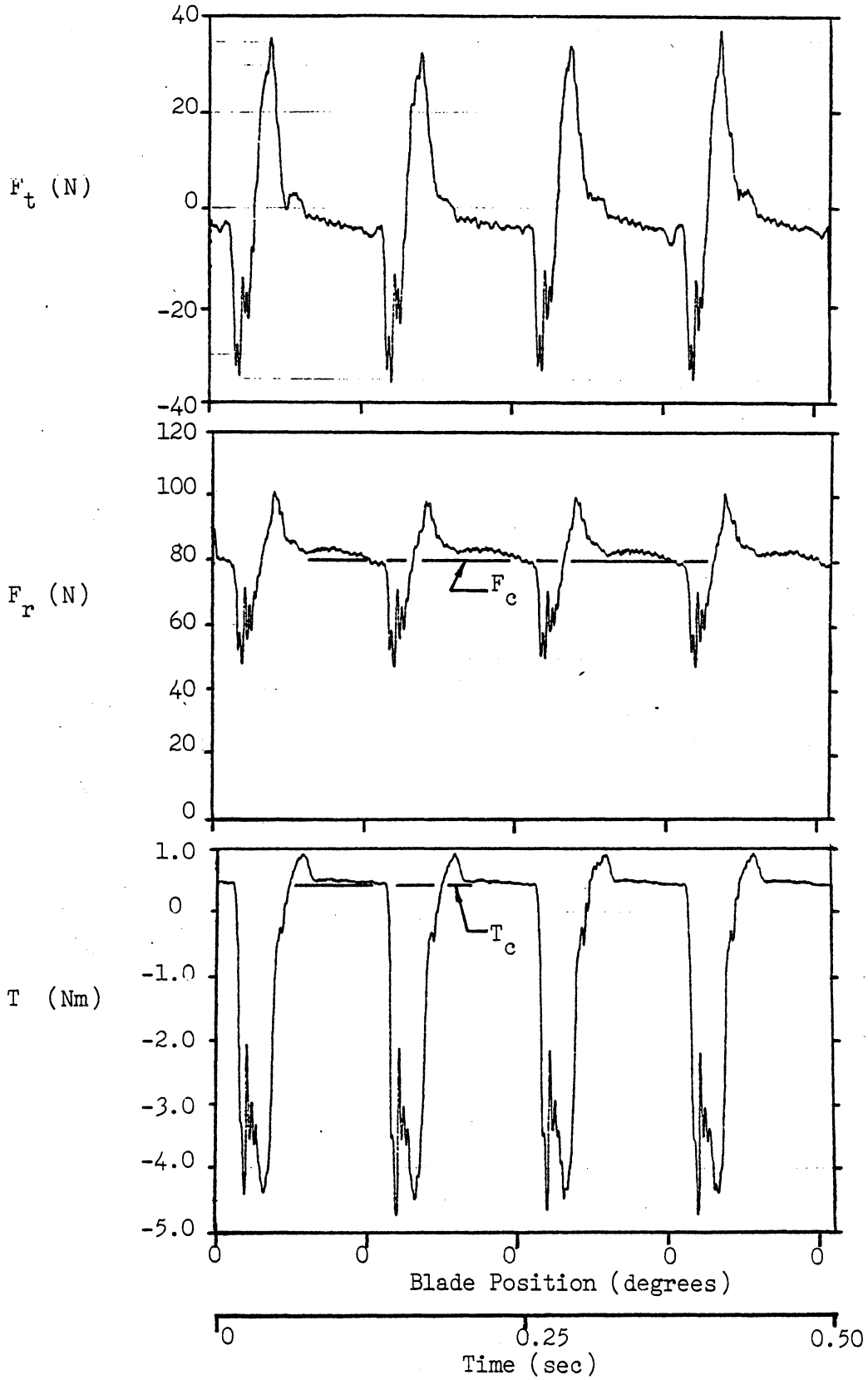


Figure 40: Blade Forces at H= 2.16 m, $N_1$= 1.10

It is interesting to note that at runaway speed the maximum tangential force (35 N) is lower than that at the optimum speed (60 N), but that the magnitude of the alternating force is approximately equal. For example, Fig. 40 at $N_1$=1.10 shows the force alternating between positive and negative 35 N, while Fig. 34 at $N_1$=0.48 shows a force variation of 30 N. We can conclude that at runaway speed, the alternating tangential force does not increase substantially.

From the radial forces in these figures, we can see that while the flow is in the optimum efficiency range, the pattern of blade loading is fairly consistent.

The centrifugal force is also shown on the figures. From this, we can see that the results are consistent with the mechanical forces. In the region where there is little water flow through the runner, the centrifugal forces agree well with the measured forces shown. We can also see the effect of the blade weight. For example, in Fig. 38, we can see that between BDC (270 degrees) and when the runner enters the nozzle (55 degrees), the force varies sinusoidally about the centrifugal force.

At runaway speed (Fig. 40) we can see that the largest radial force is due to the centrifugal force, but the fluid forces also impose a large alternating force. In this case,

the centrifugal force is 80 N while the fluid forces vary from positive 20 N to negative 30 N for an alternating component of 25 N.

The blade torques in these figures show very clearly the change in incidence angle with changing speed. At the slowest speed (Fig. 36) when the incidence angle is positive, there is a large positive torque on the blade as it initially enters the nozzle. As the speed increases, we can see that the initial blade torque goes from positive at $N_1$=0.42 and 0.48 (Figs. 37, 34) to slightly negative at $N_1$=0.56 (Fig. 38) to large negative values at $N_1$=0.75 and 1.10 (Figs. 39, 40). These large negative torques clearly show the high negative incidence angle when the blade passes the nozzle.

We can also see that the mechanical torque is small compared to the torque due to fluid forces. The centrifugal torque from Fig. 28 is shown on the figures and agrees well with the measured torque when the flow passage is empty.

### 5.3.3 Maximum Blade Forces

#### 5.3.3.1 Experimental and Theoretical Correlation

The primary objective of this study was to determine the maximum blade forces for design purposes. So far, we have studied the flow and the pattern of blade loading. The maxi-

mum forces were found to occur at a point slightly before the nozzle exit. These forces were read from the force plots. For the radial force, the centrifugal force was subtracted from the total force to find the fluid force. Then the forces were nondimensionalized as described in Chapter 4 and plotted as a function of the flow coefficient. The theoretical values were calculated including the full blade thickness and omitting the blade thickness. Since the blades were tapered at the leading and trailing edges, the actual value should lie between the two curves. The results for the tangential and radial forces are shown in Figs. 41 and 42.

We can see that the maximum tangential forces (Fig. 41) agree well with the theoretical values. Through the entire optimum speed range, the experimental values are bounded by the two theoretical curves. Only at very high speeds (large negative incidence angles) is there a significant difference between the values. We can also see that the data are consistent with varying heads.

The correlation is reasonable, but not as good for the maximum radial forces (Fig. 42). In the optimum speed range the correlation is good and the blade forces are slightly below the theoretical values. At high and low nondimensional speeds (large negative and positive incidence angles), the

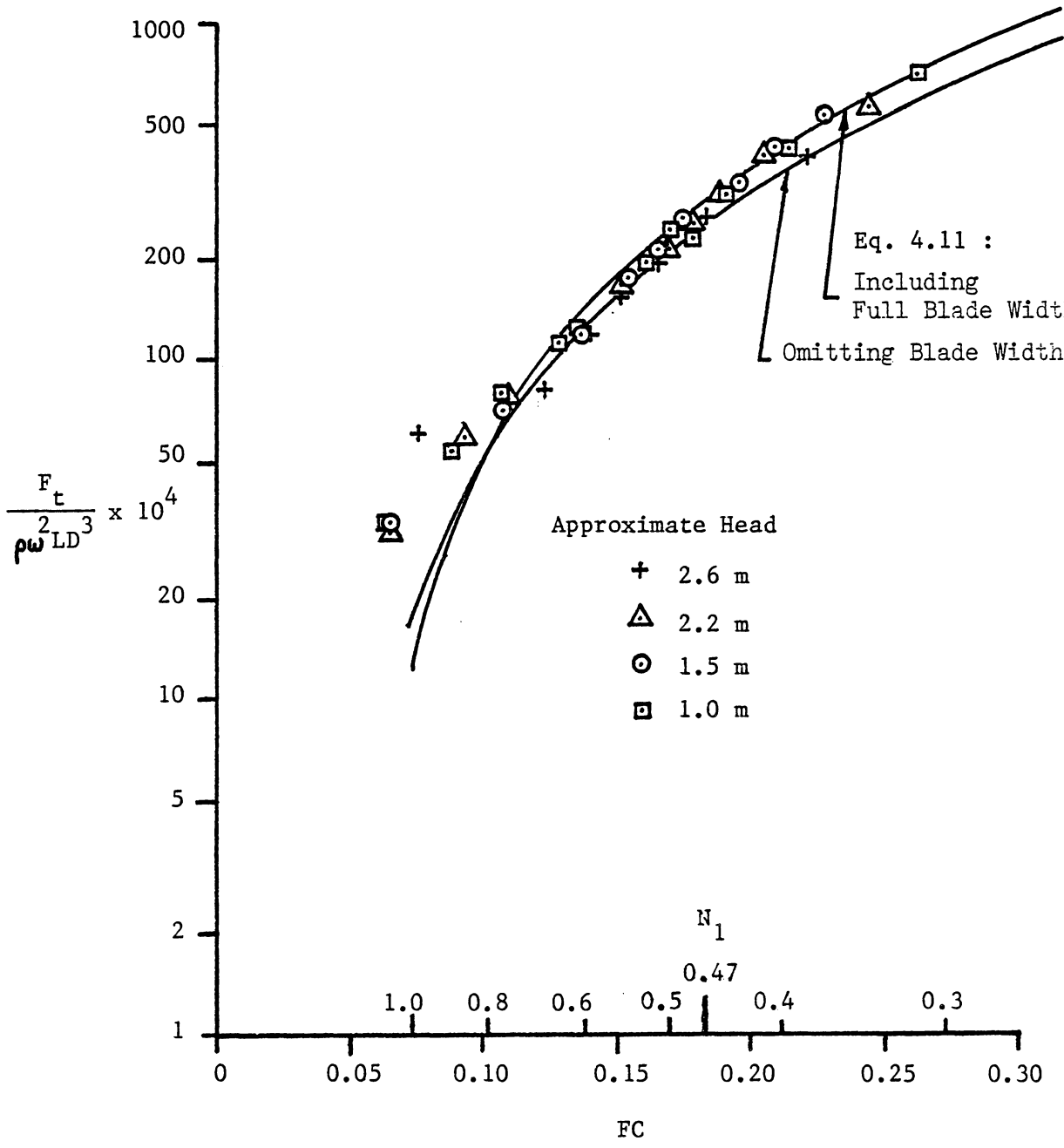


Figure 41: Maximum Tangential Forces

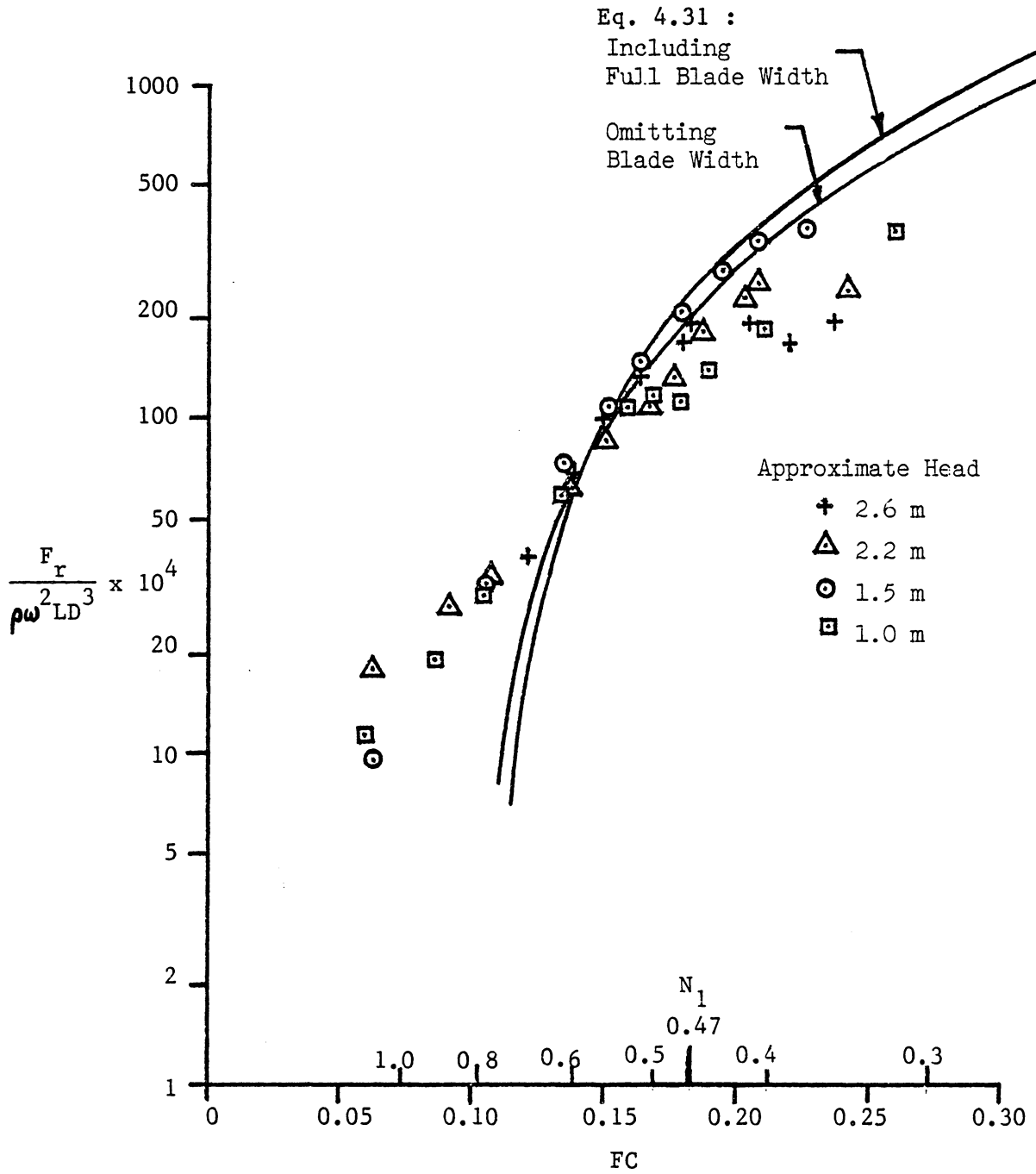


Figure 42: Maximum Radial Forces

correlation is not good. This is due to the full-passage assumption built into the analysis. From the flow visualization, we saw that the blade passages were not completely full at very high and low nondimensional speeds. Also evident is the larger scatter in the data for the radial forces. This is due to larger uncertainties associated with the radial forces than with the tangential forces.

The results of these two figures largely validate the usefulness of the force equations (Eq. 4.11 and 4.31). For design purposes, these expressions should give good guidelines as to the blade loading for stress calculations.

As a further aid in design, $N_1$ values obtained from Fig. 16 were also plotted on Figs. 41 and 42. This allows the designer to quickly go to the optimum speed ($N_1$=0.47) and determine the nondimensional forces at that point. For a geometrically similar machine, the actual blade forces can be determined by simply multiplying by the water density, angular velocity squared, length of the runner, and the diameter of the runner cubed. For other enclosed angles and total convergence angles, the forces can be calculated from Eqs. 4.11 and 4.31.

5.3.3.2 Alternative Calculations

The nondimensional force is in somewhat unconventional form in that it does not directly include a term for the head. This is because the force equations were derived as a function of mass flow rate through the blade passage and the relation between mass flow rate and head is difficult to calculate. As can be seen from Fig. 14, the flow is not constant, in fact, it does not vary linearly, over the entire range of nondimensional speed. For this reason, it was decided to show the force as a function of the flow coefficient and superimpose the nondimensional speed.

An alternate approach would be to consider only the practical range of the flow rates ($N_1$=0.4-0.6) and linearize the relation between flow and head by using Fig. 14. If this technique were used, the force could be directly plotted as a function of head, nondimensional speed, and geometric factors.

5.3.3.3 Example Turbine Selection and Force Calculation

Using the turbine characteristic curves (Figs. 13-15) and the blade force curves (Figs. 41 and 42), a geometrically similar turbine can be selected and the blade forces determined.

For example, a site has a head of 15 m and a design flow rate of 1.0 $^{m^3}/_{sec}$. The optimum runner tip speed will be:

$$U=0.47\sqrt{2gH} = 8.06\ ^{m}/_{sec}$$

If the design speed were 300 RPM, this would give a runner diameter of 0.513 m. At the optimum speed, the nondimensional flow rate can be seen to be 0.17 (Fig. 14) which implies the length of the runner must be 0.67 m to give the design flow rate.

Then from Figs. 41 and 42, the nondimensional tangential and radial forces at $N_1$=0.47 are read as 0.0264 and 0.0182. Thus, the maximum tangential force will be 2350 N and the maximum radial force will be 1620 N.

5.3.3.4 Limitations

There are several limitations to this method of force calculation, however. First, the actual pressure distribution on the blade is not known. For accurate stress calculations in the blades, this needs to be known. Secondly, the force equations were derived for full passage flow. The maximum force occurs near the nozzle exit where one passage is not completely full. In this case, there was good agreement between the calculations and experimental results, but under

other conditions it might not hold as well. For example, if the turbine was used with a draft tube, the pressure inside the casing would be less than atmospheric. This might cause a greater pressure difference between the nozzle and the casing, creating a greater spike near the nozzle exit. Both of these are good topics for additional research.

# Chapter VI

# CONCLUSIONS AND RECOMMENDATIONS

## 6.1 CONCLUSIONS

A cross-flow turbine was tested with the primary objective being to determine the fluid forces on the blades. It was tested over a head range from 1.0 m to 2.6 m, and over the nondimensional speed range, $N_1$=0.35-1.10 for each head. The blade forces, as well as the turbine's performance, were determined at these points. From the test results, the following conclusions can be drawn:

(a) Peak efficiency was found to occur at $N_1$=0.47. The efficiency at this point is between 65 and 70%; this could probably be improved with more careful attention to the nozzle-runner gap.

(b) The flow rate cannot be calculated without serious error if a free-jet is assumed. The flow was 17% lower than that calculated using a free-jet.

(c) From the flow visualization, the turning angle in the first pass and the validity of the full-passage assumption could be observed. Separation off the suction and pressure sides of the blades was seen at low and high speeds, respectively. The full-passage assumption appeared reasonable only near the optimum speed.

(d) The centrifugal force and torque were found by spinning the runner with no water flow. They were found to agree well with the measured forces during turbine operation, at points where there was no flow through the passages.

(e) Although the magnitudes are different, the pattern of blade loading at a given speed, $N_1$, remains nearly the same as head changes.

(f) The forces were recorded at runner speeds from $N_1$=0.35-1.10. At runaway speed, the fluid forces were not substantially higher than at optimum speed. The blade torque clearly shows the change in incidence angle over the speed range.

(g) The maximum blade forces occur when the blade is about 10 degrees before the nozzle exit, where there is a spike in force. The tangential forces were found to be in good agreement with the results of a full-passage control volume analysis, while the radial forces were slightly lower than predicted--possibly because of inward drag forces.

(h) Using Figs. 41 and 42, the turbine designer will be able to determine the blade forces for any geometrically similar machine.

## 6.2 RECOMMENDATIONS FOR FUTURE WORK

One of the shortcomings of the cross-flow turbine is its low maximum efficiency as compared to other hydraulic turbines. In an attempt to improve the efficiency, various runner and blade geometries should be tested. One variation would be to use a larger blade arc, giving a larger overall turning. Also, other blade shapes could be tested. The blade shape would not be as simple but it would still be two-dimensional, and the efficiency gained may offset the added cost.

For the blade forces, the pressure distribution would be useful in a more exact strength analysis. This could be measured statically by setting the absolute flow angle to the relative velocity angle from the turbine at optimum speed. However, the distribution so obtained might not exactly model the distribution in a runner.

Also, by using the force data obtained in this thesis, the stresses for various fastening techniques could be analyzed by using a finite element program.

In conclusion, the cross-flow turbine has the advantages of simple geometry and the possibility of good efficiencies over a wide range of flows. However, research still needs to be done to improve its efficiency and optimize its strength to make it less expensive. This could make it even more attractive for small hydropower applications.

# Appendix A

## CALIBRATION DATA

The strain gages on the runner were calibrated by hanging weights from the blade shaft when the runner was in two positions. First, the radial gages were calibrated by putting the runner in the 270 degree position (Fig. 25), when the force would be purely radial. Then, the tangential gage was calibrated by putting the runner in the 180 degree position, when the force would be purely tangential. The data points for the calibration are shown in Tables 2 and 3, and the curves are shown in Figs. 43 and 44. In Table 2 the output from link A is also given to determine the amount of link interaction. For the same reason, the outputs of links B and C are shown in Table. 3 The slope of each curve was determined using a least-squares fit. The standard deviation was computed for the uncertainty analysis.

The calibration weights were hung at a lever arm of 2.092 times the lever arm to the center of the blade. Thus, the tangential conversion factor is 2.092 divided by the slope. For the radial links, the force on each link was half of the total calibration weight, so the conversion factor was 2.092 divided by twice the slope. The slopes from the calibration curve and the resulting conversion factors are shown below:

| Link | Slope of the Calibration Curve (V/N) | Conversion Factor (N/V) |
|---|---|---|
| A | 0.00057791 | 3619.9 |
| B | 0.00026431 | 3957.5 |
| C | 0.00023991 | 4360.0 |

Forces could be obtained by measuring the bridge amplifier output in volts and multiplying by the conversion factor to get force in Newtons.

The calibration of the brake force was more straightforward. The calibration data points are shown in Table 4 and the curve is shown in Fig. 45. The force can be obtained from the bridge voltages by dividing them by the slope. The conversion factor is 515.93 N/V.

TABLE 2

Radial Force Calibration

| Applied Force (N) | Voltage Output From Link A ($V \times 10^4$) | Voltage Output From Link B ($V \times 10^4$) | Voltage Output From Link C ($V \times 10^4$) |
|---|---|---|---|
| 2.97 | -0.366 | 7.70 | 8.29 |
| 11.87 | 0.202 | 30.03 | 29.44 |
| 20.77 | 0.315 | 53.29 | 50.93 |
| 25.22 | 0.501 | 63.99 | 62.86 |
| 29.67 | 0.480 | 76.47 | 73.40 |
| 43.00 | 0.997 | 111.50 | 105.41 |
| 56.34 | 1.640 | 146.54 | 136.56 |
| 60.79 | 1.720 | 157.63 | 148.62 |
| 65.25 | 2.216 | 168.53 | 159.81 |
| 69.71 | 2.112 | 182.10 | 168.99 |
| 74.16 | 4.495 | 193.44 | 180.02 |
| 84.70 | 3.778 | 221.34 | 204.77 |
| 96.53 | 4.388 | 253.38 | 233.27 |
| 109.87 | 5.056 | 289.38 | 297.15 |
| | Slope ($V/N$) | 0.00026431 | 0.00023991 |
| | Standard Deviation (V) | 0.00009869 | 0.00007027 |

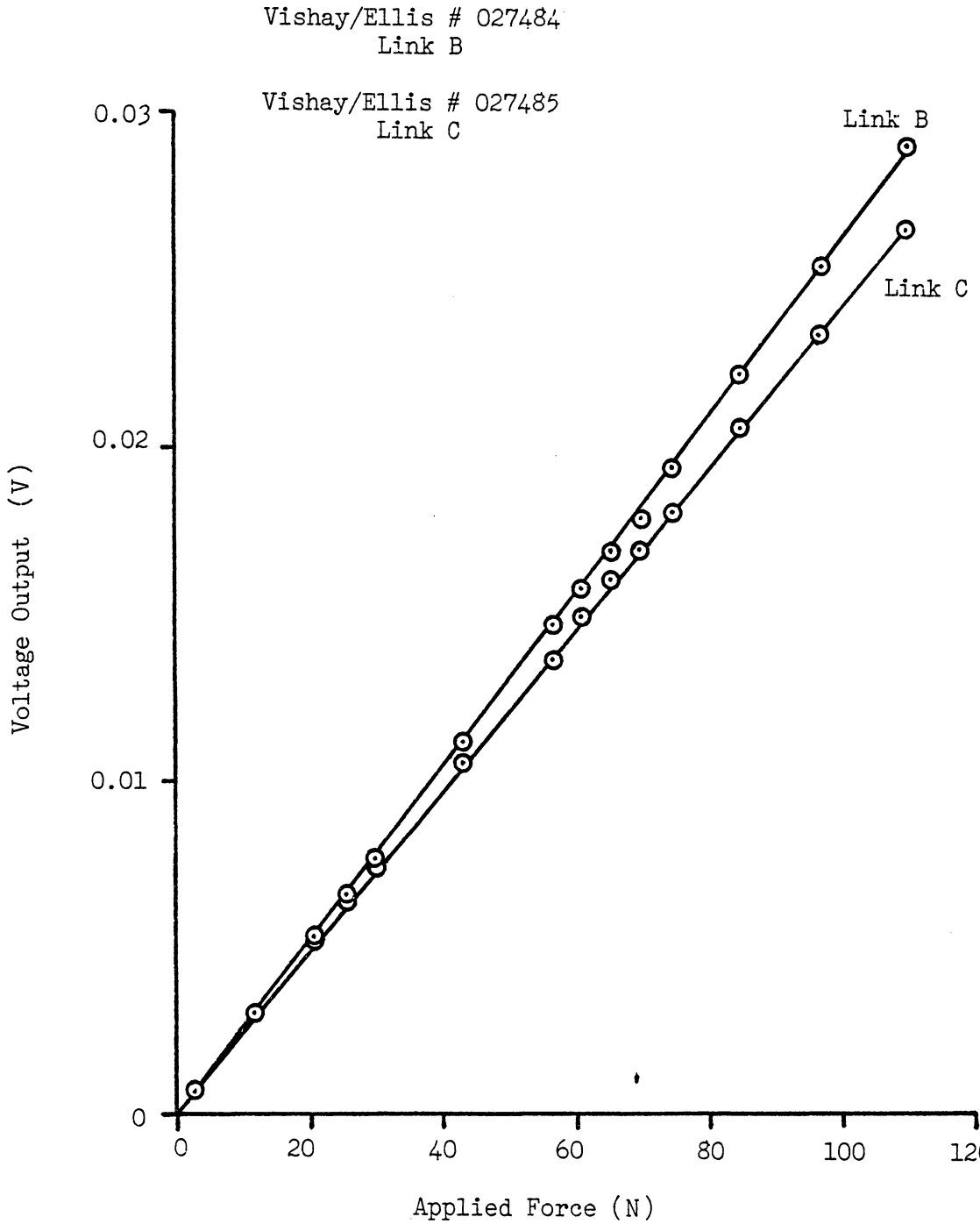


Figure 43: Radial Force Calibration

TABLE 3

Tangential Force Calibration

| Applied Force (N) | Voltage OUtput From Link A ($V \times 10^4$) | Voltage Output From Link B ($V \times 10^4$) | Voltage Output From Link C ($V \times 10^4$) |
|---|---|---|---|
| 2.97 | 16.80 | -0.008 | 0.020 |
| 7.48 | 41.21 | 0.154 | -0.650 |
| 11.87 | 67.60 | 0.516 | -0.812 |
| 20.77 | 118.94 | 1.592 | -2.257 |
| 29.67 | 170.07 | 0.783 | -1.298 |
| 34.12 | 195.36 | 0.375 | -2.029 |
| 38.59 | 223.75 | -2.900 | -1.365 |
| 43.04 | 248.31 | -1.315 | -2.270 |
| 47.48 | 273.78 | -3.531 | -2.246 |
| 58.02 | 335.86 | -3.988 | -0.255 |
| 69.85 | 401.88 | -2.633 | -2.054 |
| 83.19 | 479.81 | -2.197 | -2.781 |
| 96.53 | 557.47 | -3.791 | -2.636 |
| 109.87 | 633.55 | -3.756 | -5.295 |

Slope ($^V/_N$) 0.00057791

Standard Deviation 0.00007608

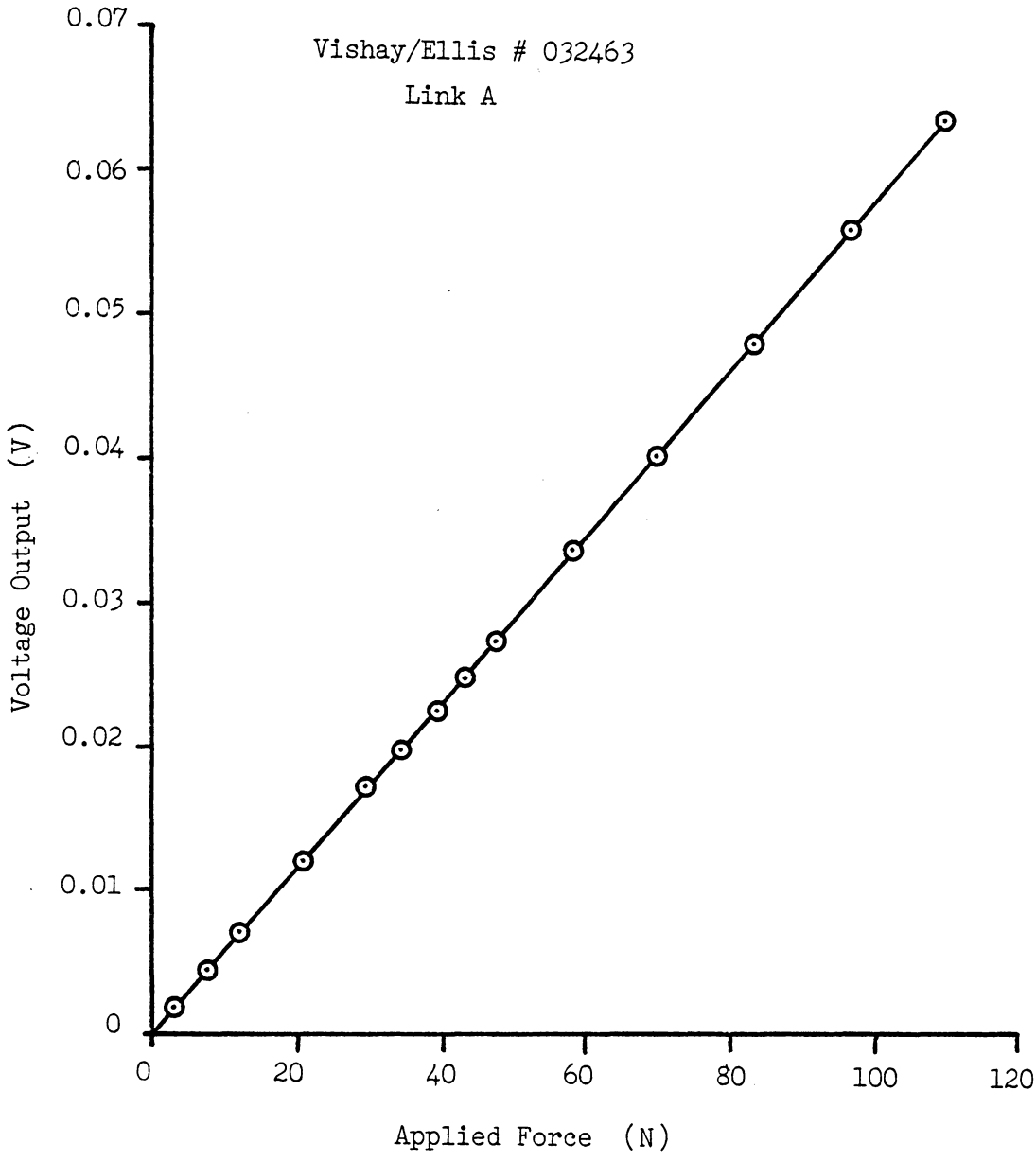


Figure 44: Tangential Force Calibration

TABLE 4

Brake Force Calibration

| Applied Force (N) | Voltage Output ($V \times 10^3$) |
|---|---|
| 2.80 | 5.48 |
| 14.63 | 28.47 |
| 19.08 | 36.94 |
| 23.55 | 45.50 |
| 34.09 | 66.06 |
| 38.55 | 74.80 |
| 42.99 | 83.43 |
| 47.44 | 92.22 |
| 56.33 | 109.32 |
| 65.23 | 126.56 |
| 78.57 | 152.61 |
| 83.02 | 161.27 |
| 96.36 | 186.44 |
| Slope ($^V/_N$) | 0.00193907 |
| Standard Deviation (V) | 0.00018397 |

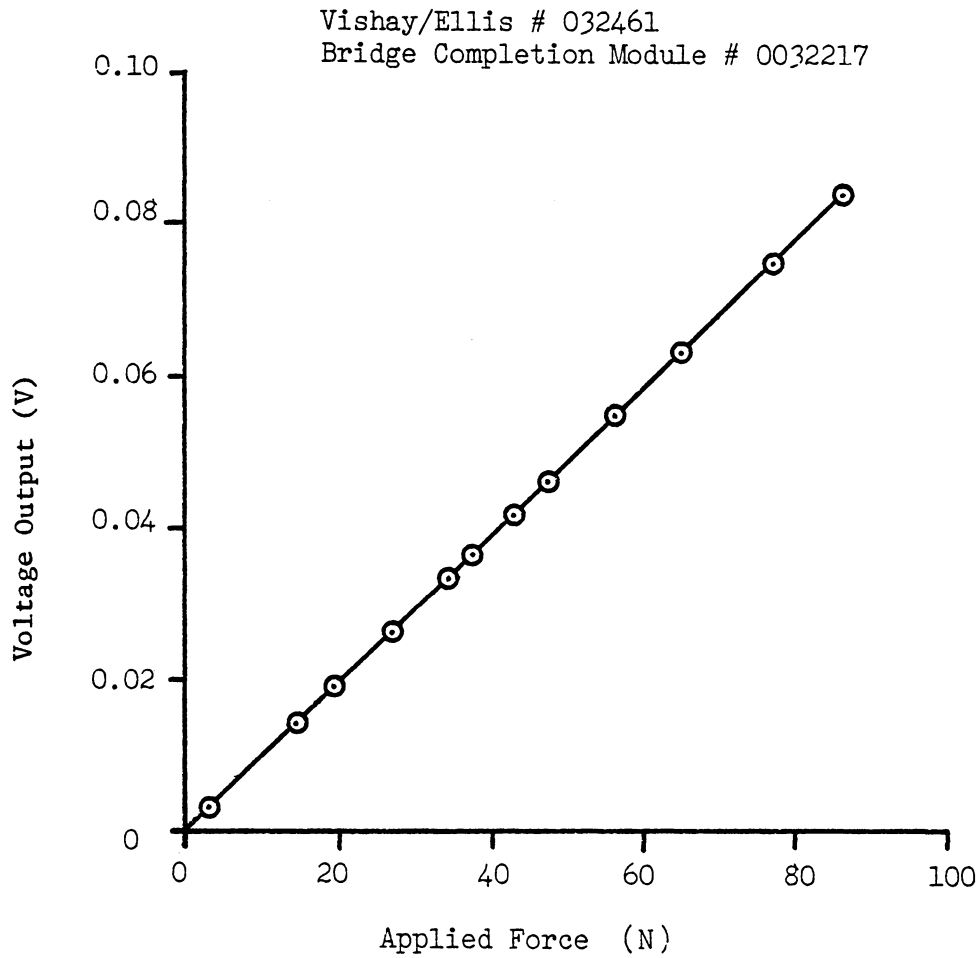


Figure 45: Brake Force Calibration

# Appendix B

# EXPERIMENTAL RESULTS

TABLE 5

Turbine Characteristics

| ID | HEAD (m) | RPM | Q ($m^3/s$) | P (W) | $N_1$ | EFF (%) | $P_1$ | $Q_1$ |
|---|---|---|---|---|---|---|---|---|
| 1 | 1.071 | 340.9 | 0.03281 | 24.8 | 1.078 | 7.2 | 0.0047 | 0.1313 |
| 2 | 1.082 | 281.7 | 0.03858 | 159.6 | 0.886 | 39.0 | 0.0300 | 0.1536 |
| 3 | 1.092 | 242.9 | 0.04060 | 224.2 | 0.761 | 51.6 | 0.0416 | 0.1609 |
| 4 | 1.047 | 192.9 | 0.04060 | 265.5 | 0.617 | 63.7 | 0.0524 | 0.1643 |
| 5 | 1.017 | 151.9 | 0.04060 | 283.1 | 0.493 | 70.0 | 0.0584 | 0.1668 |
| 6 | 1.012 | 161.5 | 0.04060 | 277.8 | 0.525 | 69.0 | 0.0577 | 0.1672 |
| 7 | 1.010 | 98.9 | 0.04060 | 232.7 | 0.322 | 57.9 | 0.0485 | 0.1673 |
| 8 | 1.012 | 133.3 | 0.04004 | 247.1 | 0.434 | 62.2 | 0.0513 | 0.1649 |
| 9 | 1.008 | 120.8 | 0.04032 | 261.1 | 0.394 | 65.5 | 0.0546 | 0.1663 |
| 10 | 1.005 | 143.8 | 0.04032 | 272.3 | 0.469 | 68.6 | 0.0572 | 0.1666 |
| 11 | 1.010 | 129.5 | 0.04032 | 271.0 | 0.422 | 67.9 | 0.0565 | 0.1662 |
| 12 | 1.507 | 371.0 | 0.04253 | 135.7 | 0.989 | 21.6 | 0.0155 | 0.1435 |
| 13 | 1.552 | 270.3 | 0.04880 | 395.4 | 0.710 | 53.3 | 0.0433 | 0.1622 |
| 14 | 1.493 | 136.8 | 0.04973 | 450.0 | 0.366 | 61.8 | 0.0522 | 0.1686 |
| 15 | 1.466 | 163.9 | 0.04950 | 484.9 | 0.443 | 68.2 | 0.0578 | 0.1693 |
| 16 | 1.504 | 206.9 | 0.04996 | 488.6 | 0.552 | 66.3 | 0.0560 | 0.1687 |
| 17 | 1.526 | 229.6 | 0.04903 | 458.4 | 0.608 | 62.5 | 0.0514 | 0.1644 |
| 18 | 1.487 | 187.8 | 0.04880 | 481.7 | 0.504 | 67.7 | 0.0562 | 0.1658 |
| 19 | 1.453 | 172.2 | 0.04903 | 483.9 | 0.468 | 69.3 | 0.0585 | 0.1685 |
| 20 | 1.478 | 150.6 | 0.04973 | 481.6 | 0.405 | 66.9 | 0.0567 | 0.1694 |
| 21 | 1.462 | 139.7 | 0.04996 | 458.6 | 0.378 | 64.1 | 0.0549 | 0.1711 |
| 22 | 1.498 | 286.4 | 0.04809 | 331.0 | 0.766 | 46.9 | 0.0382 | 0.1627 |
| 23 | 1.463 | 161.5 | 0.04973 | 482.3 | 0.437 | 67.6 | 0.0577 | 0.1703 |
| 24 | 1.446 | 400.0 | 0.03946 | 29.9 | 1.089 | 5.3 | 0.0036 | 0.1359 |
| 25 | 2.204 | 339.4 | 0.05782 | 577.2 | 0.748 | 46.2 | 0.0373 | 0.1613 |
| 26 | 2.220 | 277.4 | 0.05996 | 756.6 | 0.609 | 58.0 | 0.0484 | 0.1667 |
| 27 | 2.134 | 250.0 | 0.05958 | 780.7 | 0.560 | 62.6 | 0.0530 | 0.1689 |
| 28 | 2.264 | 232.3 | 0.06147 | 884.7 | 0.505 | 64.9 | 0.0549 | 0.1692 |
| 29 | 2.246 | 219.2 | 0.06128 | 884.6 | 0.479 | 65.6 | 0.0556 | 0.1694 |
| 30 | 2.157 | 188.1 | 0.06053 | 818.3 | 0.419 | 63.9 | 0.0546 | 0.1707 |
| 31 | 2.137 | 202.9 | 0.05996 | 819.4 | 0.454 | 65.2 | 0.0555 | 0.1699 |
| 32 | 2.214 | 186.1 | 0.06147 | 850.0 | 0.409 | 63.7 | 0.0546 | 0.1711 |
| 33 | 2.198 | 160.2 | 0.06147 | 777.3 | 0.354 | 58.7 | 0.0505 | 0.1717 |
| 34 | 2.270 | 400.8 | 0.05782 | 451.2 | 0.871 | 35.1 | 0.0279 | 0.1590 |
| 35 | 2.162 | 493.8 | 0.04903 | 53.1 | 1.099 | 5.1 | 0.0035 | 0.1381 |

Turbine Characteristics (cont.)

| ID | HEAD (m) | RPM | Q ($m^3/s$) | P (W) | $N_1$ | EFF (%) | $P_1$ | $Q_1$ |
|---|---|---|---|---|---|---|---|---|
| 36 | 2.682 | 392.2 | 0.06402 | 732.7 | 0.784 | 43.5 | 0.0353 | 0.1619 |
| 37 | 2.894 | 471.9 | 0.06366 | 547.9 | 0.908 | 30.3 | 0.0235 | 0.1550 |
| 38 | 2.691 | 488.9 | 0.05880 | 352.4 | 0.975 | 22.7 | 0.0169 | 0.1485 |
| 39 | 2.819 | 565.5 | 0.05660 | 80.6 | 1.102 | 5.2 | 0.0036 | 0.1396 |
| 40 | 2.768 | 348.0 | 0.06448 | 949.6 | 0.685 | 54.3 | 0.0436 | 0.1605 |
| 41 | 2.663 | 300.8 | 0.06579 | 1009.6 | 0.603 | 58.8 | 0.0492 | 0.1670 |
| 42 | 2.628 | 253.2 | 0.06561 | 1083.9 | 0.511 | 64.1 | 0.0538 | 0.1676 |
| 43 | 2.702 | 281.7 | 0.06648 | 1093.3 | 0.561 | 62.1 | 0.0521 | 0.1675 |
| 44 | 2.729 | 234.7 | 0.06784 | 1174.4 | 0.465 | 64.7 | 0.0551 | 0.1701 |
| 45 | 2.713 | 194.8 | 0.06784 | 1095.8 | 0.387 | 60.7 | 0.0519 | 0.1706 |
| 46 | 2.657 | 207.6 | 0.06716 | 1109.7 | 0.417 | 63.5 | 0.0542 | 0.1707 |
| 47 | 2.623 | 179.6 | 0.06699 | 1017.9 | 0.363 | 59.1 | 0.0507 | 0.1713 |
| 48 | 2.600 | 232.8 | 0.06631 | 1085.5 | 0.473 | 64.2 | 0.0548 | 0.1703 |

TABLE 6

Blade Forces

| ID | $N_1$ | FC | $F_t$ (N) | $F_{r\ tot}$ (N) | $F_{cent}$ (N) | $F_r$ (N) | $F_{1t}$ x $10^4$ | $F_{1r}$ x $10^4$ |
|---|---|---|---|---|---|---|---|---|
| 1 | 1.078 | 0.0609 | 18.0 | 44.0 | 38.0 | 6.0 | 33.88 | 11.29 |
| 2 | 0.886 | 0.0867 | 20.0 | 33.0 | 26.0 | 7.0 | 55.13 | 19.29 |
| 3 | 0.761 | 0.1058 | 22.0 | 27.5 | 19.5 | 8.0 | 81.56 | 29.66 |
| 4 | 0.617 | 0.1332 | 22.0 | 22.5 | 12.4 | 10.1 | 129.32 | 59.37 |
| 5 | 0.493 | 0.1692 | 26.0 | 20.0 | 7.5 | 12.5 | 246.46 | 118.49 |
| 6 | 0.525 | 0.1591 | 23.5 | 21.0 | 8.4 | 12.6 | 197.07 | 105.66 |
| 7 | 0.322 | 0.2598 | 32.0 | 19.0 | 3.0 | 16.0 | 715.57 | 357.79 |
| 8 | 0.434 | 0.1901 | 26.0 | 17.0 | 5.6 | 11.4 | 320.04 | 140.33 |
| 9 | 0.394 | 0.2112 | 27.0 | 18.0 | 4.6 | 13.4 | 404.69 | 200.85 |
| 10 | 0.469 | 0.1775 | 22.0 | 17.3 | 6.6 | 10.7 | 232.70 | 113.18 |
| 16 | 0.552 | 0.1528 | 34.5 | 35.5 | 14.5 | 21.0 | 176.28 | 107.30 |
| 17 | 0.608 | 0.1351 | 30.0 | 35.0 | 17.3 | 17.7 | 124.47 | 73.44 |
| 18 | 0.504 | 0.1645 | 34.5 | 35.5 | 11.5 | 24.0 | 213.96 | 148.84 |
| 19 | 0.468 | 0.1802 | 35.5 | 38.0 | 9.8 | 28.2 | 261.85 | 208.01 |
| 20 | 0.405 | 0.2090 | 44.5 | 42.5 | 7.3 | 35.2 | 429.15 | 339.46 |
| 21 | 0.378 | 0.2263 | 48.0 | 38.5 | 6.2 | 32.3 | 537.95 | 362.00 |
| 22 | 0.766 | 0.1063 | 27.0 | 39.0 | 27.0 | 12.0 | 72.00 | 32.00 |
| 23 | 0.437 | 0.1949 | 40.5 | 41.0 | 8.0 | 33.0 | 339.63 | 276.74 |
| 24 | 1.089 | 0.0624 | 24.5 | 61.5 | 54.5 | 7.0 | 33.49 | 9.57 |
| 25 | 0.748 | 0.1078 | 41.0 | 55.5 | 37.8 | 17.7 | 77.85 | 33.61 |
| 26 | 0.609 | 0.1368 | 44.0 | 47.0 | 25.0 | 22.0 | 125.07 | 62.53 |
| 27 | 0.560 | 0.1508 | 48.0 | 45.5 | 20.7 | 24.8 | 167.98 | 86.79 |
| 28 | 0.505 | 0.1675 | 53.0 | 45.5 | 17.8 | 27.7 | 214.82 | 112.27 |
| 29 | 0.479 | 0.1769 | 56.5 | 46.0 | 16.8 | 29.2 | 257.20 | 132.92 |
| 30 | 0.419 | 0.2037 | 65.5 | 49.0 | 12.0 | 37.0 | 404.91 | 228.73 |
| 31 | 0.454 | 0.1870 | 60.5 | 48.0 | 13.6 | 34.4 | 321.43 | 182.76 |
| 32 | 0.409 | 0.2090 | 68.0 | 52.0 | 11.4 | 40.6 | 429.45 | 256.41 |
| 33 | 0.354 | 0.2428 | 65.0 | 37.0 | 8.3 | 28.7 | 553.97 | 244.60 |
| 34 | 0.871 | 0.0913 | 43.5 | 75.0 | 54.6 | 20.4 | 59.23 | 27.78 |
| 35 | 1.099 | 0.0628 | 35.0 | 100.0 | 80.0 | 20.0 | 31.40 | 17.94 |
| 40 | 0.685 | 0.1173 | 46.0 | 62.0 | 40.0 | 22.0 | 83.08 | 39.73 |
| 41 | 0.603 | 0.1384 | 50.0 | 60.0 | 30.0 | 30.0 | 120.87 | 72.52 |
| 42 | 0.511 | 0.1640 | 57.5 | 60.5 | 21.2 | 39.3 | 196.17 | 134.08 |
| 43 | 0.561 | 0.1494 | 56.0 | 62.5 | 26.2 | 36.3 | 154.35 | 100.05 |
| 44 | 0.465 | 0.1829 | 68.0 | 66.5 | 18.0 | 48.5 | 270.01 | 192.58 |
| 45 | 0.387 | 0.2204 | 70.0 | 42.0 | 12.5 | 29.5 | 403.47 | 170.04 |
| 46 | 0.417 | 0.2047 | 83.5 | 52.0 | 14.2 | 37.8 | 423.77 | 191.84 |
| 47 | 0.363 | 0.2361 | 75.0 | 40.5 | 11.5 | 29.0 | 508.56 | 196.64 |
| 48 | 0.473 | 0.1803 | 64.0 | 60.0 | 18.0 | 42.0 | 258.29 | 169.50 |

## LIST OF REFERENCES


1. Papamarcos, John,"Developments in Hydropower," Power Engineering, December, 1978, pp. 30-34.

2. Hanchey, James, R., "Hydropower--An Assessment of the Prospects for Development," Energy Technology VIII, Proceedings of the Eighth Energy Technology Conference, Washington, D.C., March 9-11, 1981, pp. 1354-1364.

3. Gladwell, John, S., Warnick, Calvin, C.,"Low-Head Hydro: An Examination of an Alternative Energy Source," Idaho Water Resources Institute, Moscow, Idaho, 1978, p. 17. From the Seminar "Low-Head Hydroelectric Technology--Problems and Opportunities of an Alternative Energy Source," University of Idaho, June 6-7, 1978.

4. Noyes, Robert, Ed., Small and Micro Hydroelectric Power Plants--Technology and Feasibility, Energy Technology Review, No. 60, pp. 0-24, 1980. Information summarized from "Preliminary Inventory of Hydropower Resources," prepared by the U.S. Army Corps of Engineer's Institute for Water Resources and Hydrologic Center as part of the National Hydroelectric Power Resources Study, July, 1979.

5. Kennedy, Joe, "Generating Profits," Roanoke Times and World News, November 29, 1983.

6. Noyes, Robert, Ed., Small and Micro Hydroelectric Power Plants--Technology and Feasibility, Energy Technology Review, No. 60, pp. 25-35, 1980. Information summarized from "Feasibility Studies for Small Scale Hydroelectric Additions--A Guide Manual", prepared by the U.S. Army Corps of Engineer's Institute for Water Resources and Hydrologic Center with funding from the U.S. Department of Energy, July, 1979.

7. Wayne, Warner, W., "Small-Scale Hydro Equipment," Energy Technology VIII, Proceedings of the Eighth Energy Technology Conference, Washington, D.C., March 9-11, 1981, pp. 1365-1376.

8. Wayne, Warner, W.,"Available Low-Head Hydro Technology," Energy Technology VI, Proceedings of the Sixth Energy Technology Conference, Washington, D.C., February 26-28, 1979, pp. 932-949.

9. "Simplified Methodology for Economic Screening of Potential Low-Head, Small Capacity Hydroelectric Sites," Electrical Power Research Institute, No. 1679, January, 1981.

10. Haimerl, L., A.,"The cross-flow Turbine," Water Power, January, 1960, pp. 5-13.

11. Mockmore, C., A., Merryfield, F.,"The Banki Water Turbine," Engineering Experimental Station, Bulletin No. 25, Oregon State University, February, 1949.

12. Johnson, W., Ely, R., White, F.,"Design and Testing of an Inexpensive Crossflow Turbine," from Small Hydro-Power Fluid Machinery, presented at the Annual Winter Meeting, ASME, Phoenix, Arizona, November 14-19, 1982, ASME, NY, pp. 129-133.

13. Nakase, Y., et al.,"A Study of cross-flow Turbine (Effects of Nozzle Shape on its Performance)," from Small Hydro-Power Fluid Machinery, presented at the Annual Winter Meeting, ASME, Phoenix, Arizona, November 14-19, 1982, ASME, NY, pp. 13-18.

14. Balje, O., E., Turbomachines-A Guide to Design, Selection and Theory, pp. 328-336, John Wiley and Sons, 1981.

15. Stapenhorst, F., W., E.,"The Ossberger cross-flow Turbine," from Small Hydro-Power Fluid Machinery, presented at the Annual Winter Meeting, ASME, Chicago, Illinois, November 16-21, 1980, ASME, NY, pp. 27-29.

16. Hamm, Hans, W.,"Low-Cost Development of Small Water Power Sites," Volunteers in Technical Assistance, Mount Rainier, Maryland, 1967, pp. 25-30.

17. Breslin, W., R.,"Small Michell (Banki) Turbine: A Construction Manual," Volunteers in Technical Assistance, Mount Rainier, Maryland, 1980, pp. 1-31.

18. Durali, Mohammed,"Design of Small Water Turbines for Farms and Small Communities," Technology Adaptation Program, TAP Report 76-1, Massachusetts Institute of Technology, 1976, pp. 19-57.

19. Company Literature from Balaju Yantra Shala (P) Ltd., P. O. Box 209, Balaju, Kathmandu, Nepal.

20. Beckwith, T., G., Buck, N., L., Marangoni, R., D., Mechanical Measurements, Third Edition, pp.353-405, Addison-Wesley, 1978.

21. Siegel, Robert, P.,"Head Augumentation in Hydraulic Reaction Turbines by Means of Draft Tube Ejectors," M. S. Thesis, Virginia Polytechnic Institute and State University, 1982.

22. Light, Roger W.,"Development of a Rotating-to-Stationary Data Transfer System Based on FM Telemetry," M. S. Thesis, Virginia Polytechnic Institute and State University, 1975.

23. Holman, J., P., Experimental Methods for Engineers, pp. 44-51, McGraw-Hill, Inc., NY, 1978.

24. White, Frank, M., Viscous Fluid Flow, p. 672, McGraw-Hill, Inc., NY, 1974.

**The vita has been removed from the scanned document**